TRAPPING AND MANIPULATING SINGLE MOLECULES IN SOLUTION

A DISSERTATION
SUBMITTED TO THE DEPARTMENT OF PHYSICS
AND THE COMMITTEE ON GRADUATE STUDIES
OF STANFORD UNIVERSITY
IN PARTIAL FULFILLMENT OF THE REQUIREMENTS
FOR THE DEGREE OF
DOCTOR OF PHILOSOPHY

Adam E. Cohen
October 2006

I certify that I have read this dissertation and that, in my opinion, it is fully adequate in scope and quality as a dissertation for the degree of Doctor of Philosophy.

W. E. Moerner Principal Co-Adviser

I certify that I have read this dissertation and that, in my opinion, it is fully adequate in scope and quality as a dissertation for the degree of Doctor of Philosophy.

Sebastian Doniach Principal Co-Adviser

I certify that I have read this dissertation and that, in my opinion, it is fully adequate in scope and quality as a dissertation for the degree of Doctor of Philosophy.

Steve Boxer

Approved for the University Committee on Graduate Studies.

Introduction

This thesis describes the development, characterization, and application of the Anti-Brownian Electrokinetic trap (ABEL trap): a device for trapping and manipulating individual nanoscale objects in solution. The ABEL trap works by tracking the Brownian motion of a single fluorescent object of interest, and then applying a feedback voltage to the solution to induce an electrokinetic drift that cancels this Brownian motion.

The ABEL trap is capable of trapping objects far smaller than can be trapped by any other means under comparable conditions. It provides a way to study individual molecules in their native environment, bypassing the perils of surface attachment chemistry. The feedback voltages themselves also provide information along a dimension not usually accessible to single molecule experiments. By analyzing the feedback voltages one can extract time-dependent information about the diffusion coefficient and electrokinetic mobility of the trapped object. Finally, the ABEL trap has potential for use as a small-scale fabrication technology. Trapped objects may be photochemically immobilized, providing a means to form permanent nanoscale structures.

Chapter 1 provides a background on previous trapping technology, electrokinetic phenomena, and the theory of feedback, including some new results on particle-tracking. Chapter 2 describes an implementation of the ABEL trap that uses a high speed camera and real-time image processing to implement the feedback. In Chapter 3 I describe trapping of single molecules of λ-DNA and analyze their mechanical properties. Chapter 4 is a theoretical diversion inspired by the experiments on DNA. It addresses the question, what are the natural ways to describe the shape of a random walk? Chapter 5 is again on instrumentation, describing a scheme that performs the feedback entirely in hardware. The advantage of this scheme is its increased ability to trap very small particles, even down to individual fluorophores. Chapter 6 discusses outstanding theoretical questions and directions for future research.

Here is a list of the papers I wrote on the ABEL trap:

1. A. E. Cohen and W. E. Moerner, "Method for trapping and manipulating nanoscale objects in solution," Appl. Phys. Lett. **86**, 093109, Feb. 28 2005;
2. A. E. Cohen and W. E. Moerner, "The Anti-Brownian Electrophoretic Trap (ABEL Trap): Fabrication and Software," Proc. SPIE **5699**, 2005;
3. A. E. Cohen, "Control of nanoparticles with arbitrary two-dimensional force fields," Phys. Rev. Lett. **94**, 118102, Mar. 25 2005;
4. A. E. Cohen and W. E. Moerner, "An all-glass microfluidic cell for the ABEL trap: fabrication and modelling," Proc. SPIE **5930**, 2005;
5. A. E. Cohen and W. E. Moerner, "Suppressing Brownian motion of individual biomolecules in solution," PNAS **103**, 4362-4365, Mar. 14 2006;
6. A. E. Cohen and W. E. Moerner, "Dynamics of single DNA molecules in equilibrium," *submitted*.

We also filed a patent application, "Sub-micron object control arrangement and approach therefor," which is currently under review.

Acknowledgment

I *enjoyed* doing my PhD at Stanford, and this wasn't because of the lovely view from my office. I enjoyed it because I shared the time with many wonderful supportive friends.

Every thesis involves a huge amount of energy spent on non-productive thrashing, half-completed experiments, and chasing bad ideas. Mine was no exception. Throughout all this, W. E. encouraged me with sound advice, good humor, and admirable sangfroid. He also traveled to the ends of the earth, risking life and limb, in search of funding, molecules, and hard-to-find cables. For all this support, and much more, I am eternally grateful.

The Moerner Lab is populated by great scientists and friendly people. I overlapped with and learned from: Stefanie Nishimura, Kallie Willets, Johann Schleier-Smith, Dave Fromm, Jim Schuck, Jaesuk Hwang, Hanshin Hwang, Kit Werley, So Yeon Kim, Andrea Kurtz, Sam Lord, Nick Conley, Anika Kinkhabwala, Lawrence Klein, Frank Jaeckel, Marcelle Koenig, and Naveen Sinha.

I spent a lot of time in the Stanford Nanofabrication Facility (SNF) and the Physics Machine Shop. In the SNF Mary Tang and Mahnaz Mansourpour were particularly helpful. I thank all the gentlemen in the Machine Shop for helping me out with mechanical advice. I also thank Maria Frank for much friendly and helpful advice on how to stay on the right side of the (physics department) law.

Outside of work, I enjoyed spending time with my roommates Jan, Mark, and Eran and my fellow students in physics. My girlfriend Abby, my parents Audrey and Joel, and my sister Zoe, provided much needed reminders that there is more to life than correlation functions. I thank Bill Golden for his generosity and support.

Finally I thank my thesis committee for coming together on short notice and providing constructive comments on my work: Michael Levitt (chair), W. E. Moerner, Seb. Doniach (physics co-advisor), Steve Boxer, David Goldhaber-Gordon.

I thank the Fannie and John Hertz Foundation for a graduate fellowship and for supporting some non-traditional moves. I thank the Aspen Center for Physics for hospitality while I wrote this thesis. We received funding from the National Science Foundation and the NIH.

Contents

List of Tables

List of Figures

Chapter 1

Background and Theory

One of the outstanding challenges of nanotechnology is to develop a means to trap and manipulate individual molecules in solution. To study a biomolecule one would like to hold the molecule still, to turn it around, to pull on its ends, and to bring it into contact with other molecules—all in a highly controlled manner and in the molecule's native environment. Such a level of control would also allow one to build custom molecular-assemblies designed for specific tasks. The Anti-Brownian Electrokinetic trap (ABEL trap) is a step toward these goals.

This chapter is a summary of the things I had to learn to build the ABEL trap. To motivate the selection of topics I start with a short overview of the ABEL trap and a comparison between the ABEL trap and the clever schemes others have developed for moving small things around. The bulk of the chapter is devoted to studying some pieces of the ABEL trap in detail, focusing on electrokinetics, particle-tracking, control theory, and time-series analysis.

1.1 Overview of the ABEL trap

Fig. 1.1 shows a schematic layout of the ABEL trap. A microfluidic cell forms the heart of the ABEL trap. The center of the microfluidic cell is a disc-shaped trapping region, typically ~ 10 μm wide and < 1 μm deep. Inside the trapping region fluorescent particles diffuse freely in the x-y plane but are mechanically confined in the

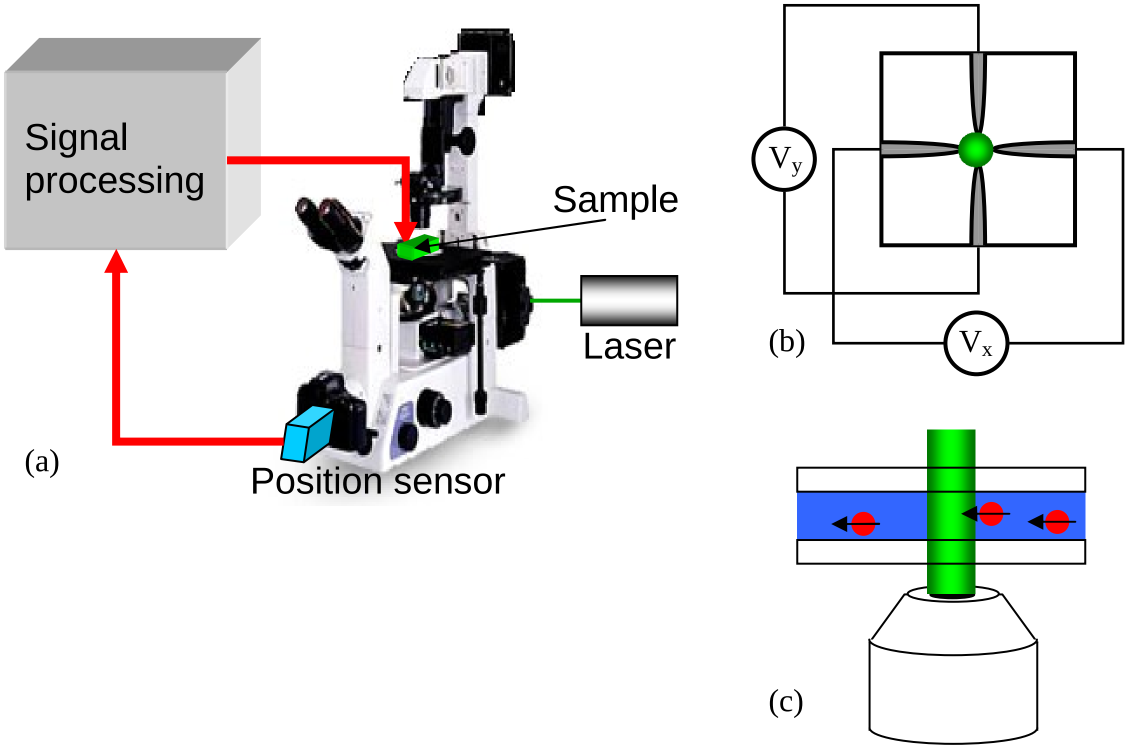

Figure 1.1: Schematic layout of the ABEL trap. a) System configuration. b) Top view of the trapping cell, with the laser spot shown in green in the center. c) side view of the trapping cell.

z-direction. A voltage, $\mathbf{V} = (V_x, V_y)$, applied a set of four control electrodes causes particles in the trapping region to acquire a velocity $\mathbf{v} \propto \mathbf{V}$. The mechanisms by which voltages are transduced into velocities will be discussed in section 1.4. The microfluidic cell is mounted in a fluorescence microscope. A laser illuminates the particles in the trap and a detector collects the fluorescence. I have used several imaging schemes to extract the x and y coordinates of one particle of interest. The abstract principles of single particle tracking are discussed in section 1.5, and specific implementations are described in Chapters 2 and 5. Tracking electronics convert the offset between the measured position and the desired position into feedback voltages, which are applied to the four feedback electrodes.

How tightly can the ABEL trap confine a particle? In section 1.6 I discuss this question in detail. Here is an appetizer. The r.m.s. distance, d, between the actual and target locations has two components: d_f due to the finite restoring force of the trap, and d_r due to the response time of the feedback loop. We now show that typically $d_r \gg d_f$.

Consider the idealized scenario where the feedback is instantaneous. Nonetheless the particle will explore a finite area because there is a maximum electrokinetic velocity that the feedback system can impose. This velocity turns out to be relatively independent of the size or nature of the particle, and in microfluidic geometries is about $v_{max} \approx 10$ mm/s.[98] The instantaneous velocity of Brownian motion is not well-defined, but over a finite interval one can calculate the r.m.s. velocity. In time t a particle diffuses a 1-dimensional mean-squared distance

$$\left\langle d^2 \right\rangle = 2Dt, \tag{1.1}$$

where D is the diffusion coefficient. Thus the r.m.s. velocity of a particle that has diffused a distance d is $v = 2D/d$. Even with instantaneous feedback, the particle can only be confined to an area with linear dimension $d_f = 2D/v_{max}$. The finite restoring force implies a finite relaxation time, $t_f = 2D/v_{max}^2$. Table 1.1 shows that for most objects one might like to trap, the velocity required to confine the object to an area 500 nm in diameter is much less than 10 mm/s.

While the feedback strength is not a severe problem for the ABEL trap, the feedback latency is the limiting factor. A particle can be trapped to an area of dimension $2Dt_r$, where t_r is the response time of the feedback loop. Table 1.1 shows that small objects require feedback bandwidths of several kHz to be trapped. This is a severe requirement on any ABEL trap design.

To estimate the feedback parameters for an object not in Table 1.1, the Einstein-Smoluchowski formula gives the diffusion coefficient of a spherical particle with radius a:

$$D = \frac{k_B T}{6\pi\eta a}, \tag{1.2}$$

where η is the viscosity of the surrounding medium. The viscosity of pure water at room temperature is ~ 1 cP, or 10^{-3} kg/m s in SI units.

The fundamental limit to trapping an individual fluorophore is the finite rate of

Object	D (μm^2/s)	Bandwidth (Hz)	Velocity (μm/s)
1 μm sphere	0.44	3.5	1.8
200 nm sphere	2.2	18	8.8
20 nm sphere	21.8	174	88
2 nm sphere	218	1740	870
Rhodamine 6G	280	2240	1120
water[83]	2850	23000	11000
Macromolecules			
Ribosome 4S (*E. coli*)[121]	37	300	150
γ-Globulin[121]	37	300	150
BSA[82]	49	400	200
Hemoglobin[121]	69	550	275
Myoglobin[121]	100	800	400
Lysozyme[24]	111	890	445
Ribonuclease[121]	131	1050	525

Table 1.1: Table of diffusion coefficients of commonly encountered substances. Tyn and Gusek[121] provide an expanded table with diffusion coefficients for 89 macromolecules and viruses. D is the diffusion coefficient. The feedback bandwidth required for successful trapping within $d_r = 500$ nm is calculated from $1/t_r = 2D/d_r^2$. To counter the Brownian motion, the ABEL trap must impose a velocity with r.m.s. value $v = 2D/d_r$.

photon-detection: it is impossible to know the position of a fluorophore in between photon detection events. To confine a fluorophore with $D \approx 300$ μm^2/s to a distance $d \approx 0.5$ μm requires a photon detection rate, and a feedback bandwidth, of $\sim$ 2400 Hz. A further constraint on trapping single fluorophores is that there cannot be long-lived dark-states. If the molecule goes dark for a time long enough for it to diffuse out of the trap, it is lost. As for all single-molecule fluorescence studies, photobleaching ultimately limits the observation time.

1.2 Manipulating small objects

Laser tweezers have led to a revolution in the fields of nanomanipulation and biophysics. Single-[5, 90] and multiple-[50] beam optical traps have been used to assemble structures from dielectric microparticles;[60] to probe the intrinisic mechanical properties of DNA and RNA;[26, 9, 127] and to probe the action of DNA-processive enzymes.[113, 89] Optical forces have been shown to bias slightly the diffusion of spheres as small as 14 nm[32], but this is at intensities that would rapidly photobleach or otherwise damage sensitive biomolecules. Near an electronic resonance, the polarizability of a molecule can be greatly enhanced, allowing optical forces to bias the diffusion of fluorophores in solution (enhancing the transit time of single Rhodamine 6G molecules across a confocal spot from 1 ms to 2 ms), again at the cost of rapid photobleaching.[92] Although less widespread, magnetic tweezers,[48] and AC dielectrophoresis[124] have also been used to trap and manipulate micron-scale objects. Unfortunately the forces generated by all of these techniques are too weak to trap objects smaller than ~100 nm in solution at room temperature.

Optical trapping, dielectrophoresis, and magnetic tweezers exert very weak forces for two reasons. In each of these techniques, the force scales with the volume of the trapped object: to trap a 10 nm object requires a million times as much input power as to trap a 1-micron object. Also the force arises through a second-order interaction with the applied electric or magnetic field. That is, the field must first polarize the object, and then interact a second time to generate a force between the induced dipole and a gradient in the field. Electrophoretic forces, on the other hand, are much stronger than optical forces. Electrophoresis depends on charge rather than polarizability, and is first order in the field rather than second order. This is why electrophoresis is commonly used to separate biomolecules, and optical forces are not. Electrophoresis has not previously been used to trap biomolecules because an electrophoretic potential contains no minima away from the boundaries (although for particles whose momentum is significant, an AC electric field can dynamically trap a charged particle [2]).

A further drawback of optical trapping techniques is the lack of selectivity. Laser tweezers generate a potential minimum for polarizable objects. Any sufficiently large polarizable object will fall into this minimum and be trapped. Laser tweezers cannot be used in dense dispersions because the trap will become "gummed up" with particles.[3] With very small particles, it is impossible to know for certain how many are trapped in a laser tweezers. The ABEL Trap, in contrast, is guaranteed to trap only a single freely diffusing object. The Brownian motion of distinct freely diffusing objects is uncorrelated, and thus it is impossible to cancel the Brownian motion of more than one object at a time. The ABEL trap can trap any object whose position can tracked optically. The signal from the object of interest may be discriminated from background via fluorescence wavelength, fluorescence lifetime, or software-based image processing. While this thesis focuses exclusively on detection via fluorescence, schemes based on scattering, interference, or absorption are also conceivable.

Scanning probe microscopes (STM[18] and AFM[17]) are another technology often used for nanoscale manipulation.[40] Scanned probes have very high spatial resolution, but are restricted to moving objects on solid surfaces. The sharp tips of scanned probes exert large local forces which may damage soft biomaterials. Finally scanned probes require direct mechanical access to the object being manipulated, with the tip necessarily a few nm away from the object. This may be awkward in complex environments. The ABEL trap suffers from none of these three drawbacks.

The Paul trap[94] and Dehmelt's improvements on the Penning trap[36] allowed scientists to observe individual ions in vacuum for long times. These traps have been used in basic physics to measure the magnetic moment of the electron,[122] and are also widely used as an analytical tool in mass-spectrometry. Arnold and coworkers developed traps that could trap micron-sized charged particles in air at atmospheric pressure, but such traps do not work for particles whose motion is severely overdamped.[2] To-date, no equivalent tool has been developed for studying single molecules in solution.

Biophysicists seeking to study individual molecules have a limited set of options for confining the molecule. One common practice is to immobilize the molecule on a surface.[133] Unfortunately surface chemistry is notoriously finicky, and there is a persistent doubt whether the tied-down molecule acts the same as its free-solution comrades. Another technique is to immobilize the molecule in the pores of a gel,[97] in a liquid droplet,[68] or in a surface-tethered lipid vesicle.[20] However, in each of these cases the molecule may interact with the confining medium, and it is difficult to bring in additional analytes once a molecule has been confined.

Finally, in fluorescence correlation spectroscopy (FCS), molecules in free-solution are observed as they diffuse through a tightly focused laser beam.[58, 46] While these molecules may be in their native environment, the short residence times of FCS (typically a few milliseconds) limit the technique to the study of fast processes. Many biological processes occur on the timescale of seconds to hours. As a concrete example of the problem facing single-molecule researchers, nobody has found a way to observe directly the catalytic cycle of the chaperonin GroEL, which takes 7 - 15 seconds, without disturbing this cycle.

1.3 Feedback Control

Feedback control is widely used to stabilize the motion of stochastic systems, where the stochasticity may arise from quantum, thermal, or manufacturing fluctuations. In particular, feedback may be used to cancel the Brownian motion of a single nanoscale object in solution, over some finite bandwidth. In contrast to passive trapping schemes, feedback trapping has the advantage that the applied potential need not have any local minima.

As early as 1971 Howard Berg developed an automated system for keeping swimming bacteria in the field of view of a microscope.[13] In his apparatus six photomultipliers recorded the x, y, and z coordinates of a bacterium and an analog feedback loop translated the microscope stage to keep the bacterium in focus.

The first proposal to use feedback in single-molecule studies is due to Jörg Enderlein[42]. The avalanche photodiodes (APDs) necessary for efficient single molecule detection are too expensive to use in groups of six, so Enderlein proposed a system with a single APD and a rotating laser focus. A confocal spot is rapidly rotated in a circle, with a radius approximately equal to the radius of the spot. If the molecule is in the center of the circle, it emits a steady flux of fluorescent photons. If the molecule moves off-center, there is a modulation in the fluorescence intensity at the laser rotation frequency. The phase of this modulation, relative to the phase of the laser rotation, indicates the direction in which the molecule has moved. This tracking system is confined to two dimensions (although one could imagine a variant where the laser focus is dithered in the z-dimension too). Enderlein proposed tracking slowly diffusing molecules confined to two dimensions by cellular membranes ($D < 10^{-2} \mu\text{m}^2/\text{s}$). In his proposal the molecule is allowed to diffuse freely, and the center of the laser focus is adjusted to follow the molecule.

One drawback of the Enderlein proposal is that it is difficult to translate the laser focus across a specimen, while still keeping the emitted photons focused on an APD. Andrew Berglund and Hideo Mabuchi built a system that circumvents this difficulty by keeping the laser focus fixed and translating the microscope stage (staying more faithful to the original Berg design).[14] This system uses galvo mirrors to rotate the laser beam at a fixed frequency of 8 kHz and a piezoelectric translation stage to keep the particle in focus. The motion in the z-direction (perpendicular to the focal plane) is constrained simply by squeezing a drop of solution between two coverslips. The Berglund-Mabuchi system can track fluorescent beads down to ~ 60 nm in diameter, but is subject to several drawbacks. The mechanical translation stage is too slow to track very fast objects, and the finite travel of the stage limits the amount of time an object can be tracked. Finally, tracking systems are easily confused by fixed pieces of dirt on a coverslip. As the system follows a particle diffusing over a surface, it is bound to encounter other particles or other bright “goobers” stuck to the surface. Quite frequently the tracking system locks onto one of these fixed objects and loses the moving object of interest. In the ABEL trap, in contrast, the trapping is performed over a fixed spot on the sample cell. It is fairly easy to find a small spot with no fluorescent contamination, or to photobleach the contamination if there is a uniform background of surface adsorbed fluorophores. The ABEL trap also allows one to position a trapped object relative to other fixed objects on the surface, e.g. to probe ligand-substrate interactions. On the other hand, stage-feedback systems are truly non-invasive, so they can be used to track particles diffusing inside cells or other heterogeneous environments.

Recently the group of Haw Yang developed an improved stage-feedback tracking system that can work in three dimensions.[27] They use a quadrant photodiode to detect the position of the particle in the x-y plane, and a slightly defocused confocal pinhole to change z-displacements into intensity variations detected by an APD. This system has been able to track relatively large particles ($\sim$ 250 nm gold beads) and with faster feedback may be able to track smaller particles.

Concurrent with the development of the Berglund-Mabuchi trap, the group of Enrico Gratton built a real-time particle-tracking system based on a two-photon microscope.[70, 73] This device operates on a similar principle (rotating laser focus and Fourier transform based detection), but has the added feature of two detection wavelengths so two differently labelled particles can be tracked simultaneously. Gratton and coworkers also use stage feedback, so they can track particles in cells, but are restricted to tracking slowly diffusing particles.

Subsequent to our initial demonstration of the ABEL trap[33], the group of Ben Shapiro independently developed the idea of using video tracking and electrokinetic forces to steer small particles in solution[30]. Their work uses a camera operating at a relatively slow rate of 40 frames/sec and uses a poly(dimethyl siloxane) (PDMS) microfluidic cell. They only trapped large objects (e.g. yeast cells 4 μm in diameter), and focused on developing a system to trap multiple particles. To achieve this they built microfluidic cells with up to 8 electrodes (capable of controlling 3 particles simultaneously and independently).

1.4 Electrokinetics

Electrokinetic forces provide the muscle for the ABEL trap. What are they, and how can they be controlled? Electrokinetic forces are generally divided into two classes: electrophoretic and electroosmotic. Both kinds of forces play an important role in the ABEL trap.

1.4.1 Huckel Model

Electrophoresis arises from the direct action of an electric field on a charged object. For molecule-scale objects, the electrophoretic velocity is determined by a simple force-balance between viscous drag and electric force. The viscous drag on an object is

$$\mathbf{F}_\gamma = -\gamma \mathbf{v}, \tag{1.3}$$

where $\mathbf{v}$ is the velocity of the object and γ is the friction coefficient. For a spherical particle of radius a in a Newtonian fluid, the friction coefficient is

$$\gamma = 6\pi\eta a. \tag{1.4}$$

For non-spherical objects the friction coefficient may be a complicated function of the geometry of the object. In such cases, the Stokes-Einstein relation provides a simple relation between the drag coefficient and the diffusion coefficient:

$$\gamma = k_B T / D. \tag{1.5}$$

The viscous force is balanced against the electrical force $\mathbf{F}_E = q\mathbf{E}$ to yield the Huckel equation for the steady state velocity in an electric field:

$$\mathbf{v} = \frac{q}{6\pi\eta a}\mathbf{E}. \tag{1.6}$$

The quantity $q/(6\pi\eta a)$ is the mobility, usually denoted μ. It is often convenient to express the mobility in terms of the electrostatic potential on the surface of the particle, ζ, rather than the charge of the particle. If we assume a spherically symmetric charge distribution, the potential is related to the charge by

$$\zeta = \frac{1}{4\pi\epsilon\epsilon_0}\frac{q}{a}, \tag{1.7}$$

where ϵ is the dielectric constant of the medium ($\epsilon = 78.5$ for water at 25° C) and ϵ_0 is the permittivity of free space. The mobility is then

$$\mu = \frac{2\epsilon\epsilon_0\zeta}{3\eta}. \tag{1.8}$$

1.4.2 Smoluchowski model

The picture of a simple force-balance neglects the role of counterions in the solution, which become important for particles larger than a few nanometers in size. The issue is that counterions accumulate around any charged interface, modifying the naked charge of the object. These counterions are also acted on by the electric field, leading to additional flow patterns and electric fields. The counterions lead to two new forces, a "retardation effect" due to fluid flow induced by the motion of the counterions, and a "relaxation effect" due to a modification of the electric field induced by reorganization of the counterions. To understand these effects we must first review the physics of the electrical double layer (Fig. 1.2).

Consider a planar charged surface immersed in an electrolyte solution. In an inhomogeneous potential the concentration of a mobile charged species i obeys

$$C_i = C_i^0 \exp\left(\frac{-z_i e\Phi}{k_B T}\right), \tag{1.9}$$

where z_i is the valence, e is the electron charge, and Φ is the local potential. The region of inhomogeneous potential is assumed to be connected to a vast reservoir of particles at zero potential and with concentration C_i^0. It is almost always the case that the enhancement or depletion of ions near an interface leaves the bulk concentration

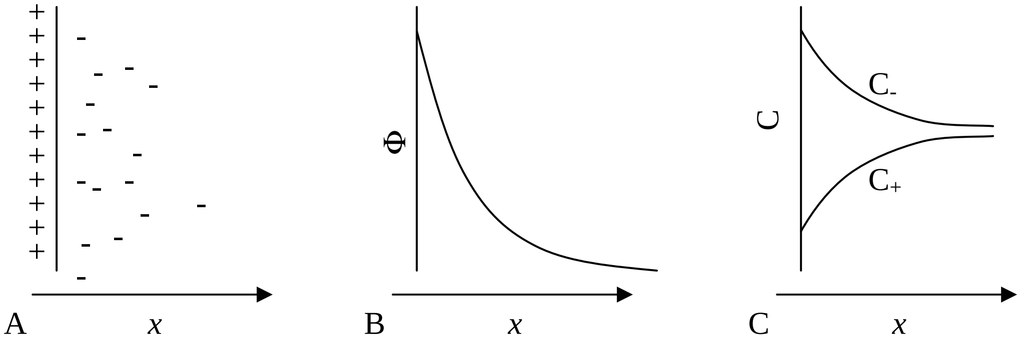

Figure 1.2: Structure of the electric double layer. A) An excess of oppositely charged counterions accumulates near a charged surface. B) The excess counterions screen the charge, causing the potential to drop over a characteristic distance, λ_D. C) Far from the surface the concentrations of all counterions return to their free-solution values.

essentially unchanged.

The excess charge density is

$$\rho = \sum_i C_i z_i e. \tag{1.10}$$

The potential in turn depends on the excess charge density via Poisson's equation. For the planar geometry we are considering here, this becomes

$$\frac{d^2\Phi}{dx^2} = -\frac{1}{\epsilon\epsilon_0}\rho(x). \tag{1.11}$$

Together Eqs. 1.9–1.11 form the coupled Poisson-Boltzmann equation, a nonlinear differential equation. A method of solution for a planar geometry and a 1:1 electrolyte is given in [8]. The result is the Guoy-Chapman formula for the potential distribution in the double layer:

$$\frac{\tanh(ze\Phi/4k_BT)}{\tanh(ze\Phi_0/4k_BT)} = e^{x/\lambda_D}, \tag{1.12}$$

where Φ_0 is the potential on the surface and λ_D is called the Debye length and is given by:

$$\lambda_D = \left(\frac{\epsilon\epsilon_0 k_B T}{2C^0 z^2 e^2}\right)^{1/2}. \tag{1.13}$$

C^0 (Molar)	λ_D (nm)
1	0.3
10^{-1}	0.96
10^{-2}	3.0
10^{-3}	9.6
10^{-4}	30
10^{-7}	960

Table 1.2: Double layer thicknesses for various concentrations of a 1:1 monovalent electrolyte. The last line corresponds to the case of deionized water, for which $[\mathrm{H}^+] = [\mathrm{OH}^-] = 10^{-7}$ M.

Table 1.4.2 gives the double layer thickness for various concentrations of monovalent 1:1 electrolytes.

Under the frequently violated condition that the surface potential is low ($\Phi_0 \ll 50/z$ mV), Eq. 1.12 can be linearized to

$$\Phi = \Phi_0 e^{-x/\lambda_D}. \tag{1.14}$$

For potentials not too much larger than $50/z$ mV, the Guoy-Chapman theory breaks down anyway because it does not take into account the finite size of the ions. In the Guoy-Chapman theory, ions may approach infinitesimally close to the surface, leading to a divergence in the screening charge at large surface potentials. The Stern theory remedies this defect by setting a finite distance of minimum approach, but we don't need to go into it here.

For a colloidal particle, the above analysis applies provided that the radius $a \gg \lambda_D$. Then one can think of the surface as essentially planar. Table 1.4.2 shows that this condition applies in standard buffers for objects larger than a few nanometers in diameter.

Now let's apply an external electric field. For an insulating particle in a conducting medium, the steady-state electric field must be tangential to the surface of the particle. Consider a thin sheet of solution of area A and thickness dx, parallel to the surface of the particle. The viscous force required to shear this sheet at a uniform rate is

$$F_v = \eta A \frac{dv}{dx}. \tag{1.15}$$

If this sheet has an excess charge density ρ then the electric force on it is

$$dF_E = \rho E A \, dx. \tag{1.16}$$

Differentiating Eqs. 1.15 and 1.16 with respect to x and requiring force balance yields

$$\rho E = \eta \frac{d^2 v}{dx^2}. \tag{1.17}$$

Substituting in the Poisson Equation 1.11 we obtain

$$\frac{d^2 v}{dx^2} = -\frac{\epsilon\epsilon_0 E}{\eta} \frac{d^2 \Phi}{dx^2}, \tag{1.18}$$

which upon integration across the double layers yields the Smoluchowski Equation:

$$v = v_0 + \frac{\epsilon\epsilon_0 \zeta}{\eta} E, \tag{1.19}$$

where ζ is the potential at the plane of shear—the point within the double layer where the "no-slip" boundary condition is applied and the fluid starts to flow according to Eq. 1.15. We will not be upset by the fact that in real systems the fluid velocity does drop instantaneously to zero on the surface of the particle: usually one measures the electrophoretic mobility and then applies the Smoluchowski Equation 1.19 to extract the ζ-potential.

It is found experimentally that $|\zeta| < |\Phi_0|$, where Φ_0 is the surface potential in Eqs. 1.12 and 1.14. The explanation is that ions can penetrate right up to the surface of the solid, but the innermost ions are not mobile, so they merely reduce the effective charge of the particle without contributing to electroosmotic flow.

Eq. 1.19 says that there is a velocity difference between the solid surface and the bulk solution. This applies equally to field-induced motion of fluid in a fixed capillary (electroosmosis) or to motion of a particle in a fluid at rest (electrophoresis). In either case one defines the electrokinetic mobility

$$\mu = \frac{\epsilon\epsilon_0\zeta}{\eta}. \tag{1.20}$$

Eq. 1.20 includes the retardation effect and is the same as Eq. 1.8, apart from a numeric factor of 2/3.

1.4.3 Corrections to Smoluchowski

In 1931 Henry developed a generalized version of Eq. 1.19 to interpolate between the limits $a/\lambda_D \ll 1$ (Eq. 1.8) and $a/\lambda_D \gg 1$ (Eq. 1.20).[56] His formula is

$$\mu = \frac{2\epsilon\epsilon_0\zeta f(a/\lambda_D)}{3\eta}, \tag{1.21}$$

where the Henry function $f(a/\lambda_D)$ varies smoothly between 1 for $a/\lambda_D \ll 1$ and 1.5 for $a/\lambda_D \gg 1$.

Two further effects under the heading “relaxation forces” modify the mobility beyond Eq. 1.21: double layer polarization and concentration polarization. Double layer polarization is a distortion of the double layer by the applied electric field. This effect is significant when the surface conductivity of the double layer is large compared to the bulk conductivity in the solution (times the particle radius a). Then one can think of the double layer as a partially conducting Faraday cage that screens some of the applied field and leads to a lower mobility than expected from Eq. 1.21. In 1948 Henry[57] and Booth[19] independently developed a formalism for double layer screening and subsequently Wiersema *et al.*[131] and O’Brien and White[91] performed numerical simulations to solve the nonlinear PDEs that arise in this context.

The ions that cause the charge imbalance responsible for double layer screening come from the bulk solution. One side of the particle acts as a sink for these ions and the other side acts as a source. As a result, a bulk concentration imbalance develops extending a distance of order a from the particle. This secondary imbalance leads to an additional electric field which further modifies the mobility of the particle. A great deal of work over the past century has gone into finding an accurate expression for the electrokinetic mobility of a charged sphere in an electrolyte solution.

The analytical challenge of predicting μ becomes much harder when $e\zeta \geq k_B T$ because then it is no longer appropriate to use the linearized Poisson-Boltzmann equation. Formulas valid for all ζ and all size objects are a topic of current research. Furthermore, with polyvalent counterions the Poisson-Boltzmann equation itself ceases to be valid. The problem is that the Poisson-Boltzmann equation is a mean-field equation: it only deals with average potentials and concentrations. However, when the interactions between ions become sufficiently strong, the motion of ions becomes correlated, so transient fluctuations in the charge density become important. Of particular interest is the "charge inversion" phenomenon in which high z counterions may condense on a colloid and actually reverse the sign of its total charge, leading to a "backwards" mobility.[51]

1.4.4 Dynamic Electrophoresis

The discussion of electrokinetics thus far has been restricted to steady-state behavior. Indeed, the bulk of the electrokinetic literature deals with steady-state phenomena, since these are principally of interest in capillary electrophoresis and other chromatographic applications. However, for the ABEL trap we need to understand dynamic electrophoresis. We measure the particle to be at a location other than where we want it, and apply a corrective electric field. How long does the particle take to reach its steady state velocity?

Each of the effects discussed above has a characteristic time associated with it.[84] Relaxation times can be grouped into two categories: hydrodynamic and electrodynamic. Water cannot support shear waves; instead transverse disturbances propagate diffusively. This process of hydrodynamic relaxation is governed by the diffusion of vorticity, $\upsilon = \nabla \times \mathbf{v}$. The vorticity of a two-dimensional flow subject to irrotational body forces obeys a diffusion-like equation

$$\frac{dv}{dt} = \sqrt{\frac{\eta}{\rho}}\nabla^2 v, \tag{1.22}$$

where ρ is the fluid density and the quantity η/ρ is called the kinematic viscosity and plays the role of a diffusion coefficient. For water at 20° C, $\eta/\rho = 10^6$ μm^2/s. We can now make simple estimates of the time to reach hydrodynamic equilibrium. For a channel of thickness h, an electroosmotic flow initiated at the walls of the channel will take a time

$$\tau_{eo} \approx \frac{\rho h^2}{2\eta} \tag{1.23}$$

to diffuse to the center of the channel. For the 1 μm channels typical of the ABEL trap, we find $\tau_{eo} \approx 1$ μs. When a particle moves, the viscous drag it experiences is due to shear spread over a characteristic distance a. To set up this flow-field requires a time

$$\tau_p \approx \frac{\rho a^2}{2\eta}. \tag{1.24}$$

Since $a < h$ (the particle must fit in the channel), we have $\tau_p < \tau_{eo}$. For a typical value of $a = 100$ nm, $\tau_p \approx 10$ ns.

Now we look at the electrodynamic relaxation processes. In order to establish a polarization of the double layer (the Henry-Booth effect, Sec. 1.4.3), ions from the solution must diffuse a distance of order the thickness of the double layer. This takes a time

$$\tau_{dl} \approx \frac{\lambda_D^2}{2D} \tag{1.25}$$

where D is the diffusion coefficient of the counterions. For $\lambda_D = 10$ nm and $D = 500$ μm^2/s, $\tau_{dl} \approx 100$ ns. The ions that polarize the double layer are taken from the bulk solution, leading to the concentration polarization effect. This concentration imbalance extends over a distance of order the particle size, so the time to establish concentration polarization is

$$\tau_{cp} \approx \frac{a^2}{2D}. \tag{1.26}$$

For $a = 100$ nm, this time is $\tau_{cp} \approx 10$ μs. Mangelsdorf and White, and more recently

Hill *et al.* performed numerical simulations of colloidal particles in AC electric fields, and found fairly flat frequency response up to frequencies of 10^5 Hz for 100 nm particles. Smaller particles would be expected to have even faster responses. The highest frequency electrical signals applied by the ABEL trap are 40 kHz, so for our purposes we can consider the response to be instantaneous.

1.4.5 Practical considerations in electrophoresis

In capillary electrophoresis, and more generally whenever one wants to manipulate small particles using electric fields, an applied electric field sets up both a bulk electroosmotic flow and an electrophoretic drift.[69] The total velocity of the particle is the sum of the electrophoretic and electroosmotic velocities. If the particle is large compared to the Debye length and is chemically identical to the capillary walls, then the net electrokinetic mobility of the particle is zero: the electrophoretic and electroosmotic velocities exactly cancel. This exact cancellation rarely occurs in practice. For highly charged analytes, one generally wants to minimize electroosmotic flow so that the measured mobility reflects intrinsic properties of the particle (i.e. its ζ-potential). On the other hand, for neutral analytes, electroosmosis provides the only "handle" for applying the feedback, and thus it is necessary to have a strong electroosmotic flow.

A number of factors can modify the electrophoretic and electroosmotic mobilities. In contrast to pressure driven flows, much of the shear in electrokinetic phenomena occurs within λ_D of the surface. Thus the viscosity that appears in Eq. 1.21 is the *surface* viscosity within the first few nanometers of the solid-liquid interface. This viscosity may be considerably increased via the addition of neutral brushlike polymers that stick via physical or chemical interact with the surface. By changing the ionic strength, one can affect how much of the double layer falls within the region of high surface viscosity. Meanwhile, charged species that adsorb to the surface can change the ζ potential and thereby affect the electroosmotic flow. The pH also affects electroosmotic flow by determining the protonation state of surface groups.

The ability to tune the electrokinetic and surface adsorption properties of a channel depends on the channel material. Most microfluidic devices (and all the sample cells for the ABEL trap) are either made of a soft polymer, such as poly(dimethyl siloxane) (PDMS), or a hard material such as glass or fused silica. PDMS has a naturally hydrophobic surface and develops a negative surface charge in water. PDMS has been modified by exposure to oxygen plasma; silanization; adsorption of proteins; and covalent modification (for a review see [80]). In particular, UV driven surface polymerization with charged monomers can make the surface stably hydrophilic and can even reverse the sign of the surface charge.[61] Liu *et al.* also demonstrated the ability to eliminate or reverse the sign of electroosmotic flow in PDMS through physical adsorption of mixed Polybrene/Dextran Sulfate polymers.[76] Surface oxidation is the easiest way to control the electroosmotic flow in PDMS. Brief exposure to a plasma of room-air or to a corona discharge renders the surface hydrophilic. The modified surface supports strong electroosmotic flow, but reverts to hydrophobic over less than an hour if exposed to room-air.

Glass and quartz capillaries can be dynamically modified by adsorption of cellulose derivatives, surfactants,[120] lipid bilayers, or poly(vinyl alcohol)[11] or covalently modified with a number of polymers[12]. PH can strongly modify the ζ potential,[45] as can seemingly inert counterions. For instance, the ζ potential of glass was varied between -88 to -66 mV by addition of KCl and $LaCl_3$. The same salts varied the ζ potential of PDMS from -110 mV to -68 mV. [116]. The large dielectric constant of water weakens internal electric fields, so one might hope that organic solvents with their lower dielectric constants would support higher electroosmotic mobilities. Alas Schwer and Kenndler experimentally showed that this is not the case.[108] Special purpose cationic coatings have also been designed to prevent DNA adsorption.[75]

In addition to modifying the electroosmotic mobility, surface coatings are often selected to minimize interaction between an analyte and the walls of a capillary. Surface adsorption is a particularly sticky issue in the ABEL trap. The hydrophobic surface of PDMS strongly adsorbs hydrophobic species from solution, and many small dye molecules will actually be absorbed into the PDMS, gradually increasing the fluorescence background. The frequency with which a particle in the trapping region collides with the walls of the trap is $f = 2D/h^2$, where h is the depth of the trapping region. The depth of the trapping region is typically between 100 nm and 1 μm; much smaller than in most microfluidic devices. Thus the rate of collisions is higher, and so is the probability that a given particle will adsorb to the surface. For a typical scenario with $h = 200$ nm and $D = 20$ μm^2/s, a particle collides with the walls of the trap roughly 1000 times per second. Adsorbed particles change the surface chemistry of the trap and contribute to an increased fluorescence background. In the very dilute solutions typically used for trapping, adsorption may completely deplete the solution of fluorescent particles. For all of the above reasons, it is important to minimize the affinity of particles for the walls of the trap.

1.4.6 Electrophoresis in two dimensions

Electrophoresis is typically considered a 1-dimensional process: one measures the relative mobilities of different components of a solution either along a capillary or in a gel. Even in 2-D electrophoresis, the two separations are run sequentially, each as a 1-D process. Life becomes modestly more interesting when performing electrophoresis in two dimensions simultaneously.

Given n electrodes in a solution, one has $n - 1$ degrees of freedom in determining the electric field (adding a constant potential to all the electrodes does not affect the field). To create an arbitrary 2-D electric field, in principle one only needs three electrodes. In practice it is more convenient to use four electrodes with bipolar driving: when a potential $+V$ is applied to one electrode, the potential $-V$ is applied to its opposing partner. But with four electrodes there should be three degrees of freedom. Where is the third degree of freedom?

Fig. 1.3 illustrates the situation. In addition to the linear fields E_x and E_y, there is also a quadrupolar field E_q generated by applying $+V$ to one set of opposing electrodes and $-V$ to the other set. This quadrupolar field has a zero at the center of the trap. The electroosmotic flow generated by this field is a purely extensional flow that can be used to stretch or orient anisotropic objects. While there is current interest in the behavior of polymers in quadrupolar fields and extensional flows, I

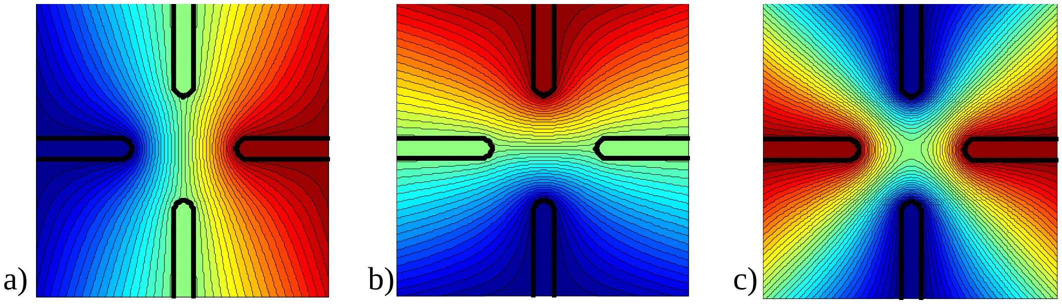

Figure 1.3: Three modes of the electric field in the ABEL trap. The contour lines represent equipotential surfaces. a) Horizontal mode. b) Vertical mode. c) Quadrupolar mode. Solid black lines indicate the electrode boundaries. Simulations were performed by solving Poisson's equation in two dimensions using homemade code written in Matlab.

always kept $E_q = 0$.[64, 110]

Now that we have discussed how and why a particle in solution moves in response to a field, we turn to the other part of the ABEL trap: monitoring the motion of the particle as quickly and accurately as possible. For the purposes of this thesis, the ultimate goal is to trap individual molecules, which requires single-molecule imaging.

1.5 Particle Tracking

In his original treatise of Brownian motion[23] Robert Brown observed that when ground up small enough, particles of all manner showed random jiggling in solution.[1] This phenomenon remained unexplained until Einstein's famous 1905 paper[41] in which he explained

> Bodies of a microscopically visible size suspended in liquids must, as a result of thermal molecular motions, perform motions of such magnitude that they can be easily observed with a microscope.

By following the Brownian motion of a small object in solution, one can learn about its properties and about its interaction with the environment. Single particles

---

[1] Brown called these small particles "Molecules" because they appeared to have a well-defined smallest size. In fact he had discovered the diffraction limit of his microscope.

can be detected using the broad array of microscopic imaging methods that have already been developed in the Moerner laboratory and elsewhere.[85, 86, 87] Automated video tracking schemes have recently taken much of the drudgery out of this task, allowing determination of diffusion coefficients and other transport properties on the single particle level. Since the first report of tracking single molecules in cells[106], there have been countless applications to understanding problems in biology.[49, 125] Critical to the ABEL trap, however, is precise determination of position of a single fluorophore freely diffusing in water. This goal has not previously been achieved. To reach it, we need to look carefully at the constraints and errors in particle tracking.

1.5.1 Tracking accuracy

Qian and coworkers first developed a statistical formalism for interpreting Brownian trajectories recorded by video [99]. This work did not consider the details of the video capture process, namely the finite exposure time during each video frame, nor the possible role of measurement noise. Savin and coworkers recently addressed these two issues [105], but omitted some important details that will be taken up here.

Standard video-tracking of a diffusing particle is subject to some systematic biases that, to my knowledge, have not previously been described. An understanding of these biases is crucial to developing a quantitative model of the ABEL trap, as well as to interpreting correctly all manner of particle-tracking experiments. In this section I study the statistical properties of the recorded trajectory of a particle undergoing a pure random walk.

No tracking system can measure the instantaneous location of a particle. Instead, every system has some finite “exposure time” during which it collects photons. The reported location of the particle is actually the location of its center of mass averaged over the exposure. In modern video tracking systems, and especially in the ABEL trap, this exposure time is a sizeable fraction of the frame time (up to 90 % is typical). A large exposure time is good because it maximizes the number of detected photons; but the cost is statistical complexity in the data. Here is why.

Consider a particle moving in only one dimension with a diffusion coefficient D

(the results derived below generalize trivially to two dimensions). The mean-square displacement of the particle over a cycle of length T is $2DT$. Suppose that during each cycle the center of mass position is calculated by averaging over a time $\tau < T$. The surprising fact is that the center of mass *does not* diffuse a mean-square distance $2DT$ over one cycle. We now calculate how far the center of mass diffuses.

Suppose the particle starts at $x = 0$ at time $t = 0$ and we perform an exposure of duration τ. We now calculate mean-square displacement of the center of mass of this time-lapse image. In the absence of deterministic drift, the particle obeys the Langevin equation:

$$\frac{dx}{dt} = \xi_0(t), \tag{1.27}$$

where $\xi_0(t)$ is Gaussian white noise with mean zero and covariance

$$\langle \xi_0(t)\xi_0(t')\rangle = 2D\delta(t - t'). \tag{1.28}$$

The random variable $\xi_0(t)$ is the mathematical manifestation of the countless thermal collisions that cause Brownian motion. The position of the particle at time t is

$$x(t) = \int_0^t \xi_0(t')\, dt'. \tag{1.29}$$

The position of the center of mass is

$$\begin{aligned} x_{CM} &= \frac{1}{\tau}\int_0^\tau x(t)\, dt \\ &= \frac{1}{\tau}\int_0^\tau dt \int_0^t dt'\, \xi_0(t'). \end{aligned} \tag{1.30}$$

Thus we have

$$\begin{aligned}\langle x_{CM}^2\rangle &= \frac{1}{\tau^2}\int_0^\tau dt\int_0^t dt'\int_0^\tau dt''\int_0^{t''} dt'''\,\langle\xi_0(t')\xi_0(t''')\rangle\\ &= \frac{1}{\tau^2}\int_0^\tau dt\int_0^t dt'\int_0^\tau dt''\,2D\Theta(t''-t')\\ &= \frac{1}{\tau^2}\int_0^\tau dt\int_0^t dt'\,2D(\tau-t')\\ &= \frac{1}{\tau^2}\int_0^\tau dt\,2D\tau t-Dt^2\\ &= \frac{2D\tau}{3}.\end{aligned} \tag{1.31}$$

In going from the first to the second line of Eq. 1.31 the Θ unit-step function appears because the δ-function from Eq. 1.28 only contributes when both of its arguments are in the domain of integration.

The result of Eq. 1.31 is also the mean-square separation between the center of mass of the time-lapse image and the location of the particle at the *end* of the exposure. Between the end of one integration period and the beginning of the next, the particle undergoes diffusion for a time $T-\tau$ and thus diffuses a mean-square distance $2D(T-\tau)$. Then a new integration period begins and the center of mass is measured to be a mean-square distance of $2D\tau/3$ from the position at the start of the integration. Thus the variance in the displacement $\Delta x[n]\equiv x[n]-x[n-1]$ is:

$$\begin{aligned}\langle\Delta x[n]^2\rangle &= \frac{2D\tau}{3}+2D(T-\tau)+\frac{2D\tau}{3}\\ &= 2D\left(T-\frac{1}{3}\tau\right).\end{aligned} \tag{1.32}$$

This non-intuitive result illustrates the potential for systematic biases in the estimation of diffusion coefficients from video-tracking data.

A further consequence of the finite integration time τ is that successive displacements of the particle (i.e. $\Delta x[n]$ and $\Delta x[n+1]$) are not statistically independent. Here is a simple way to see that this must be the case. If the displacements were independent, then from Eq. 1.32 one would expect the mean-square displacement after N

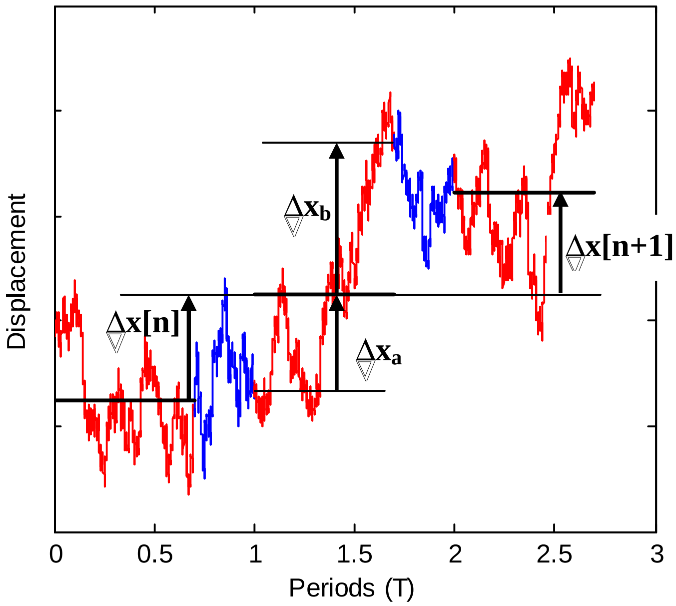

Figure 1.4: Timing diagram for measurements of a particle diffusing in 1-D. The red parts of the trajectory indicate integration times of length τ. The position of the particle reported at the end of one integration time is its average center of mass during that integration time (horizontal bold lines). Δx_a is the displacement between the start of the integration time and the center of mass and Δx_b is the displacement between the center of mass and the end of the integration time. The correlation between Δx_a and Δx_b introduces a correlation between $\Delta x[n]$ and $\Delta x[n+1]$.

measurement cycles to be $2ND(T - \tau/3)$. On the other hand, the argument used to justify Eq. 1.32 can be extended to apply to a long period of free diffusion bracketed by a first and an N^{th} measurement period. Then one would expect the mean-square displacement to be $2D(NT - \tau/3)$, which is in fact the correct answer. The error in the first approach (summing N mean-square displacements) must be that successive displacements are not statistically independent.

Now we calculate the correlation between successive measured displacements, $\langle \Delta x[n] \Delta x[n+1] \rangle$. The correlation arises because the same chunk of the trajectory used to calculate x[n] influences both $\Delta x[n]$ and $\Delta x[n+1]$. Fig. 1.4 illustrates this principle.

Using the notation of Fig. 1.4 we have

$$\Delta x_a = \frac{1}{\tau}\int_0^\tau dt \int_0^t dt'\, \xi_0(t') \tag{1.33}$$

and

$$\Delta x_b = \int_0^\tau \xi_0(t)dt - \Delta x_a. \tag{1.34}$$

The product $\langle \Delta x_a \Delta x_b \rangle$ can be evaluated in much the same way as Eq. 1.31. The result is

$$\langle \Delta x_a \Delta x_b \rangle = \frac{D\tau}{3}. \tag{1.35}$$

The measured displacements $\Delta x[n]$ and $\Delta x[n+1]$ have other contributions besides Δx_a and Δx_b, but these contributions are independent of each other so $\langle \Delta x[n]\Delta x[n+1]\rangle$ is also given by Eq. 1.35.

Here is a summary of the statistical properties of the measured displacement of a freely diffusing particle

$$\langle \Delta x[m]\Delta x[n]\rangle = \begin{cases} 2D(T-\tau/3) & \text{if } n = m \\ D\tau/3 & \text{if } |n-m| = 1 \\ 0 & \text{otherwise.} \end{cases} \tag{1.36}$$

The first line of Eq. 1.36 was given in [105], but those authors neglected the autocorrelation at lag 1. Due to the finite autocorrelation at lag 1 in Eq. 1.36, the apparent Brownian noise is *not* white. One interpretation of this is that the finite integration time τ causes aliasing of high frequency components of the Brownian noise into the measurement band. Eq. 1.36 shows that any realistic measurement of a diffusing particle shows nontrivial statistical behavior at short lags. This behavior must be included in an accurate analysis of diffusive trajectories.

1.5.2 Measurement noise

It is impossible to measure the position of a particle with perfect accuracy. Measurement errors may be especially significant for dim or quickly moving objects. A realistic model of a particle-tracking system must take these errors into account.

Even in the absence of electronic noise or imperfect instrumentation, a particle tracking system is limited by the optical resolution of a microscope. If the microscope has a Gaussian point spread function (PSF) with width σ, then a stationary particle that emits N photons during an integration time can be localized with an accuracy of $\sigma/\sqrt{N}$.[119] Thus the best a tracking system can hope for is to locate a particle to within $\chi_0 = \sigma/\sqrt{N}$, where N is the number of photons detected in interval τ. In reality, the measurement uncertainty $\chi > \chi_0$ due to background photons, electrical noise, imperfections in the optics and optical alignment, and so on. Let us assume that all noise sources enter as Gaussian white noise with standard deviation χ.

Suppose a particle is freely diffusing and its position is being measured by a noisy detector. The equations governing this situation are:

$$\begin{aligned} x^*[n+1] &= x^*[n] + \xi[n] \\ x[n] &= x^*[n] + \chi[n], \end{aligned} \tag{1.37}$$

where $x^*[n]$ is the position that would be measured with a finite exposure time but in the absence of measurement noise, $\xi[n]$ is Gaussian non-white noise with covariance of Eq. 1.36, and $x[n]$ is the measured position of the particle. What are the statistical properties of the steps $\Delta x[n] \equiv x[n] - x[n-1]$?

The variance is

$$\left\langle \Delta x^2 \right\rangle = \left\langle \xi^2 \right\rangle + 2\left\langle \chi^2 \right\rangle; \tag{1.38}$$

the covariance at lag 1 is

$$\left\langle \Delta x[n] \Delta x[n+1] \right\rangle = \left\langle \xi[n]\xi[n+1] \right\rangle - \left\langle \chi^2 \right\rangle; \tag{1.39}$$

and all other covariances are 0. Thus we see that a finite shutter time and measurement noise both modify the covariance in the measured displacements of a purely Brownian particle at lags -1, 0, and 1. However, there is an important result if one wishes to obtain accurate diffusion coefficients from data subject to the above sources

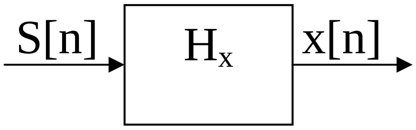

Figure 1.5: Block diagram of a causal, linear, discrete time, time-invariant system.

of contamination:

$$\sum_{m=-1}^{1} \langle \Delta x[n] \Delta x[n+m] \rangle = 2DT. \tag{1.40}$$

This formula provides an unbiased estimate of the diffusion coefficient, even if one does not know the exposure time τ or the error in the position measurements, $\langle \chi^2 \rangle$.

1.6 Control Theory

Having reviewed the basic elements of the ABEL trap, we now go to a higher level of abstraction to study the properties of feedback systems in general. Many excellent books have been written on control theory [107, 25, 6]; particularly useful is the tutorial on control theory for physicists by Bechhoefer.[10]. Here I focus only on the aspects relevant for cancelling Brownian motion. We start by considering a causal, linear, discrete time, time-invariant system, x, with input $S[n]$ and output $x[n]$ (Fig. 1.5).

Let's discuss the constraints on the system. Causality is guaranteed: the output of every system depends only on inputs received at earlier times. Linearity means that if $S_1[n]$ causes $x_1[n]$ and $S_2[n]$ causes $x_2[n]$, then the input $aS_1[n] + bS_2[n]$ causes output $ax_1[n] + bx_2[n]$ for all real a and b. This is an approximation, and we will encounter many systems where this approximation breaks down in interesting ways.

We focus on discrete time systems, where $n = \ldots, -1, 0, 1, 2, \ldots$. All data analysis will be done on discretized data, and one may safely assume that a continuous time system can be approximated by a discrete time system if time is subdivided finely enough.

Finally, time-invariance means that the response is a function only of the time interval between stimulus and response, and not a function of time in an absolute sense. This constraint is violated whenever the system x has internal dynamics. Depending on which state you catch it in, its response may be different. This deviation from time-invariance will be of particular interest later on because it will provide a window into the internal dynamics of molecules held in the ABEL trap.

Assuming all the above conditions hold, the most general relation between the input of the system and the output is:

$$x[n] = \sum_{m=0}^{\infty} H_x[m] S[n-m], \tag{1.41}$$

where $H_x[m]$ is the impulse response function of system x. If S is a s-dimensional vector and x is a q-dimensional vector, then for each value of m, $H_x[m]$ is a $q \times s$ matrix. We will typically assume S and and x are scalars.

When many systems are interconnected in a possibly complicated way, the generalization of Eq. 1.41 becomes clumsy to handle in the time-domain. It is better to take a Z-transform, defined by:

$$\tilde{x}(z) \equiv \sum_{n=-\infty}^{\infty} x[n] z^{-n} \tag{1.42}$$

and its inverse

$$x[n] = \frac{1}{2\pi i} \oint \tilde{x}(z) z^{n-1} dz, \tag{1.43}$$

where the integral is taken around any circle in the complex plane centered at the origin and in the region of convergence of $\tilde{x}(z)$ (we indicate variables in the Z domain with a "∼"). In the Z domain, Eq. 1.41 takes the much simpler form

$$\tilde{x}(z) = \tilde{H}_x(z) \tilde{S}(z). \tag{1.44}$$

Concatenation of elements with different response functions is accomplished simply by multiplying the Z-transformed response functions and then taking the inverse Z transform.

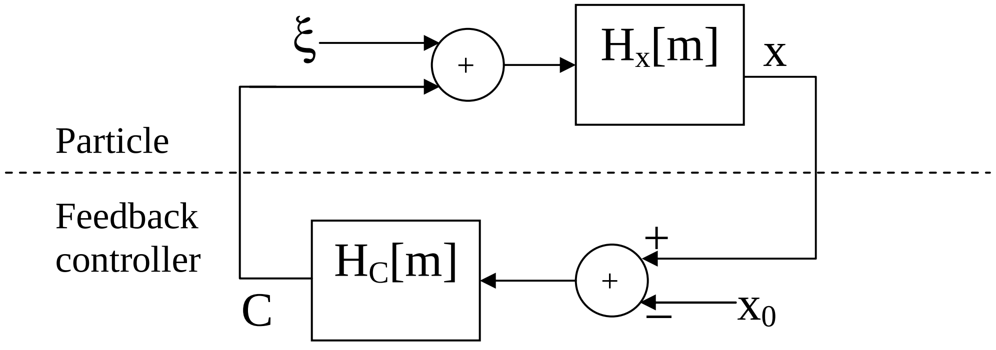

Figure 1.6: Simplest idealized system for canceling Brownian motion in one dimension. x represents the location of the particle with impulse response $H_x[m]$ and C represents the response of the control system with impulse response $H_C[m]$.

1.6.1 Simplest control model

We start with an idealized feedback system in 1 dimension. This system demonstrates the essential features of feedback control, without the complications of realism. Later subsections will generalize this model to more realistic scenarios.

Let $x[n]$ represent the position of the particle at time n, and $C[n]$ represented the output of a feedback controller. The response function of the particle is $H_x[m]$ and the response function of the controller is $H_C[m]$. The position of the particle is subject to some noise, e.g. from Brownian motion, while the feedback controller seeks to keep the particle at location $x_0[n]$. A picture of the situation is given in Fig. 1.6.

When everything is expressed in the Z domain, the system is described by a set of algebraic equations:

$$\begin{aligned} \tilde{x} &= \tilde{H}_x \left(\tilde{\xi} + \tilde{C} \right) && (1.45) \\ \tilde{C} &= \tilde{H}_C \left(\tilde{x} - \tilde{x}_0 \right), && (1.46) \end{aligned}$$

where the z dependence has been omitted for simplicity. These equations are easily solved to yield:

$$\tilde{x} = \frac{\tilde{H}_x \tilde{\xi} - \tilde{H}_x \tilde{H}_C \tilde{x}_0}{1 - \tilde{H}_x \tilde{H}_C}, \tag{1.47}$$

and

$$\tilde{C} = \frac{\tilde{H}_C \tilde{H}_x \tilde{\xi} - \tilde{H}_C \tilde{x}_0}{1 - \tilde{H}_C \tilde{H}_x}. \tag{1.48}$$

These are the fundamental equations describing the response of a discrete-time feedback system. We will return to them often, with various models for the response functions $\tilde{H}_C$ and $\tilde{H}_x$.

At this high level of abstraction, Eqs. 1.47 and 1.48 do not have much intuitive meaning. One key feature to notice is the potential for disaster in the denominators. If $\tilde{H}_C \tilde{H}_x = 1$ for any z, the denominator blows up and the system becomes unstable. Given some knowledge of the range of values of $\tilde{H}_x$ one expects to encounter, one must design the controller to keep $\tilde{H}_C \tilde{H}_x > 1$. Ideally one approaches the limit of $\tilde{H}_C \tilde{H}_x \gg 1$. Then Eqs. 1.47 and 1.48 take on the pleasing form:

$$\begin{aligned} \tilde{x} &\approx \tilde{x}_0 - \frac{\tilde{\xi}}{\tilde{H}_C} && (1.49) \\ \tilde{C} &\approx -\tilde{\xi} + \frac{\tilde{x}_0}{\tilde{H}_x}. && (1.50) \end{aligned}$$

That is, the particle resides approximately at x_0, with the thermal fluctuations damped by a factor of H_C. The output of the controller is then very nearly equal and opposite to the noise, ξ.

1.6.2 More realistic control model

Fig. 1.7 shows the timing diagram for a realistic feedback controller. The controller operates on a cycle of length T. There are two parts to the controller that operate simultaneously. The measurement section (top row in Fig. 1.7) calculates the location of the center of mass of the particle, averaged over some finite integration time τ. During this interval, the particle undergoes Brownian motion due to thermal collisions, as well as deterministic linear motion due to the applied voltage. The feedback section (bottom row in Fig. 1.7) calculates a feedback voltage that is applied after a delay of ρT from the midpoint of the observation time.

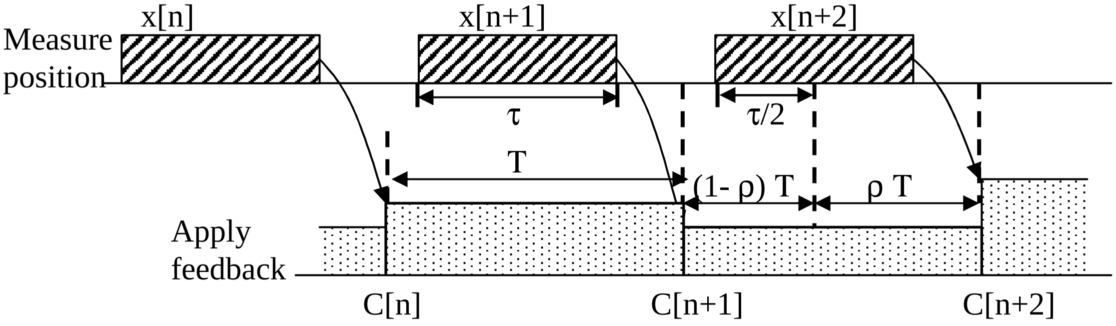

Figure 1.7: Timing diagram of a realistic discrete-time feedback system. The system operates on a cycle of length T. The position of the particle (top row) is obtained by averaging for a finite observation time τ during each cycle. There is a delay of ρT between the midpoint of an observation time and the application of the corresponding feedback voltage. Because the electric field switches at a point in between two observations of the particle, the displacement of the particle depends on two consecutive feedback voltages.

In a constant electric field E the particle undergoes deterministic motion at constant velocity μE. Therefore the measured position of the center of mass of the particle is (on average) equal to its position at the midpoint of the integration time.

Our tracking system only measures the location of the particle at discrete intervals, so we want a discrete equation of motion. This is easily obtained by examination of the timing diagram of Fig. 1.7. The position of the particle obeys:

$$x[n+1] = x[n] + \rho\mu E[n-1]T + (1-\rho)\mu E[n]T + \xi[n], \tag{1.51}$$

where ρ is the fraction of a cycle between the midpoint of a position measurement and the application of the feedback voltage. The *discrete time* Brownian noise has covariance given by Eq. 1.36.

With linear proportional feedback, the electric field is

$$E[n] = -A(x[n] - x_0[n]), \tag{1.52}$$

where A is a user-set gain and x_0 is the target position for the particle.

The coupled finite-difference equations 1.51 and 1.52 are solved by transforming to the Z domain. We make use of the fact that for any function $x[n]$ the Z transform of $x[n-n_0]$ is $z^{-n_0}\tilde{x}(z)$. Thus we have:

$$\begin{aligned} \tilde{E} &= -A(\tilde{x}-\tilde{x}_0) && (1.53)\\ z\tilde{x} &= \tilde{x}+\rho\mu z^{-1}\tilde{E}T+(1-\rho)\mu\tilde{E}T+\tilde{\xi}, && (1.54)\end{aligned}$$

where the explicit z dependence has been omitted for simplicity. These equations are simple to solve algebraically, yielding

$$\begin{aligned} \tilde{x} &= \frac{\mu AT\left[\rho z^{-1}+(1-\rho)\right]\tilde{x}_0+\tilde{\xi}}{\mu AT\left[\rho z^{-1}+(1-\rho)\right]+z-1} && (1.55)\\ \tilde{E} &= \frac{-\mu A^2T\tilde{x}_0\left[\rho z^{-1}+(1-\rho)\right]+\tilde{\xi}}{\mu AT\left[\rho z^{-1}+(1-\rho)\right]+z-1}+A\tilde{x}_0. && (1.56)\end{aligned}$$

Eqs. 1.55 and 1.56 look complicated, but that is only because of the complexity in the timing. They have the same basic structure as Eqs. 1.47 and 1.48. The dimensionless quantity μAT measures the strength of the feedback. It tells you what fraction of a displacement is counteracted by each iteration of the feedback loop. The timing parameter ρ measures a delay of a fraction of a cycle in the feedback. $\rho=0$ corresponds to the fastest feedback, $\rho=1$ to the slowest.

To simplify the notation, define $g\equiv\mu AT$. For $\rho=0$ the feedback is stable for $0<g<2$. For $\rho=1$ the feedback is stable for $0<g<1$. For $0<\rho<1$, the value of g at which the system becomes unstable lies between 1 and 2. For $g\leq 0$ or $g\geq 2$ the system is unstable and the particle is not trapped.

We now seek the power spectra of the fluctuations in $\tilde{x}$ and $\tilde{E}$. These are obtained by evaluating Eqs. 1.55-1.56 on the unit circle $z=e^{i\omega}$. The Z-transform then becomes the discrete time Fourier transform. To do this, we need the power spectrum of the Brownian noise. The Wiener-Khintchine formula relates the power spectrum to Fourier transform of the two-time autocorrelation. In discrete time,

$$|\tilde{\xi}(e^{i\omega})|^2=\sum_{m=-\infty}^{\infty}\langle\xi[n]\xi[n+m]\rangle\, e^{-i\omega m}. \qquad (1.57)$$

From Eq. 1.57, we see that the Brownian noise has power spectrum:

$$|\tilde{\xi}(e^{i\omega})|^2 = \frac{2}{3}\tau\cos(\omega) + 2D(T - \tau/3). \tag{1.58}$$

For simplicity, assume the target position is held fixed at $x_0 = 0$. Then the power spectrum of the position fluctuations of the particle becomes:

$$|\tilde{x}(e^{i\omega})|^2 = \frac{\frac{2}{3}\tau\cos(\omega) + 2D(T - \tau/3)}{|g\left(\rho e^{-i\omega} + (1-\rho)\right) + e^{i\omega} - 1|^2}. \tag{1.59}$$

The variance in position of the particle about the trap center is obtained by numerical integration of Eq. 1.59 and Parseval's identity

$$\sum_{n=-\infty}^{\infty} |x[n]|^2 = \frac{1}{2\pi}\int_0^{2\pi} |\tilde{x}(e^{i\omega})|^2 d\omega. \tag{1.60}$$

Fig. 1.8 shows the power spectrum of the fluctuations in particle position for $\rho = 1/2$ and $\tau = T$. For loop gains $g > 1$ the particle develops oscillations, manifested as a peak in the power spectrum. The variance in the position of the particle is a minimum for $g = 0.75$, which corresponds to the heavy black curve in Fig. 1.8.

1.6.3 Measurement noise

Now we consider the role of measurement noise when the feedback is on. In the presence of measurement noise, Eq. 1.52 becomes:

$$E[n] = -A(x[n] + \chi[n] - x_0[n]), \tag{1.61}$$

and Eq. 1.51 for the motion of the particle remains unchanged. If we again assume the target position is fixed at $x_0 = 0$, the power spectrum of the fluctuations in the position of the particle becomes

$$|\tilde{x}(e^{i\omega})|^2 = \frac{|\tilde{\xi}|^2 + \chi^2 g^2 |\left(\rho e^{-i\omega} + (1-\rho)\right)|^2}{|g\left(\rho e^{-i\omega} + (1-\rho)\right) + e^{i\omega} - 1|^2}, \tag{1.62}$$

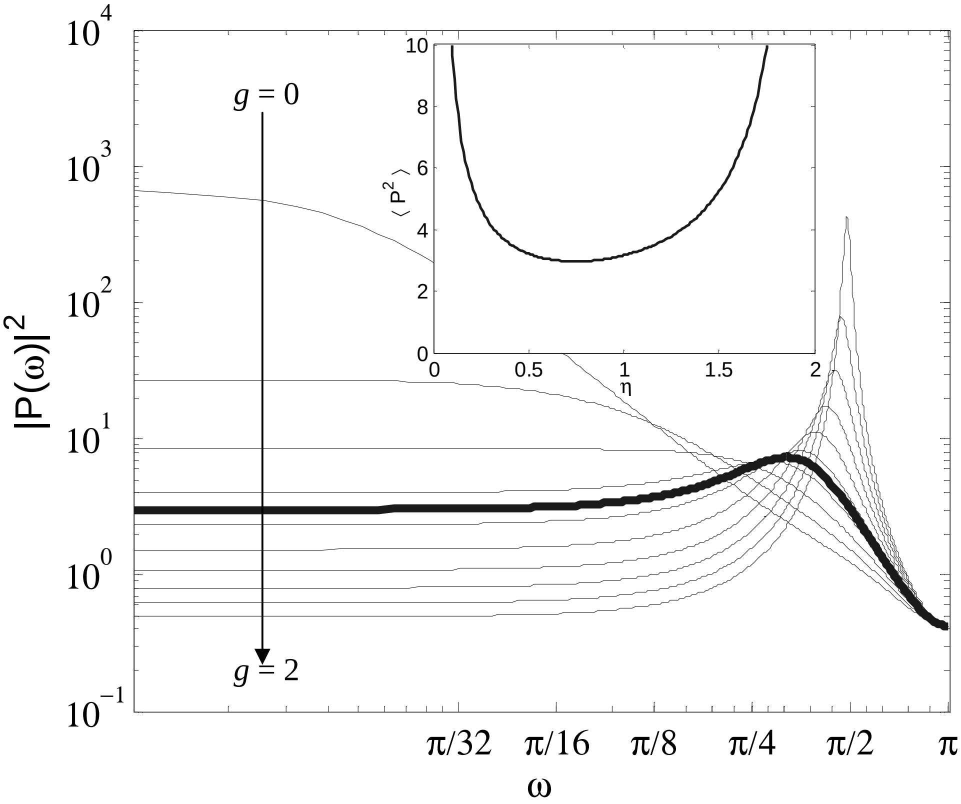

Figure 1.8: Predicted power spectrum of the fluctuations in the position of a particle held in a linear discrete time feedback loop as a function of the dimensionless loop gain, g, with the timing parameter $\rho = 1/2$. Inset: mean-square fluctuations in the position of the particle as a function of g.

where $|\tilde{\xi}|^2$ is given by Eq. 1.58 and the cross-terms containing ξ and χ vanish because we assume the Brownian fluctuations and the shot noise are uncorrelated. The quantity χ is easy to measure by, for instance, focusing on a fixed particle and recording the variance in its measured positions.

One might think that to localize a particle more accurately, one simply needs a longer integration time. The number of photons detected is proportional to the integration time, so the localization accuracy scales as $\chi^2 \propto T^{-1}$. However, any error in estimating the location of the particle is then fed back to the particle for a time T before a new measurement can correct this error. The net result is that the amplitude of the shot-noise-induced fluctuations in the position of the particle is independent of the cycle time T.

On the other hand, the particle is also diffusing and the longer one waits, the further it diffuses from the target position: $\xi^2 \propto T$. Thus even in the presence of measurement noise, one should try to make T as small as possible. When T is small (i.e. the measurement errors are large) the optimal strategy is to have a small loop gain g, so each error does not send the particle too far astray. Rather than relying on a long integration time, one simply lets the particle integrate the many small feedback kicks it receives.

Once the loop time becomes small compared to the rate at which photons are detected, the above analysis breaks down. The problem is that in the photon-counting regime, the shot-noise is no longer well approximated by a Gaussian distribution. Rather, in each feedback interval there are only two possibilities: either there was a photon or there wasn't. There is clearly no advantage to having many cycles of feedback run in between photon detection events.

1.7 Time series analysis

It should be clear by now that even a rudimentary analysis of the feedback in the ABEL trap gets very complicated. At the same time, the behavior of the feedback system itself is not very interesting—it is simply a bunch of hardware obeying some stochastic finite-difference equations. The interesting behavior is in the response of the trapped object to an electric field. This is the inverse of the problem we have been discussing. Given a set of measured positions and feedback voltages, what can we infer about the underlying transport coefficients of the trapped object?

To tackle this problem I developed a technique I call the "pseudo-free trajectory." This is a way of constructing a trajectory statistically similar to the one the particle would have followed had it not been trapped. In the time series analysis community, this trick is called the "Wold decomposition."[21]

The idea underlying the technique of pseudo-free trajectories is to extract the mobility μ from a least-squares fit of $d\mathbf{x}/dt$ vs. $\mathbf{E}$. The residuals from this fit are the Brownian displacements $\xi(t)$. Four facts complicate this task:

1. The positions and voltages are recorded at discrete times, $t_k = kT$.

2. The electric field $\mathbf{E}$ is related to the voltage $\mathbf{V}$ by a 2×2 matrix, $\mathbf{C}$, which is a function of the location of the target position for the molecule. The off-diagonal elements of $\mathbf{C}$ are typically small and arise when the target position is not exactly in the geometrical center of the trap: due to fringing fields, $\mathbf{E}$ may not be parallel to $\mathbf{V}$. While $\mathbf{C}$ may be estimated from finite-element simulations of the electric field, these simulations do not take into account imperfections in the sample cell and other experiment-specific factors. Thus it is best to treat the matrix $\mathbf{C}$ as an a priori unknown quantity.

3. The feedback voltage $\mathbf{V}[k]$ switches to $\mathbf{V}[k+1]$ at a time intermediate between t_k and t_{k+1}. Thus $\mathbf{x}[k+1] - \mathbf{x}[k]$ depends on both $\mathbf{V}[k]$ and $\mathbf{V}[k+1]$.

4. The feedback voltage typically has a small DC offset, which arises to compensate for a small fluid drift in the trapping region (under typical conditions, uncompensated drift would lead to an offset of several microns over a 20 s experiment). This drift is of no physical interest, so we subtract the time-average $\langle \mathbf{V} \rangle$ from each $\mathbf{V}[k]$ and $\langle \mathbf{x} \rangle$ from each $\mathbf{x}[k]$ prior to fitting the data. This subtraction forces our model to have zero intercept, so all pseudo-free trajectories start and end at the origin. This clearly unphysical constraint does not affect statistics related to timescales short compared to the duration of the experiment.

The above considerations lead to a multivariate linear model with 8 free parameters, $\alpha_{i,j}^{(0,1)}$:

$$\begin{pmatrix} x[k+1]-x[k] \\ y[k+1]-y[k] \end{pmatrix} = \begin{pmatrix} \alpha_{xx}^{(0)} & \alpha_{xy}^{(0)} & \alpha_{xx}^{(1)} & \alpha_{xy}^{(1)} \\ \alpha_{yx}^{(0)} & \alpha_{yy}^{(0)} & \alpha_{yx}^{(1)} & \alpha_{yy}^{(1)} \end{pmatrix} \begin{pmatrix} V_x[k] \\ V_y[k] \\ V_x[k+1] \\ V_y[k+1] \end{pmatrix} + \begin{pmatrix} \xi_x[k] \\ \xi_y[k] \end{pmatrix}. \tag{1.63}$$

For a trapped particle, one knows $\mathbf{V}[k]$ and $\mathbf{x}[k]$. One can use multivariate least squares fitting to extract the 8 unknown coefficients. The cumulative sum of the residuals, $(\xi_x[k], \xi_y[k])$, yields the pseudo-free trajectory.

1.7.1 Fluctuating transport coefficients

In the simplest model of a rigid, non-interacting particle in the ABEL trap, the parameters $\alpha_{i,j}^{(0,1)}$ are independent of time and the Brownian displacements $\xi[\mathbf{k}]$ are statistically independent and identically distributed. These conditions may be violated if the particle undergoes conformational fluctuations, ionization events, or binding and unbinding with other objects in the solution. Fluctuations in $\alpha_{i,j}^{(0,1)}$ or in the variance of ξ lead to heteroskedasticity in the measured trajectories, which can be detected in the residuals from the fit to Eq. 1.63.

Fluctuating mobility

First we consider fluctuations in the mobility. A simplified 1-D version of Eq. 1.63 is:

$$\Delta x[k] = (\alpha + \delta\alpha[k])V[k] + \xi[k], \tag{1.64}$$

where α is related to the time-average mobility, $\delta\alpha[k]$ is related to the fluctuations in mobility, and ξ is Gaussian white noise with variance σ_ξ^2. A least-squares fit of Δx against V yields α, with residuals (i.e. pseudo-free hops) $Q[k] = \delta\alpha[k]V[k] + \xi[k]$. Assuming the fluctuations $\delta\alpha$ are uncorrelated with the voltage V, the autocovariance of the residuals is

$$\begin{aligned}\left\langle Q[k]^2\right\rangle &= \left\langle V[k]^2\right\rangle \left\langle \delta\alpha[k]^2\right\rangle + \sigma_\xi^2 \\ \langle Q[k]Q[k+h]\rangle &= \langle V[k]V[k+h]\rangle \langle \delta\alpha[k]\delta\alpha[k+h]\rangle \end{aligned} \tag{1.65}$$

Thus fluctuations in the mobility show up in the autocovariance of the steps of the pseudo-free trajectory.

Fluctuating diffusion coefficient

Now we consider a fluctuating diffusion coefficient. Neglect, for simplicity, the effects of finite exposure time, measurement noise, and fluctuating mobility on a pseudo-free trajectory. Then the pseudo-free trajectory obeys

$$\Delta x[k] = \sqrt{2D[k]\delta t}N(0,1) \tag{1.66}$$

where $N(0,1)$ is Gaussian white noise with mean 0 and variance 1 and $D[k]$ is the fluctuating diffusion coefficient. Now consider the 4^{th} order correlation,

$$\begin{aligned} C^{(4)}[h] &= \operatorname{corr}\left(\Delta x[k+h]^2, \Delta x[k]^2\right) \\ &= \frac{\langle \Delta x[k+h]^2 \Delta x[k]^2\rangle - \langle \Delta x[k]^2\rangle^2}{\langle \Delta x[k]^4\rangle - \langle \Delta x[k]^2\rangle^2}. \end{aligned} \tag{1.67}$$

The normalization is chosen so that $C^{(4)}[0] = 1$. Each of the ingredients of Eq. 1.67 can be expressed in terms of correlation functions of D:

$$\begin{aligned}\left\langle \Delta x[k+h]^2 \Delta x[k]^2\right\rangle &= 4\delta t^2(1+2\delta[h]) \langle D[k+h]D[k]\rangle \\ \left\langle \Delta x[k]^2\right\rangle &= 2\delta t \langle D[k]\rangle \\ \left\langle \Delta x[k]^4\right\rangle &= 12\delta t^2 \left\langle D[k]^2\right\rangle , \end{aligned} \tag{1.68}$$

where we made use of the fact that $\langle N(0,1)^2 \rangle = 1$ and $\langle N(0,1)^4 \rangle = 3$. Making the above substitutions into Eq. 1.67 yields

$$C^{(4)}[h] = \frac{(1 + 2\delta[h]) \langle D[k+h] D[k] \rangle - \langle D[k] \rangle^2}{3 \langle D[k]^2 \rangle - \langle D[k] \rangle^2}. \tag{1.69}$$

Thus the 4th order correlation $C^{(4)}[h]$ is sensitive to fluctuations in the diffusion coefficient of the particle which might arise, for instance, from conformational fluctuations that change its hydrodynamic radius.

Chapter 2

Video Trapping

In this chapter I describe three incarnations of the ABEL trap based around video imaging. The cost of successive implementations increased by a factor of about 100, and the performance by a factor of about 10. Over time the design of the sample cell also evolved. While any of the sample cells could be used with any of the tracking and feedback schemes, for simplicity I will describe each sample cell as though it were affiliated with a particular embodiment of the apparatus.

2.1 Generation 1

2.1.1 Gold electrodes

The first generation of the ABEL trap used microfabricated gold electrodes on a glass coverslip. The pattern of electrodes and the fabrication procedure are illustrated in Fig. 2.1.

The ABEL trap does not provide confinement in the z-direction (although a variant with eight electrodes placed at the corners of a cube is conceivable). To provide z-confinement we formed a thin disc-shaped fluid volume in the z-direction using a PDMS stamp. The PDMS stamp consisted of a checkerboard array of square posts 1.5 μm high and 95 μm wide, separated by 105 μm. In spite of the low aspect ratio, the recessed regions of the stamp did not collapse onto the coverslip, provided that

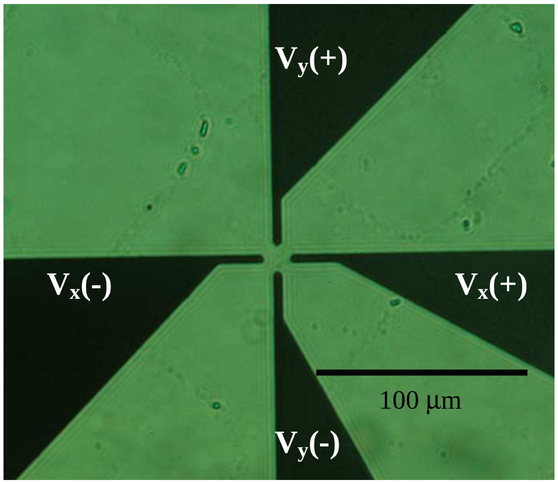

Figure 2.1: Gold electrodes (black) were fabricated to reach to the corners of a diamond-shaped trapping region. Electrodes were fabricated on 22 mm square low-fluorescence glass coverslips (Fisher) using standard contact photolithography and a bilayer liftoff process. The electrodes consisted of a 40 nm chromium adhesion layer capped by 200 nm of gold. Four-electrode arrays were formed with gaps between opposing electrodes of 3, 5, 10, and 15 μm. The 10 and 15 μm arrays proved the most useful.

the assembly was handled gently. An annular "pressure relief" trench in the PDMS, ~ 1 mm inner radius, ~ 2 mm outer radius, and ~ 0.5 mm deep, surrounded the array of posts. Fluid inlet and outlet holes were punched through the top of the stamp into the pressure relief trench. This trench was crucial to the success of the experiment: without it, minute pressure differences between the inlet and outlet ports led to large flow velocities in the thin layer of solution above the electrodes. The procedure for fabricating the PDMS stamp is shown in Fig. 2.2.

In a typical experiment, the coverslip and PDMS stamp were cleaned by sonication in a solution of deionized water and Alconox detergent. After sonication, both surfaces were hydrophobic, so water would not fill the thin channels. The coverslip was rendered hydrophilic by exposing it to a radiofrequency plasma of room air for 1 minute. This treatment was sufficient to cause water to fill the channels, without necessitating any special surface treatment of the PDMS. If the PDMS was subjected to the same plasma treatment, it became hydrophilic too, but also on contact it bonded

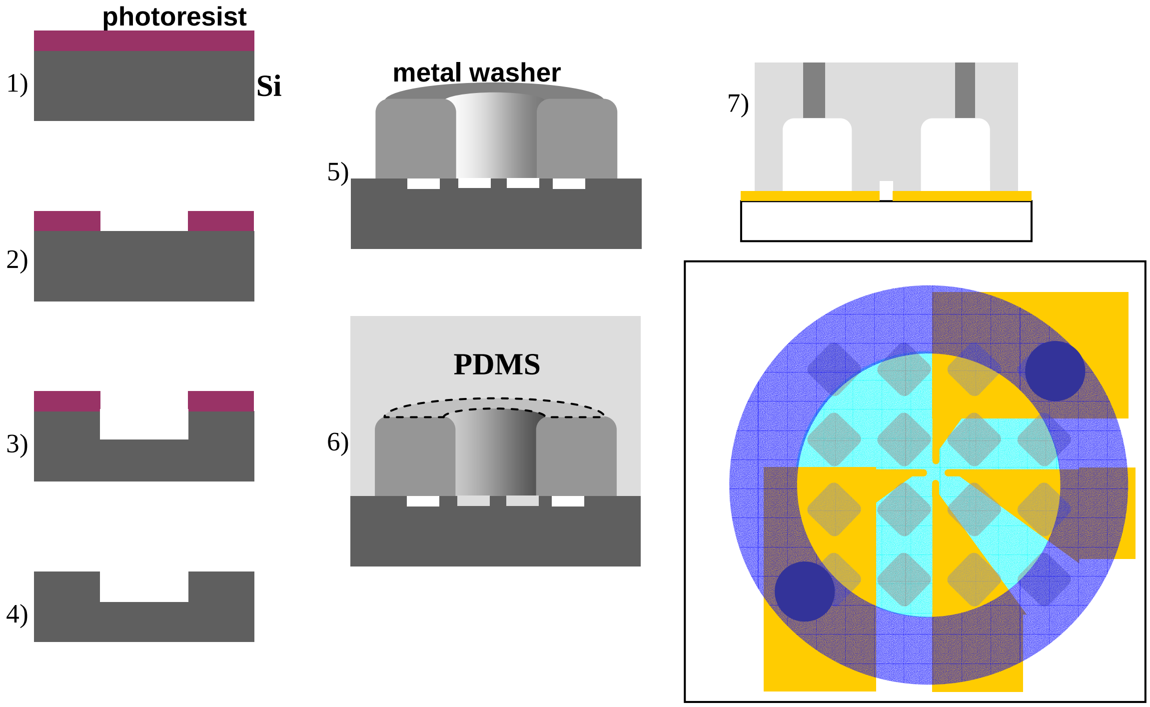

Figure 2.2: Procedure for fabricating a PDMS stamp to confine particles in the z-direction. 1) A silanized silicon wafer was coated with 1.6 μm of SPR 3612 photoresist. 2) The checkerboard pattern was formed by using a high-resolution black and white printer to print a grey shade on a mylar transparency. The transparency was used as an exposure mask and the pattern was transferred to the photoresist. 3) An SF_6 reactive ion etch was performed to transfer the pattern 1.5 μm into the silicon. 4) The photoresist was stripped from the wafer. 5) A metal washer was glued to the wafer to form the mold for a pressure relief trench. 6) To prevent adhesion of the PDMS, the master was put in a desiccator in vacuum with a drop of trichloro(1H,1H,2H,2H perfluorooctyl)silane (Aldrich) for 1 hr. prior to applying PDMS. 7) The cured PDMS was peeled off the mold, access holes were punched through its top, and it was bonded to the coverslip. The bottom right panel shows a top view of the assembled device.

irreversibly to the coverslip. We typically did not plasma-treat the PDMS so that the PDMS and coverslip could be separated and cleaned between experiments. The PDMS stamp and coverslip were assembled by hand under a dissecting microscope.

The sample cell was mounted in an inverted optical microscope equiped with a 100x, NA 1.3 oil immersion objective (Nikon S Fluor) and a 4x magnifier. The trapping region was illuminated with several mW of laser light. Our setup can be switched between illumination at 633 nm, 532 nm, 514 nm, or 488 nm. The sample cell was filled with a solution of the particles to be trapped. The inlet and outlet holes were then capped with a slab of PDMS. Once capped, the cell could be used for days without need for disassembly. Fluorescently labeled polystyrene nanospheres (FluoSpheres, Molecular Probes) dissolved in deionized water were excited with a 1 mW 633 nm HeNe laser, and fluorescence emission was detected with a Genwac 902H Si CCD camera operating at a 30 Hz frame rate.

2.1.2 Magic Wand feedback

In the initial demonstration of the ABEL trap, images from the CCD camera were displayed on a TV screen. The feedback was performed using the "magic wand" configuration of photoresistors shown in Fig. 2.3. The four photoresistors were mounted in a diamond configuration inside a plastic funnel. The funnel was placed over the image of one particle on the TV screen. If the image of the particle was located symmetrically between the four photoresistors, then both voltage dividers were balanced and the cell received no feedback voltage. If the particle moved off-center, then one photoresistor would get more light than the others, leading to an imbalance in the voltage divider circuit. The simple circuit shown in Fig. 2.3b generated the bipolar voltages that were applied to the electrodes. By dragging the photoresistors around on the TV monitor, one could move a trapped particle inside the ABEL trap on a scale some 10,000 times smaller. This very simple proof-of-principle device could trap 1 micron fluorescent microspheres.

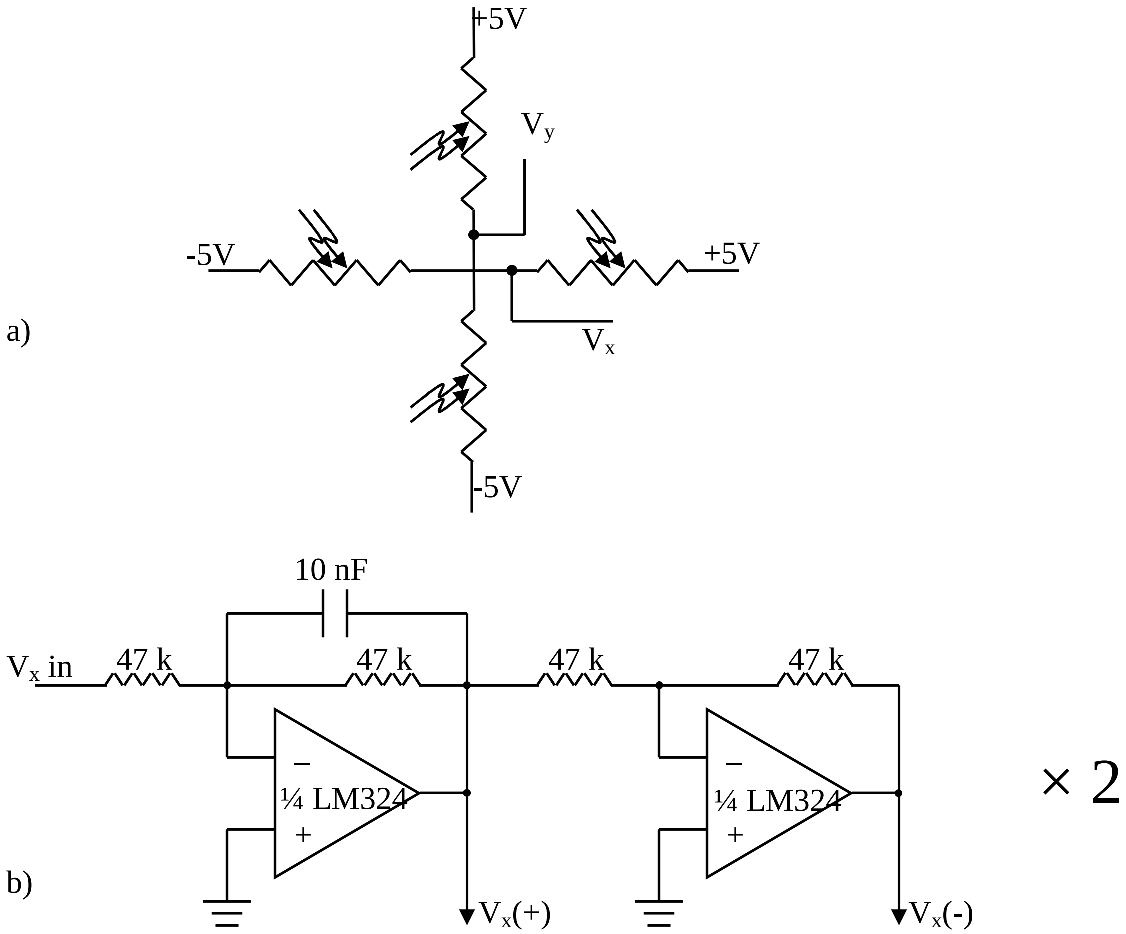

Figure 2.3: Magic Wand feedback circuit. a) Configuration of photoresistors to detect the position of a bead on a video screen. b) Op-amp circuit to generate bipolar driving voltages for the x electrodes. An identical copy of this circuit was used for the y electrodes. All implementations of the ABEL trap used this circuit (or a functional equivalent) to turn unipolar feedback signals into bipolar voltages to apply to the electrodes.

2.2 Generation 2

The proof-of-principle ABEL trap described above had several serious drawbacks. The gold electrodes were subject to corrosion, so they could only be used for a small number of experiments. Furthermore, electrochemistry on the electrodes changed the chemical composition of the solution, leading to a gradual fouling of the solution. Finally, the coupling between applied voltage and particle velocity was both time-dependent and nonlinear. The time-dependence arose because ions in the solution migrated to the electrode surfaces, gradually polarizing the solution and shielding electric fields from the electrodes. This ionic screening had a time constant of a few hundred ms. The nonlinearity arose because of Faradaic processes, which set in at potentials as low as a few hundred mV. The Faradaic current depended on concentration of reactants and products, which in turn were affected by diffusion and ionic transport, which depended on the history of applied voltages. All of these complications made it difficult to design an effective feedback algorithm.

The magic wand clearly had problems too. The 30 Hz frame-rate of the video monitor was too slow to trap objects smaller than a few hundred nm. Also, the feedback parameters were ill-controlled, depending on the contrast in the monitor, the ambient light intensity, and the response of the photoresistors. Finally, this system lacked any mechanism for recording data.

The second generation of the ABEL trap[33] resolved many of these difficulties.

2.2.1 PDMS cell

The problems with using gold-on-glass microelectrodes were solved by building a purely microfluidic sample cell with no microfabricated electrodes. The cell was made of poly(dimethyl siloxane) (PDMS). The cell was designed so that the electrodes and all of their electrochemical byproducts were kept far from the trapping region, while almost the entire electric field from the electrodes was focused to within the 20 μm trapping region. Thus, unlike traditional capillary electrophoresis setups, the ABEL trap operates at relatively low voltage.

The sample cell contained channels of two different depths: a shallow (880 nm)

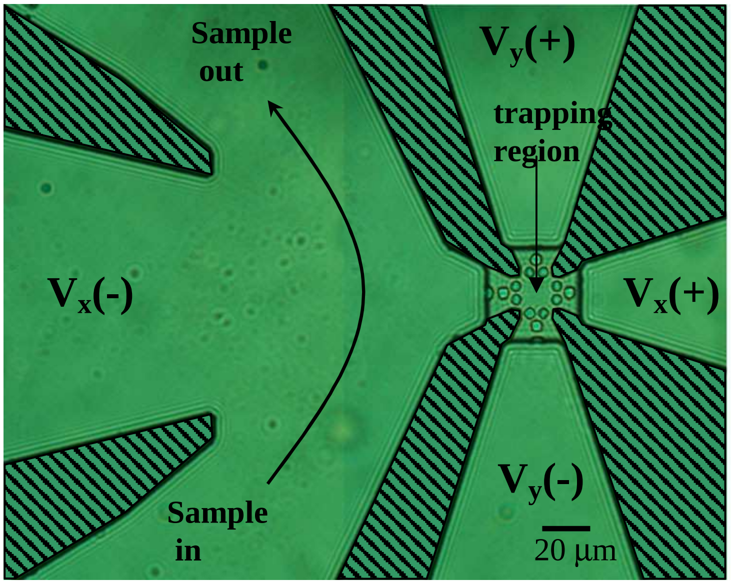

Figure 2.4: Trapping region of the ABEL trap, formed from an oxidized PDMS stamp and a glass coverslip. The trapping region is $\sim$ 20 μm across and 880 nm deep. This depth allows free diffusion of submicron particles, while still confining the particles to the focal plane of the microscope. The small circles surrounding the trapping region are support posts to keep the PDMS from collapsing onto the glass coverslip. The channels extending to the edges of the image are $\sim$ 20 μm deep and extend $\sim$ 7 mm away from the trapping region, where they are connected to macroscopic platinum electrodes. The channel on the left splits into three to allow for easy and rapid sample delivery. Regions of PDMS in contact with the glass have been crosshatched for clarity.

channel formed the trapping region and deep (20 μm) channels connected the trapping region to macroscopic electrodes. It was necessary to use a thin channel in the trapping region to confine trapped objects to the focal plane of the microscope. It was also necessary to use thick channels to connect the trapping region to the macroscopic electrodes to avoid resistive losses in these channels and to allow the channels to fill easily. The feedback potentials were supplied via macroscopic platinum electrodes inserted in the distal ends of the large channels.

Sample cells were fabricated in the Stanford Nanofabrication Facility (SNF) using the procedure illustrated in Fig. 2.5. A template for the PDMS cell was formed in two stages of photolitography on a 4” Si wafer. Initially we used a conventional chrome-on-quartz mask to pattern the Si master. We found, however, that equally good results were obtained using high-resolution transparency masks, at a significant saving of cost and effort. Once a master was made with 40 copies of the pattern, it could be used repeatedly to fabricate batches of 40 sample cells. Thus we were able to use the sample cells disposably, avoiding the risk of cross-contamination between experiments.

In a typical experiment, the PDMS stamp and a glass coverslip were cleaned in hot Alconox detergent. Then both were exposed to a plasma of low-pressure room air for 1 minute and then irreversibly bonded to each other. The plasma treatment made the surfaces hydrophilic and negatively charged, which led to strong electroosmotic flow. The cell was filled by injecting sample into the fluidic fluidic channels and then relying on capillary action to fill the channels.

A major challenge was to eliminate pressure-driven flows in the trapping region. The cross-sectional area of the trapping region (20 μm$\times$ 880 nm) is roughly 800 times smaller than that of the microfluidic channels connecting to the electrodes (700 μm$\times$ 20 μm). Thus even slight flows in the channels led to very large flow velocities in the trapping region. We balanced the pressure in the channels by connecting the entrances to each channel to the same fluid reservoir, thereby guaranteeing that they were at the same pressure.

2.2.2 Computerized feedback

Images from the Genwac CCD camera were captured using a National Instruments PCI-1407 frame grabber card on a 2.8 GHz Pentium 4 computer. The image-processing was performed in real-time using software I wrote in Visual Basic. During each frame, the Genwac first reads the even-numbered rows of pixels, and then the odd-numbered rows. By using separately the two interleaved fields that constitute one frame, I was able to increase the feedback bandwidth from 30 Hz to 60 Hz. The coordinates of the particle of interest were extracted using the IMAQ Vision library (National Instruments). The offset between the desired location of a particle and its actual location was turned into a feedback voltage, which was applied to the electrodes.

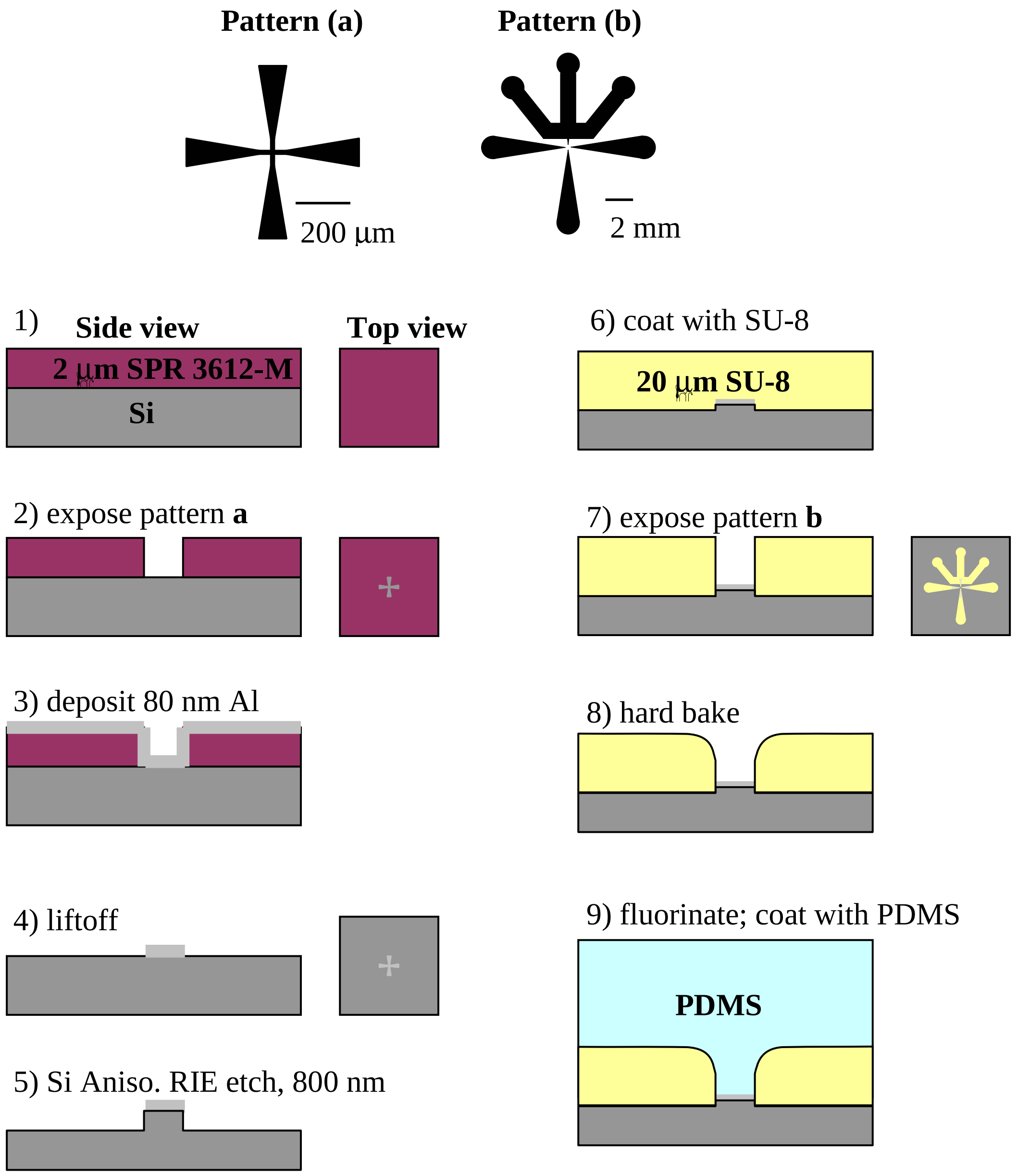

Figure 2.5: Process for making PDMS microfluidic cell. Top: Mask patterns were printed on a transparency. Each mask contains ∼ 40 copies of the pattern. Bottom: Processing steps. The central trapping region was patterned on a 4” wafer. The Al overcoat on the mesas made the mesas easy to locate for alignment with the second layer of lithography. The hard-bake of the SU-8 (150 C, 2 hrs.), strengthened the film and rounded the corners creating a draft angle for easy removal of the PDMS. To prevent adhesion of the PDMS, the master was put in a desiccator in vacuum with a drop of trichloro(1H,1H,2H,2H perfluorooctyl)silane (Aldrich) for 1 hr. prior to applying PDMS.

Fig. 2.6 shows the displacement trajectories of a free and a trapped 200 nm diameter particle. The histogram of displacements is well fit by a Gaussian. The width of this Gaussian is related to the effective spring constant of the trap through the relation

$$k = k_B T/\sigma^2, \tag{2.1}$$

where σ is the width of the distribution of particle displacements. For the 200 nm particle $\sigma = 0.45$ μm, implying a spring constant of $k = 20$ nN/m. Fig. 2.7 shows a histogram of the displacements of a 20 nm particle with a fixed target position. The width of the histogram is $\sigma = 1.58$ μm from which we extract a spring constant of $k = 1.7$ nN/m. The relative widths of the distributions for 200 nm particles and 20 nm particles are consistent with the trapping strength being limited by the feedback latency. The 20 nm particle has a diffusion coefficient 10 times larger than the 200 nm particle, so in one feedback iteration the 20 nm particle should diffuse farther by a factor of $\sim \sqrt{10}$.

The target position of the particle could be moved either by clicking and dragging the image of the particle on the computer screen, or by reading values from a file. Fig. 2.8 shows the trajectory of a 200 nm particle automatically manipulated to trace out a smiley face.

2.3 Generation 3

The Genwac-based trapping system could easily trap particles down to 100 nm in diameter, and could marginally trap particles as small as 20 nm in diameter, yet still the system suffered from several drawbacks.

The sample cell formed from a PDMS stamp and a glass coverslip had the advantage that the PDMS stamps were easy to make in large numbers and could be disposed after use. For certain applications a PDMS-based trap may be sufficient. We switched to an all-glass trap for four reasons:

1. *Better control of surface chemistry.* In the PDMS-based trap, one surface in the trapping region was PDMS while the other surface was glass. In general

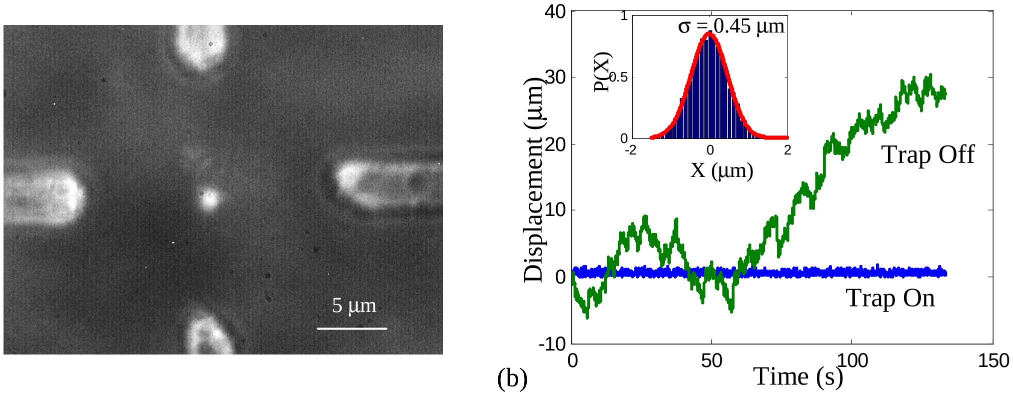

(a) (b)

Figure 2.6: Trapping of a 200 nm particle. a) Average of 30 video frames showing a single trapped particle. A cell with microfabricated electrodes was used to generate this picture. The trapping electrodes are visible protruding from the edges of the image. b) Comparison of trajectories of a 200 nm diameter particle with the trap on and with the trap off. Inset: histogram of displacements from equilibrium.

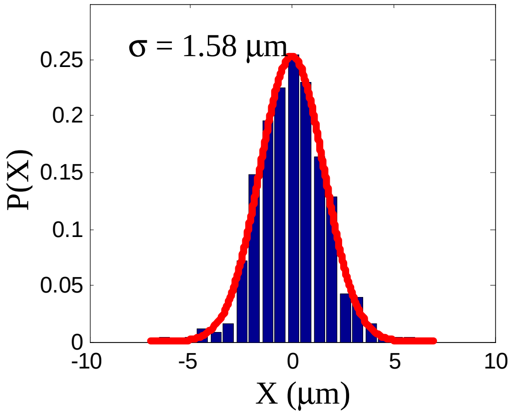

Figure 2.7: Histogram of displacements of a 20 nm fluorescent particle trapped using images from the Genwac.

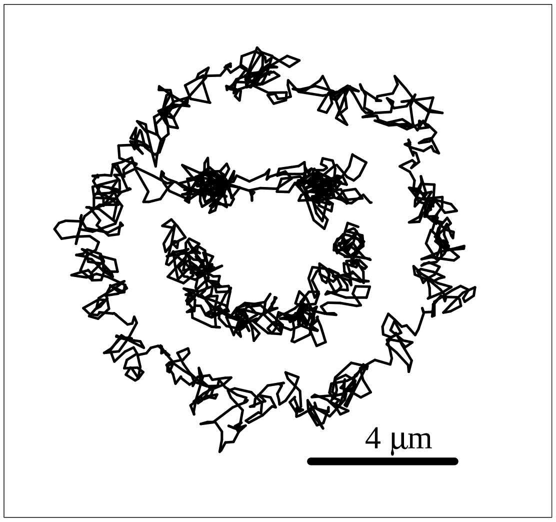

Figure 2.8: Trajectory of a 200 nm particle over the course of 1 minute, as it was manipulated to draw out a smiley face. The trajectory was specified by a file containing 1800 target positions, updated at 30 Hz. (2 of the 1800 data points—those joining the eyes and mouth—are not plotted.)

these two surfaces had different electroosmotic velocities. Thus the velocity of a particle in the trap depended on its (uncontrolled) z-displacement. The PDMS and glass also had different affinities for different objects. It was difficult to find a set of solution conditions that were optimal with respect to both surfaces. Furthermore, the surface chemistry of PDMS is poorly defined. PDMS strongly adsorbs species from air and from solution, so its properties change over time.

2. *Ability to remove oxygen from the solution.* Many fluorophores are quenched by oxygen dissolved in the solution. In most single-molecule experiments, an enzymatic oxygen scavenger system is added, which may extend the lifetime-to-photobleaching of a single molecule by a factor of 10 - 100. PDMS is porous to oxygen, and due to the high surface-to-volume ratio in the trapping region, all attempts at removing oxygen from the solution were unsuccessful. With a glass cell it is much easier to remove the oxygen from the solution. This factor was crucial to trapping single biomolecules for long times.

3. *Control of gap thickness.* For studies of surface interactions and the effect of

electroosmotic flow it is helpful to be able to control the thickness of the trapping region. Below we describe a method for adjusting the thickness of the gap with the glass cells.

4. *Lower background fluorescence.* PDMS itself has a low level of background fluorescence. Over time, however, it soaks up fluorescent impurities from the environment and the background fluorescence increases. In contrast, glass cells show very low fluorescence and do not absorb impurities.

2.3.1 Glass cell

The design for the glass cell was in the same spirit as the design for the PDMS cell, with minor modifications to improve inconvenient aspects of the PDMS cell. Fig. 2.9b shows the design. The fabrication procedure is given in Appendix 2.8.

It is advantageous be able to control the depth of the trapping region. Typically one wants the depth to be small enough to confine the object under study to the focal plane of the microscope, but large enough so that the walls of the trap do not interfere with the process being studied. In some cases, such as in studies of long DNA molecules, one may wish to study the effects of confinement on the molecular conformation and dynamics.

The microfluidic cell and holder presented here give the experimenter control over the depth of the trapping region. Fig. 2.9a shows the aluminum slide holder that allowed me to adjust the depth of the trapping region. As-assembled, the trapping region has a depth of ~ 10 μm—too large to allow trapping. A 0-80 setscrew for adjusting the gap was mounted in a sheet of acrylic above the cell. The setscrew pressed on a piece of PDMS, which in turn pressed on the patterned glass, causing the slide to bow downwards, narrowing the gap. Due to its high compliance, the PDMS translated a relatively large displacement at its top surface into a small force applied to the glass. In this way we were able to achieve sub-100 nm control over the thickness of the gap. The gap was measured interferometrically and adjusted to ~ 500 nm. In between experiments the cell could be disassembled and both pieces of glass thoroughly cleaned. The patterned piece of glass that formed the top of the cell was used for hundreds of experiments with no detectable change in its performance.

Simulating electric fields in the trap

To calculate the mobility of trapped objects in real units (m^2/Vs) it was necessary to know the conversion between voltage applied to the trap and electric field experienced by the trapped particle. A 2-dimensional finite-element simulation of the electric field was performed in Matlab. Due to their great depth (and hence high conductivity) relative to the trapping region, the channels leading to the trapping region were assumed to form equipotential surfaces. A micrograph of the trapping region was digitized, rendered in binary, and then used to set boundary conditions for the simulation (Fig. 2.10).

The simulations show that in the center of the trapping region the electric field is quite uniform. The field-of-view of the microscope is typically 10 μm x 10 μm, over which the electric field strength varies by only 0.6%. In the center of the trap, the field strength is roughly 6 (mV/μm)/V. Thermal fluctuations will drive an object with a charge of $1e$ "uphill" in the trap to a characteristic potential of $k_BT/e = 25$ mV. To confine such a particle to a region 1 μm on a side, the field must be ~ 25 mV/μm, which corresponds to an applied voltage of only slightly greater than 4 V.

2.3.2 Control Software

Fluorescence images were captured on a high-sensitivity CCD camera (Cascade 512B, Roper Scientific) at frame-rates of up to 300 Hz. The computer controlling the ABEL trap must perform the following tasks:

1. Acquire images as they stream in from the camera;
2. Process the images in real-time to extract the x,y-coordinates of a single nanoparticle;
3. Calculate feedback voltages and send them to the D/A converter;
4. Display on the monitor an image of the trapping region, highlighting the trapped particle;

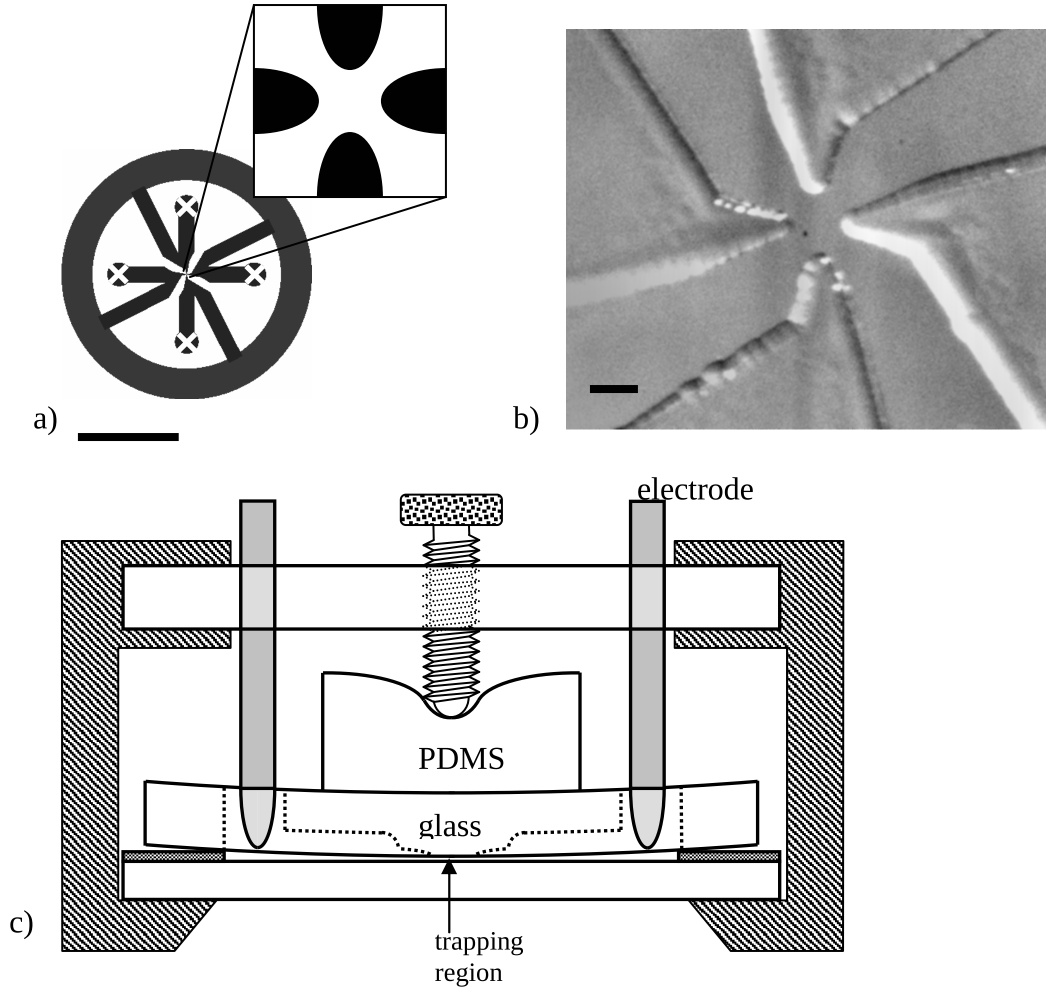

Figure 2.9: Glass microfluidic cell for the ABEL trap. a) Top view of the microfluidic channels. Recessed areas are in black. Electrode ports are indicated by white x's. The large circular channel equalizes the hydrostatic pressure in the four arms of the device and allows for easy filling of the channels. The trapping region is in the center. Scale bar, 1 cm. Inset: close-up of the trapping region. The gap between opposing channels is $\sim$130 μm. b) Photograph of the trapping region, showing the patterned glass cell. Molecules are trapped in the center. Four channels $\sim$ 17 μm deep (the regions shaped like a bird's beak) extend to the edge of the image and terminate in macroscopic electrodes. Scale bar, 100 μm. c) Cross-sectional view including the cell holder. The top of the cell is a patterned glass wafer and the bottom is a standard glass coverslip. A 10 μm annular spacer separates the top and bottom. A setscrew pushes down on a piece of PDMS, which in turn presses on the top piece of glass. The glass bows downward slightly, allowing the depth of the trapping region to be adjusted between 0-1 μm. The top and bottom of the cell can be separated for cleaning or surface treatments.

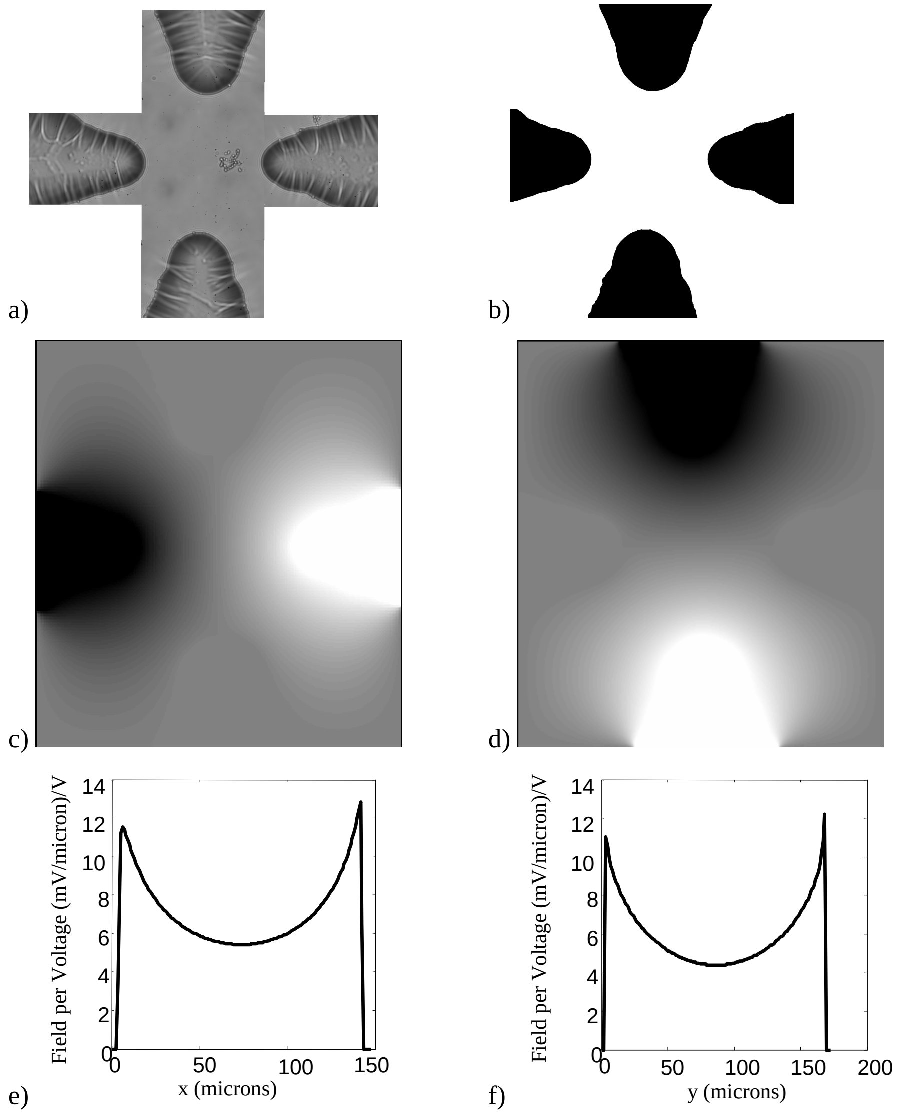

Figure 2.10: Numerical simulation of the electric field in the trapping region. a) composite micrograph of trapping region; b) binary version of image; c, d) potential profiles for vertical and horizontal potentials, respectively; e, f) vertical and horizontal electric field profiles through the center of the trap.

5. Accept inputs from the user, such as mouse clicks indicating to move the target location or to trap a different particle.

6. Record and save video images, the trajectory of the trapped particle, and the applied feedback voltage.

The first three of these tasks must be performed in less than 3.4 ms, which is a typical interval between video frames from the camera. This requirement places stringent demands on the software and computer. Tasks 4–6 can take longer to execute, but they cannot delay the execution of the first three tasks by more than 3.4 ms.

The control software is run on a personal computer (Advantage PC, 2.8 GHz Pentium 4, Windows 2000). The software is written in Visual Basic 5.0, with the IMAQ Vision and ComponentWorks libraries from National Instruments and the PVCAM low-level camera-control library from Roper Scientific. Visual Basic is not a compiled language, so these libraries are key to achieving the requisite speed of the feedback loop.

The most critical design feature in the ABEL trap is achieving a short feedback latency. Much of the latency in our system comes from the camera. The Cascade 512B camera is a frame-transfer CCD imager with 512 x 512 pixels, on-chip gain, and a 10 MHz pixel readout clock. The frame-transfer process imposes an unavoidable delay of 2 ms on each frame. Reading out the image from the CCD causes a further delay. With a 16 x 16 Region of Interest (ROI), the total interframe interval (frame transfer plus readout) is 3.1 ms, and with a 32 x 32 ROI the interframe interval is 4.5 ms. The time for the computer to process an image depends on the image-size, and typically requires $\sim$ 0.5 video frames. Thus the total latency in the feedback loop is $\sim$ 1.5 video frames, or 4.6 ms with a 16 x 16 ROI and 6.8 ms with a 32 x 32 ROI. This feedback latency determines the smallest size of particle that the ABEL trap can trap.

We have written auxiliary software to quantify the feedback latency of the ABEL trap for any set of software parameters. An LED under computer control is pointed at the camera. The computer briefly flashes the LED, and then records how long it takes for the camera and image-processing software to register the flash. In this way we have been able to optimize the entire feedback system for maximum speed.

To maximize the speed of the image processing, a small sub-image (typically 15 x 15 pixels), which we term the "fovea," is extracted from the raw image from the camera. This fovea is chosen to be small enough to contain on average only one particle, but large enough so that if the particle is in the center of the fovea during one frame, the particle is unlikely to have left the fovea entirely in the subsequent frame. In the first step of image processing, a background image is subtracted from the fovea. The background image is constructed by averaging many (typically 10 to 1000) video frames. The background subtraction is useful for removing signal from scattered laser light and from particles stuck to the surface. An optional flat-field correction then scales the intensity values in the fovea based on the spatial distribution of laser intensity. This is useful if the laser intensity is inhomogeneous over the field of view. The fovea is then convolved with a Gaussian filter (typically with a 3 x 3 or 5 x 5 kernel). A diffraction-limited spot covers several pixels on the camera, so this process preserves real features while diminishing pixel noise. A threshold is applied to remove residual background, and then the center of mass is calculated for the remaining pixels. The fovea for the next frame is centered on the center of mass calculated for the preceding frame. This procedure allows the software to track a single particle over many frames, even if there are multiple other particles in the large image. However, if two particles enter the fovea simultaneously, then only their mutual center of mass is tracked until one of the particles exits the fovea. The IMAQ Vision library from National Instruments performs all of the above operations in $\sim$ 2.5 ms for a 32 x 32 ROI.

Our software allows the user to superimpose on the feedback field an arbitrary AC or DC field. Fields with frequencies higher than the feedback bandwidth can be used to orient anisotropic particles, or to measure their mobility as a function of frequency. The ABEL trap allows one to measure time- and frequency-dependent mobilities of single particles—something which cannot be done in any other way. Time-resolved single-particle mobility measurements provide information on charge and conformational fluctuations. A DC field causes particles to sweep through the field of view. This can be useful if one is searching for a specific type of particle, or if one is working with a very dilute solution in which there are not typically any particles in the field of view.

Once a particle is trapped, there are several ways to control its position. The software accepts mouse input, so a user can simply click on an image of a trapped particle and drag the particle around on the screen. The computer adjusts the coordinates of the target position in response to movements of the mouse. Alternatively, the user may specify a file with a list of target locations. Once a particle is trapped, the computer runs through this list and applies a new target location with each frame. We have used this procedure to make particles trace out complex paths.

2.4 Characterization of the ABEL trap

In the simplest incarnation of the ABEL trap, the feedback voltage provides a linear restoring force: $\mathbf{V} = -A(\mathbf{r} - \mathbf{r_0})$, where $\mathbf{r_0}$ is a target position. When the gain A is properly adjusted, the electrophoretic drift between frames n and $n+1$ exactly cancels the Brownian displacement between frames $n-1$ and n, so the particle is trapped at position $\mathbf{r_0}$. Changing $\mathbf{r_0}$ in software causes the particle to move in 2-dimensional space.

Fig. 2.11 shows the trajectory of a trapped 50 nm nanosphere subject to linear feedback. The position fluctuations are Gaussian with r.m.s. amplitudes of $\sigma_x = 550$ nm and $\sigma_y = 520$ nm. The effective spring constants are related to the amplitude of the thermal fluctuations via Eq. 2.1, so $k_x = 1.3 \times 10^{-8}$ N/m and $k_y = 1.5 \times 10^{-8}$ N/m. Individual nanospheres were held in the trap for periods of up to several minutes.

Pseudo-free trajectories for trapped nanospheres were extracted following the procedure in section 1.7. The eight coefficients of the mobility matrices are obtained through a multidimensional linear regression of the measured displacements against the applied voltages. The residuals from this fit are the displacements due purely to the Langevin term, $\xi_i(n)$. Summing these residual displacements leads to a “pseudo-free” trajectory, as illustrated in Fig. 2.11. This kind of reconstruction can only be performed with an active trap because it requires knowledge of the force applied by the trap at all times.

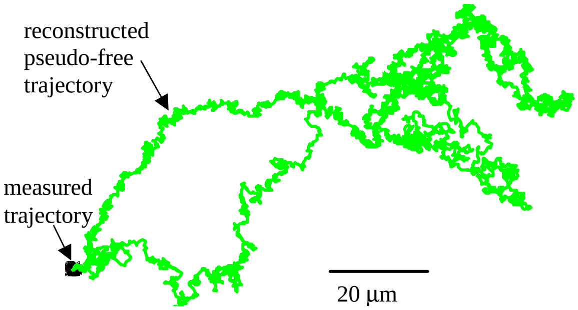

Figure 2.11: Trajectory of a trapped 50 nm particle (black), measured over 10,000 time steps (45 seconds). A "pseudo-free" trajectory (green) is obtained by subtracting from the measured trajectory the motion due to the applied electric field. The pseudo-free trajectory is constrained to start and end at the origin.

Gosse and Croquette modelled a Brownian particle subject to linear, discrete-time feedback using the Langevin equation:[48]

$$r_i(n+1) = r_i(n) - \alpha r_i(n-\Delta) + \xi_i(n), \tag{2.2}$$

where α is a dimensionless measure of the feedback gain and Δ is the feedback delay, measured in video frames. For the present apparatus Δ is between 1 and 2. This equation is a special case of the more general feedback equation 1.59 that takes into account the finite exposure time of the camera. They showed that a particle subject to Eq. 2.2 undergoes thermal fluctuations with a power spectrum,

$$|r_i(f)|^2 = \frac{4D\,\delta t^2}{|e^{2\pi i f} - 1 + \alpha e^{-2\pi i f\Delta}|^2}. \tag{2.3}$$

Eq. 2.3 predicts that when α surpasses a threshold (determined by Δ) the power spectrum develops a peak and the particle starts to oscillate. The spectra of Eq. 2.3 are in quantitative agreement with experiment, both for values of α above and below the oscillation threshold. Fig. 2.12 shows the power spectra of the trapped and pseudo-free trajectories of Fig. 2.11. The trapped spectrum is well described by Eq. 2.3, with α just at the oscillation threshold, while the pseudo-free spectrum is fit by $1/f^2$ noise, as expected for a free random walk.

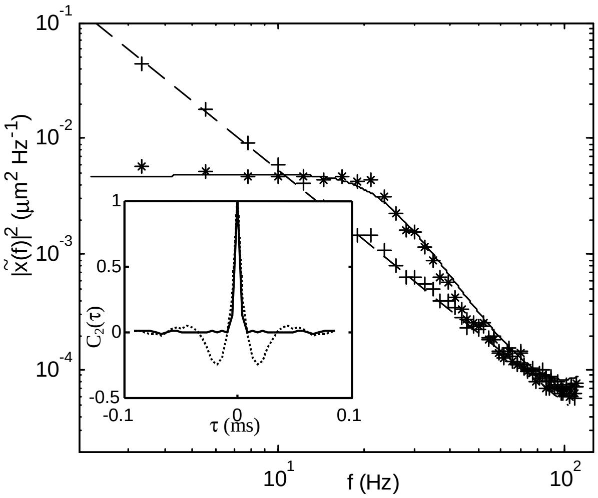

Figure 2.12: Power spectra of the x-fluctuations of a trapped 20 nm particle (*) and of the corresponding pseudo-free trajectory (+). The trapped spectrum is fit by Eq. 2.3, with $\delta t = 4.5$ ms, $\alpha = 0.3$ and $\Delta = 1.3$. The value of D is fixed at the value extracted from the pseudo-free power spectrum (8.7 μm^{2}s^{-1}). The pseudo-free spectrum is fit by $|x(f)|^2 = D/(\pi f)^2$. Inset: normalized two-point correlation functions of the displacements between successive frames along the x-axis, $C_2(\tau) \propto \langle \delta x(t)\, \delta x(t+\tau) \rangle$. The correlation function of the measured trajectory (- -) shows ringing due to the feedback delay, while that of the pseudo-free trajectory (–) shows δ-correlated steps.

Using the diffusion coefficient extracted from the pseudo-free trajectory ($D =$ 8.7 μm^{2}s^{-1}), the Stokes-Einstein relation implies a particle diameter of 50 nm. Nanoparticles in the stock solution have a nominal diameter of 24 ± 4 nm, corresponding to an expected $D = 18 \pm 3$ μm^{2}s^{-1}. To resolve this discrepancy between the measured and expected values of D, the measurement of Fig. 2.11 was repeated for $n = 19$ more nanoparticles from the same solution (trapped for 1000 video frames each). The average measured diffusion coefficient was $D = 16 \pm 6$ μm^{2}s^{-1} (min 5.7 μm^{2}s^{-1}, max 31 μm^{2}s^{-1}), in reasonable agreement with the expected value. For the nanoparticle with $D = 31$ μm^{2}s^{-1} the Stokes-Einstein relation yields a diameter of 14 nm.

2.5 Arbitrary Force Fields

One of the advantages of performing feedback in software is that the feedback voltage can be an arbitrary function of the present (or past) position of the particle. The simplest incarnation of the ABEL trap applies a voltage linear in the offset between the particle and a target location. This is equivalent to trapping the particle in a harmonic trap. However, we have also experimented with applying voltages that correspond to power-law, double-well, and lattice potentials. Furthermore, the force field need not be the gradient of a potential: we have experimented with force fields with non-zero curl, which make the particle travel in circles. The force field may also depend on the position of the particle at times other than the most recent frame. For instance, a velocity may be calculated for the particle by calculating the displacement over the two most recent frames. Adding a force proportional to the velocity is equivalent to giving the particle momentum. Depending on the direction of this force, the apparent mass of the particle may be increased or decreased, or an effective magnetic field may be applied. Here I describe the dynamics of 200 nm particles in power-law potentials and double-well potentials. The nanoparticles used in this study are fluorescent polystyrene (Molecular Probes, Eugene, OR), diluted in distilled water, and used under ambient conditions.

With a trivial modification of the software, it is possible to apply an arbitrary $\mathbf{V}(\mathbf{r})$ to a single particle. Consider a feedback voltage of the form

$$\mathbf{V} = -A \left(\frac{r}{r_0} \right)^{\beta} \hat{r}. \tag{2.4}$$

The particle experiences an effective potential proportional to $r^{\beta+1}$, or to $\ln r$ for $\beta = -1$. Thus the potential is harmonic for $\beta = 1$; conical for $\beta = 0$; logarithmic for $\beta = -1$; and Coulombic for $\beta = -2$. When $-1 < \beta \leq 0$, the potential has a cusp at $r = 0$. When $\beta \leq -1$, the potential diverges at $r = 0$, and when $\beta < -1$, the potential is bounded as $r \to \infty$. At any finite temperature, a particle will only be stably trapped for $\beta > -1$.

A single 200 nm particle was subjected to 15 different values of β between -0.8

and 4. For each value of β, 10,000 frames of data (roughly 45 seconds) were acquired. For $-1 < \beta < -0.8$ the fluctuations in position were large enough to take the particle out of the field of view, preventing extended observations.

The radial distribution function of a particle subject to restoring force of Eq. 2.4 is:

$$p(r) \propto r \exp\left(\frac{-Ar\left(\frac{r}{r_0}\right)^{\beta}}{(\beta+1)k_BT}\right), \tag{2.5}$$

where the normalization is given by the constraint $\int_0^\infty p(r)dr = 1$. Fig. 2.13 compares the predictions of Eq. 2.5, plotted as $-\ln p(r)$, with the measured radial probability distribution for several values of β. The agreement is good for $\beta > -0.4$. To account for the disagreement when $\beta < -0.4$, Brownian dynamics simulations were performed for a particle subject to the restoring force of Eq. 2.4, taking into account the feedback latency of 1.6 video frames. Including the effect of delay led to excellent agreement between theory and experiment. The feedback delay becomes most significant as $\beta \to -1$ and $r \to 0$ because the restoring force becomes increasingly kinked near the origin.

As a second illustration of the generation of arbitrary force fields, a 200 nm particle was subjected to a force field corresponding to a double-well potential. The feedback voltage was:

$$\mathbf{V}(\mathbf{r}) = (k_x x - \gamma x^3)\hat{x} - k_y y\hat{y}. \tag{2.6}$$

Hopping rates are obtained by fitting the data with a Hidden Markov Model, in which the two "hidden" states correspond to the particle residing in one or the other minima of the potential. Each hidden state is assumed to generate Gaussian-distributed observations of the position of the particle.

Kramers' theory predicts that the hopping rate, W, in a potential double-well is given by:[123]

$$W = \frac{\sqrt{|k_s|\,k_1}}{2\pi\Gamma} e^{\frac{-\Delta U}{k_BT}}, \tag{2.7}$$

where k_s and k_1 are the curvatures of the potential along the reaction coordinate at the saddle point and the starting minimum, respectively. $\Gamma = 6\pi\eta a$ is the drag

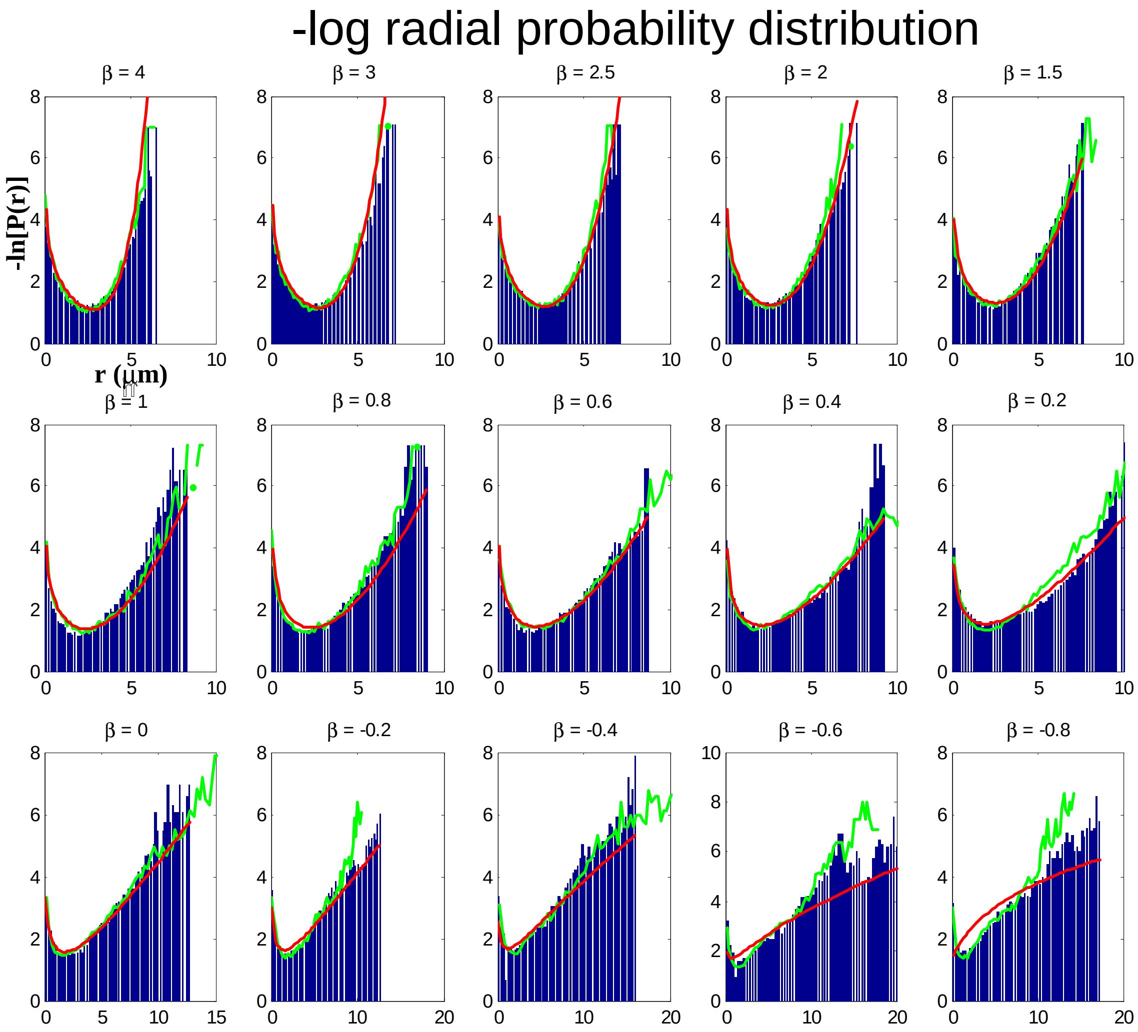

Figure 2.13: Radial probability distributions (plotted as $-\ln p(r)$) for a 200 nm particle in a power-law potential. (Blue bars) measured distribution; (red dots) Eq. 2.5; (green line) numerical simulation.

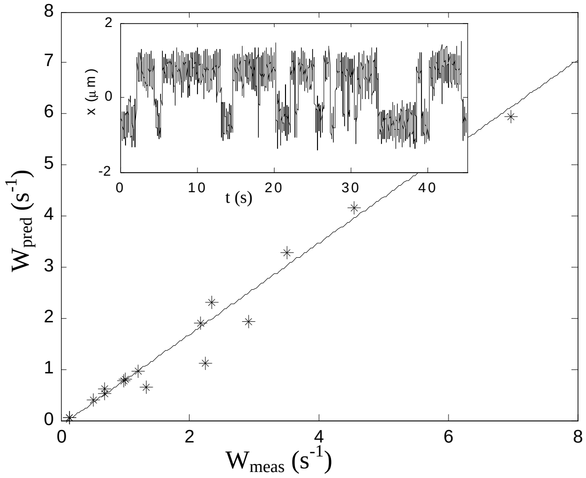

Figure 2.14: Comparison of experimental and theoretical hopping rates for a 200 nm particle in a double potential well. Eight trajectories were acquired (10,000 data points each), leading to 16 experimental rates (left → right and right → left for each trajectory). The trend-line has a slope of 0.89 (ideal = 1), which is reasonable given uncertainties in the size of the particle. Inset: representative trajectory of a single particle.

coefficient of the particle, and ΔU is the potential of the saddle point relative to the starting minimum. The parameters k_s, k_1, and ΔU are, in principle, determined by the feedback parameters k_x and γ. However, a slight fluid drift during the experiments tended to bias the particle toward one potential well over the other. Better agreement between the measured hopping rates and Eq. 2.7 was obtained when k_s, k_1, and ΔU were extracted from the measured distribution of particle positions, assuming that the distribution was related to the potential via a Boltzmann distribution. Figure 2.14 compares the measured hopping rates with the predictions of Eq. 2.7. McCann *et al.* have performed much more accurate tests of the Kramers theory using silica particles in a double optical trap. [81]

Here I have presented a few simple force fields to illustrate the ABEL trap. However, force fields of practically arbitrary complexity can be constructed. Such force fields may be useful for studying diffusion in lattices, in the presence of static or dynamic disorder, or in time-varying fields. Furthermore such force fields may be useful in sorting or assembling nanoscale components.

2.6 Trapping fluctuations in concentration

Rather than trapping individual particles in the ABEL trap, it is possible to trap statistical fluctuations in the density of particles. This rather subtle trick may be useful in instances where the particles are too dim, too fast, or too concentrated to resolve individuals. These experiments were carried out with a very early version of the ABEL trap: gold electrodes for the feedback, and imaging with a Genwac camera.

The device uses exactly the same hardware as the ABEL trap (four gold electrodes coming to the corners of a diamond; a thin layer of solution above the diamond; fluorescence detection and a feedback circuit), but uses a different software algorithm. The software divides the image of the trapping volume into an $m \times m$ grid ($m = 3$ in the proof-of-principle below). If there are on average n particles in each grid-element, then the exact number of particles in each grid element fluctuates by roughly $n^{1/2}$. The correlation time of the fluctuations is roughly the time for a particle to diffuse a distance equal to the grid-spacing. At each frame, the software searches the entire grid to find the element with the largest positive fluctuation in brightness (and therefore in n). The feedback circuit then induces an electrophoretic drift that shifts the contents of this grid element to the center of the grid (the contents of all other grid elements are also shifted by the same amount, but this doesn't matter). After roughly one correlation-time, the center grid element loses its supremacy and a new grid element becomes the brightest. All the particles are then shifted so that the contents of the new brightest element sit at the center.

A time-lapse image of the density of particles shows an enhancement at the center of the grid. The maximum value of the concentration-enhancement (assuming perfect feedback) equals the mean value of the maximum concentration-fluctuation among all the grid-elements. This enhancement mechanism is subtle, because an image of the distribution of particles at any one instant is indistinguishable from the distribution that would occur in the absence of feedback.

The concentration trap has some advantages over the ABEL trap. It does not need either the spatial or temporal resolution to see individual particles—it only need to be able to detect fluctuations in the density of particles, averaged over some suitable

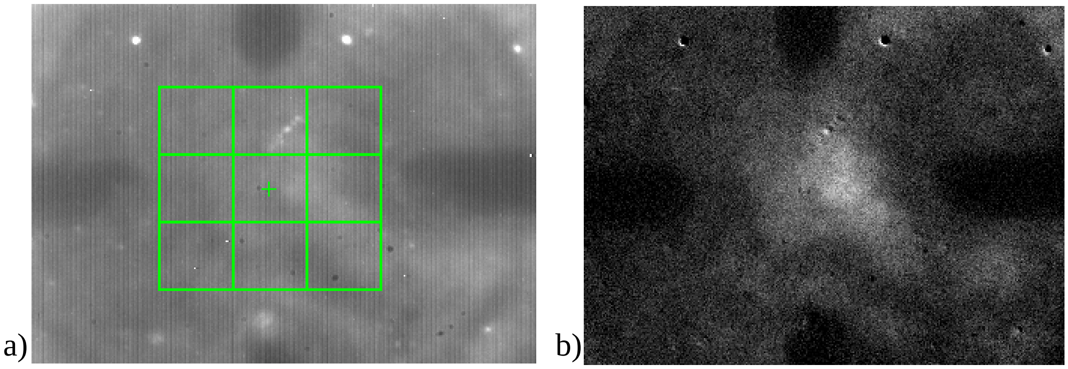

Figure 2.15: Trapping of fluctuations in the density of 20nm particles. a) Average over 6000 frames with feedback on. The 3 x 3 trapping grid is overlayed on the image, with the target position marked by a "+". b) Image in (a) with the background (average of 6000 frames with feedback off) subtracted. The central box has an enhancement of 25%.

volume. A useful analogy is that this new trapping scheme is to the ABEL trap what Fluctuation-Correlation Spectroscopy (FCS) is to single-molecule spectroscopy, i.e. taking advantage of small-number statistics vs. taking advantage of number = 1 statistics.

I demonstrated concentration trapping with 20 nm fluorescent nanospheres in an array with a 15 μm interelectrode gap. I first created an image of the array with the feedback off, averaged over 6000 frames (100 s). Then I turned on the feedback and averaged the image of the array for another 6000 frames. The difference between these two images is shown in Fig. 2.15. There is a clear enhancement in the density of particles near the center of the array.

To model the dynamics of the concentration trap, we need to find the distribution of the intensity of the brightest of the nine boxes. Assuming that the particles move independently, the distribution of intensity in an arbitrarily selected cell with the feedback off obeys a Poisson distribution with parameter λ:

$$P_\lambda(n) = \frac{e^{-\lambda}\lambda^n}{n!}, \tag{2.8}$$

with first and second moments $\langle n \rangle = \lambda$, and $\langle (n-\lambda)^2 \rangle = \lambda$. What is the probability

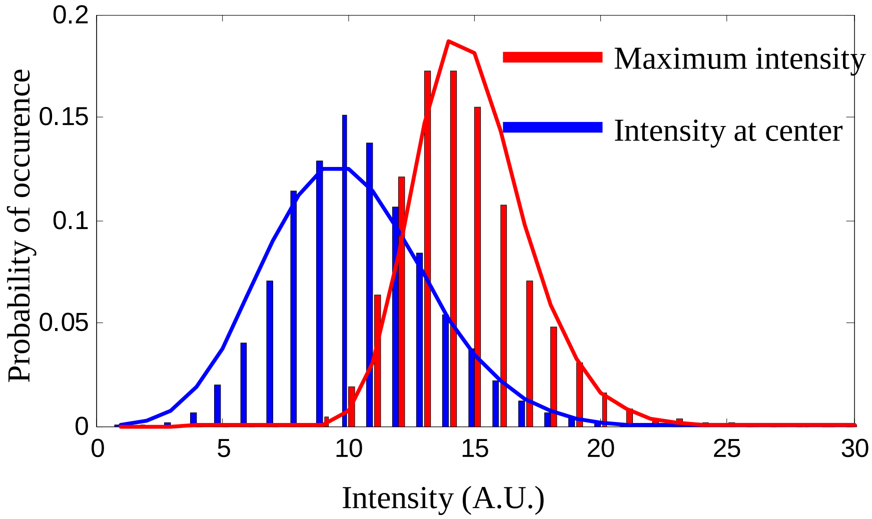

Figure 2.16: Histogram of the intensity in the central box with the feedback off (blue), and the maximum intensity of all nine boxes, also with the feedback off. The average maximum intensity (12.54) is 23% greater than the average overall intensity (10.20). This theoretical maximum compares favorably with the experimental enhancement of 25%

distribution of the maximum of m independent samples of the Poisson distribution? The cumulative probability that one sample has a value of n or less is

$$G_\lambda(n) = \sum_{i=0}^{n} P_\lambda(i). \tag{2.9}$$

Since each sample is independent, the cumulative probability that m samples are all $\leq n$ is just $G_\lambda(n)^m$. We want the probability that all samples are $\leq n$ but not all samples are $\leq n-1$. This is given by

$$P_\lambda(\max(n)) = \left(\sum_{i=0}^{n} P_\lambda(i)\right)^m - \left(\sum_{i=0}^{n-1} P_\lambda(i)\right)^m. \tag{2.10}$$

Fig. 2.16 shows the experimental distributions of $P(n)$ and $P(\max(n))$ and the fits to Eqs. 2.8 and 2.10, with an average of $\lambda = 10$ particles per box.

2.7 Trapping single biomolecules

Single biomolecules in free solution have long been of interest for detailed study by optical methods, but Brownian motion prevents the observation of one single molecule for extended periods. We used the ABEL trap to trap individual protein molecules in free solution, under ambient conditions, without requiring any attachment to beads or surfaces. We also demonstrate trapping and manipulation of single virus particles, lipid vesicles, and fluorescent semiconductor nanocrystals. To our knowledge, this represents the first report of trapping of individual biomolecules in free solution.

With the high-speed software feedback, the smallest objects that could be reliably trapped in water were ~ 20 nm in diameter. However, the trapping strength of the ABEL trap may be increased by increasing the viscosity of the trapping medium. This slows down the diffusion enough for the feedback loop to generate a restoring force before an object escapes from the field of view. Increasing the field of view (FOV) increases the distance the particle has to go before it escapes from the trap and could also allow trapping of smaller particles at a given feedback latency but with increased spatial fluctuations. But if an increase in the FOV is achieved by reading out a larger number of pixels from the CCD (we normally only read out a small fraction of the CCD), then the frame-rate of the camera slows down and the image processing software runs more slowly; these effects combine to counteract the gain from the increased FOV. The other way to increase the FOV is to use a lower magnification objective or hardware binning of the pixels. However, once the width of the point-spread-function of the microscope becomes smaller than the dimensions of one pixel, the signal-to-noise ratio decreases. It becomes increasingly difficult to locate the particle amidst the fuzz from pixel-noise and background autofluorescence. As cameras, computers, and image-processing software improve, undoubtedly camera-based ABEL traps will become more powerful.

2.7.1 TMV

We trapped individual particles of fluorescently labelled Tobacco Mosaic Virus (TMV, 300 nm long x 15 nm in diameter). Particles of TMV (ATCC, Manassas, VA) were

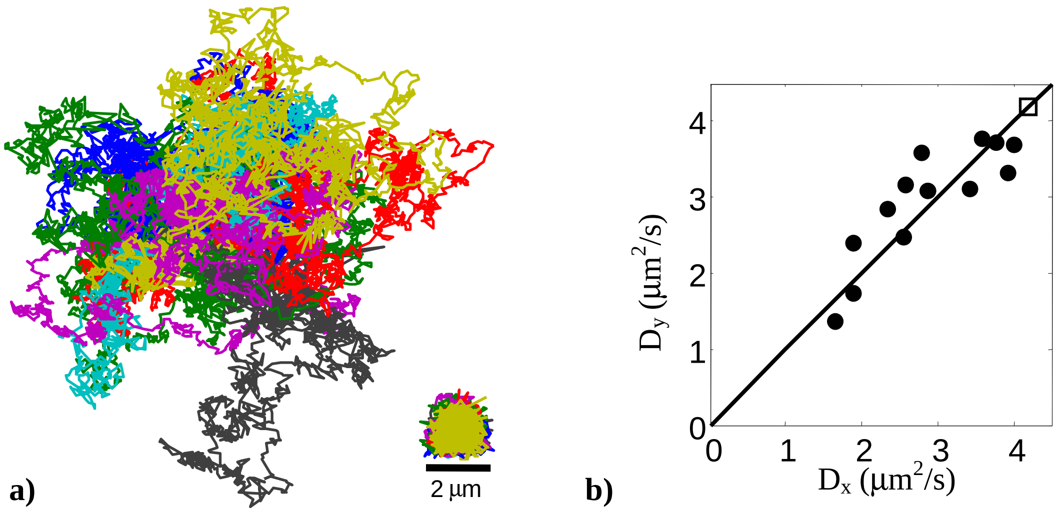

Figure 2.17: TMV pseudo-free trajectories. a) Measured (lower right) and pseudo-free (left) trajectories of 13 trapped particles of TMV. Each particle was trapped for 6.8 s (2000 video frames at 3.4 ms/frame). The pseudo-free trajectories are offset for clarity. b) Diffusion coefficients along the x- and y-axes for the 13 particles trapped in (a). If there were no statistical error in the measurements, the data points would fall along the line. The r.m.s. deviation of D_x from D_y, $\left\langle [2(D_x - D_y)/(D_x + D_y)]^2 \right\rangle^{1/2}$, is 9%, while the r.m.s. deviations of D_x and D_y from their ensemble-averaged values are 28% and 26%, respectively, indicating heterogeneity in the ensemble above the noise level of the measurement. The square indicates the value from dynamic light scattering.

suspended at a concentration of 50 nM in a buffer of 0.1 M $NaHCO_3$ (pH 8.0). They were incubated with 1 mM Cy3-succinimidyl ester (Molecular Probes) at 4 C for 48 hrs for labelling of exposed amines. Unreacted dye was removed by gel filtration followed by dialysis against distilled water. The trapping was performed in distilled water at a TMV concentration of 20 pM. The viruses were excited at 532 nm. From the record of the position and the feedback voltage we extracted pseudo-free trajectories for all the trapped molecules. Fig. 2.17 shows these pseudo-free trajectories.

These pseudo-free trajectories show significant heterogeneity in the diffusion coefficient of the trapped particles—heterogeneity that would not have been apparent from a bulk experiment. The extracted mobility had an average value of 5×10^{-4} cm^2/Vs, consistent with the literature value of 5.2×10^{-4} cm^2/Vs.[52] Fig 2.17b shows the diffusion coefficients along the x- and y-axes. From the strong correlation between D_x and the independently measured D_y, we conclude that the heterogeneity reflects an intrinsic property of the trapped particles rather than a statistical error due to the stochastic nature of the measurement. No particles showed a diffusion coefficient larger than the literature value of 4.19 $\mu\text{m}^2/\text{s}$,[132] from which we conclude that the heterogeneity is due to aggregation of the TMV virions. TMV has a rotational relaxation rate of 318 s^{-1}, which guarantees that the rotational anisotropy averages out after a few video frames, while the diffusion coefficients are calculated by averaging the displacements over 6.8 s. Thus anisotropy of the TMV does not contribute to the measured heterogeneity of D. Due to the many different ways in which multiple TMV particles can bind together, we do not expect to see clustering of the diffusion coefficients corresponding to distinct numbers of particles in an aggregate. In contrast to the experiments on TMV, trapped 200 nm fluorescent polystyrene nanospheres showed considerably less heterogeneity in D.

In one of the first papers on optical trapping, Ashkin demonstrated trapping of TMV particles in a concentrated solution.[4] In that experiment it was not possible to control the number of TMV virions in the trap because each virion experienced essentially the same attractive optical potential. In contrast, the ABEL trap always traps exactly one particle: the Brownian motion of distinct particles is uncorrelated, so the force used to cancel the motion of one particle on average augments the motion of all the others. We observed that when two particles enter the trapping region, the mutual center of brightness is trapped, until one of the particles exits the trapping region, at which point the remaining particle is trapped.

2.7.2 Lipid vesicles

To identify the dimmest fluorescent object that could be trapped, we formed 100 nm diameter vesicles of egg-phosphatidylcholine (Egg-PC) doped with 1-2 fluorescent lipid molecules per vesicle. In spite of their low fluorescence intensity, we were able to trap these vesicles and to observe photobleaching in discrete steps (Fig. 2.18). Vesicles containing individual fluorophores were stably held in the trap until photobleaching rendered the vesicles undetectable.

Lipid vesicles of egg-phosphatidylcholine (Egg-PC) were formed according to the procedure in on the Avanti website[1]. Egg-PC doped with 1 part in 10^5 of the fluorescent lipid TRITC-DHPE[2] (Avanti Polar Lipids), was dissolved in chloroform and then dried under vacuum. Lipids were hydrated in buffer, and then homogenized by repeated extrusion through a polycarbonate membrane with 100 nm pores. Vesicles were then diluted in distilled water to a concentration of 20 pM. The vesicles were excited at 532 nm.

Attempts to study transmembrane proteins in lipid vesicles at the single-molecule level have been hampered by the diffusion-limited observation time of free vesicles.[138] Furthermore, transmembrane proteins in planar supported lipid bilayers are often immobile,[53] although adding an extra bilayer ameliorates this problem.[93] Recent work has shown that lipid vesicles may be tethered to a surface via DNA linkers,[137] or gently immobilized via polymer-induced depletion forces.[136] The ABEL trap will open avenues for single-molecule studies of transmembrane proteins without the complications of tethering chemistry, albeit at the price of only studying one vesicle at a time.

2.7.3 Single molecules

The response time of the ABEL trap was insufficient to trap objects smaller than ~ 20 nm diameter in buffer ($D > 22\ \mu\text{m}^2/\text{s}$), although this will be possible in the future with faster imaging and feedback. To trap smaller objects we increased the viscosity of the trapping medium by adding glycerol or sucrose. In solutions of 50% glycerol ($\eta \approx 6\eta_{H_2O}$) we were able to trap single molecules of large proteins (GroEL and B-phycoerythrin) and single fluorescent CdSe nanocrystals (Fig. 2.18).

GroEL was fluorescently labeled at exposed amines with an average of 6 molecules of Cy3-succinimidyl ester (Molecular Probes) per tetradecamer of GroEL. A solution of 20 pM GroEL was dissolved in a buffer of 1 mM DTT, Tris-HCl, 50 mM KCl,

---

[1] http://www.avantilipids.com/PreparationOfLiposomes.html

[2] N-(6-tetramethylrhodaminethiocarbamoyl)-1,2-dihexadecanoyl-sn-glycero-3-phosphoethanolamine

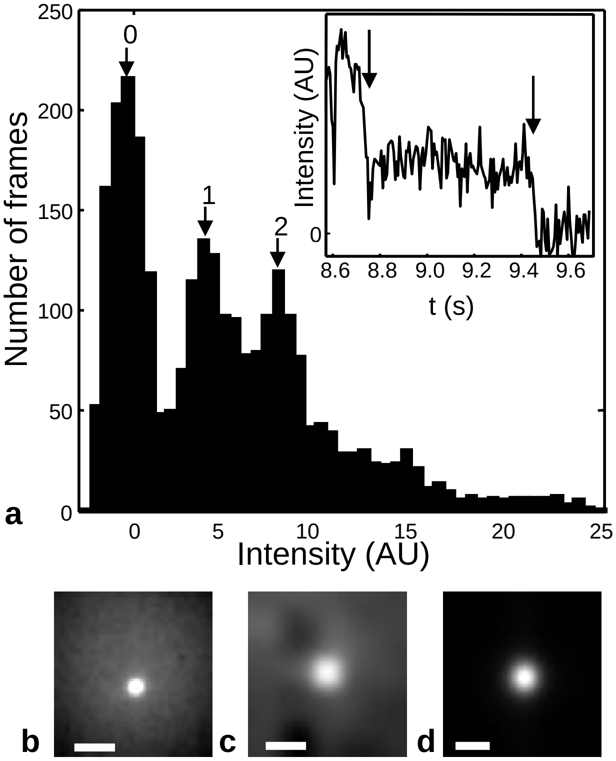

Figure 2.18: Trapping of individual fluorescent objects. a) Histogram of intensities of individual trapped fluorescently labeled vesicles. The vesicles had an average diameter of 100 nm and were composed of Egg-PC with 1 part in 10^5 of the fluorescent lipid TRITC-DHPE. A total of 26 vesicles were trapped, for a cumulative 2690 video frames (at 6.5 ms/frame). Intensities were computed from a sliding average with a 26 ms window. Peaks indicate vesicles containing 0, 1, or 2 fluorophores, as well as an unresolved contribution from more highly labeled vesicles. Some intensity values are negative because the background subtraction was set to yield zero mean intensity when the trap was empty. Inset: a typical trajectory showing 2-step photobleaching (arrows) of a vesicle containing two fluorophores. The vesicle was trapped with only one active fluorophore for $\sim$ 700 ms (between arrows). b-d) Time-averaged images of trapped single molecules and CdSe nanocrystals. b) A single molecule of B-phycoerythrin (average of 500 images taken over 2.2 s). c) GroEL labeled with Cy3 (average of 10000 images taken over 45 s). During this interval, several single molecules were sequentially trapped, eventually photobleached, and released from the trap. d) A single CdSe fluorescent nanocrystal (average of 20000 images taken over 90 s). Scale bar in b-d is 2 μm.

and 5 mM $MgCl_2$, pH 7.4. An equal volume of glycerol was added to increase the viscosity. The molecules were excited at 532 nm. Stepwise photobleaching was often observed in the trapped molecules.

B-phycoerythrin is intrinsically fluorescent, and was trapped without any artificial labelling. B-phycoerythrin (Molecular Probes) was dialyzed against a buffer of 100 mM phosphate, 100 mM NaCl, pH 7.4. Just prior to trapping, the solution was mixed with an equal volume of glycerol, and 1 mg/mL Bovine Serum Albumin was added to prevent adsorption. The molecules were excited at 532 nm. The molecules of B-phycoerythrin showed single-step photobleaching, consistent with the understanding that the many fluorophores in the molecule are strongly coupled and form a single excitonic system.[49]

Streptavidin-coated CdSe nanocrystals (QD565, Qdot Inc.) were dissolved to a concentration of 20 pM in a solution of 47% distilled water, 48% glycerol, 4% β-mercaptoethanol, and 1% an anti-adsorption polymer from Applied Biosystems. The nanocrystals were pumped at 488 nm. Trapped nanocrystals showed fluorescence blinking, and were typically lost from the trap whenever they experienced an off-time greater than a few ms.

With the ability to overcome the effects of Brownian motion, we expect that the ABEL trap will enable new biophysical measurements. It is clear that other spectroscopic techniques can be brought to bear on trapped molecules, such as fluorescence polarization/anisotropy, fluorescence lifetimes, binding events, and Förster resonant energy transfer (FRET). The ABEL trap could provide the analysis station for a device analogous to the well-known FACS (fluorescence-activated cell sorter), but now for single biomolecules. The ability to trap single viruses and trigger the release of their genetic material at a defined location is a tantalizing prospect.[43] By trapping lipid vesicles containing transmembrane proteins, one may study the action of these proteins at the single-molecule level in a near-native environment; these proteins are notoriously sensitive to departures from the cellular milieu. Enzymes that produce a fluorescent substrate are particularly attractive candidates for study because they are not subject to photobleaching.[101] The ABEL trap would provide a non-perturbative way to study the folding of single proteins in solution.[74]

2.8 Appendix: Fabrication of glass microfluidic cells

All microfabrication was performed in the Stanford Nanofabrication Facility. The processing steps are outlined in Fig 2.19. Transparency masks were designed in Adobe Illustrator and printed at a resolution of 3600 dpi on a mylar transparency. Circular wafers of Corning 7740 glass (700 μm x 100 mm) were cleaned in a Piranha solution (80% Conc. H_2SO_4, 20% H_2O_2) and then coated with 100 nm of silicon via chemical vapor deposition (CVD). The front side of the wafer was coated with 1.6 μm of Shipley SPR 3612 resist using a standard HMDS prime followed by a spin-coat and soft-bake. The pattern was exposed in a Karl Suss mask aligner (365 nm, 15 mW/cm^2, 2.5 s), and developed in Shipley LDD-26 W for 60 s.

The back side of the wafer was then coated with a protection layer of 1.6 μm of SPR 3612 resist. The wafer was given a hard-bake of 115 C for 5 minutes. The front of the wafer was exposed to a reactive-ion etch (RIE) descum (O_2, 150 mT, 100 sccm, 65 W RF power) immediately followed by a Si etch (SF_6 100 sccm, Freon-22 70 sccm, 100 mT, 55 W) until the exposed Si had been completely removed.

The wafer was then immersed in 49% HF for three minutes (etch rate 7 μm/minute), with the Si and photoresist acting as a double-layer etch mask (without the photoresist, the HF attacked the glass at pinhole defects in the Si; but the photoresist was incapable of acting as an etch-mask alone). The wafer was thoroughly rinsed in clean water and dried. The resist was stripped from the wafer and the front of the wafer was coated with 18 μm of SPR 220-7 resist. The resist was exposed and developed, leaving a 120 μm circle of resist protecting the trapping region and the channels in the immediate vicinity. The back of the wafer was also coated with 18 μm of SPR 220-7 and the wafer was hard-baked. The wafer was again etched in 49% HF, for 10 minutes. The final depth of the channels was $\sim$80 μm, except near the trapping region where they were only 24 μm deep. The channels were not etched to the full depth near the trapping region because the HF etch is isotropic: it widens the channels as it deepens them. Had the channels near the trapping region not been protected, the channels would have fused together.

The wafer was thoroughly rinsed in clean water and the resist was stripped from

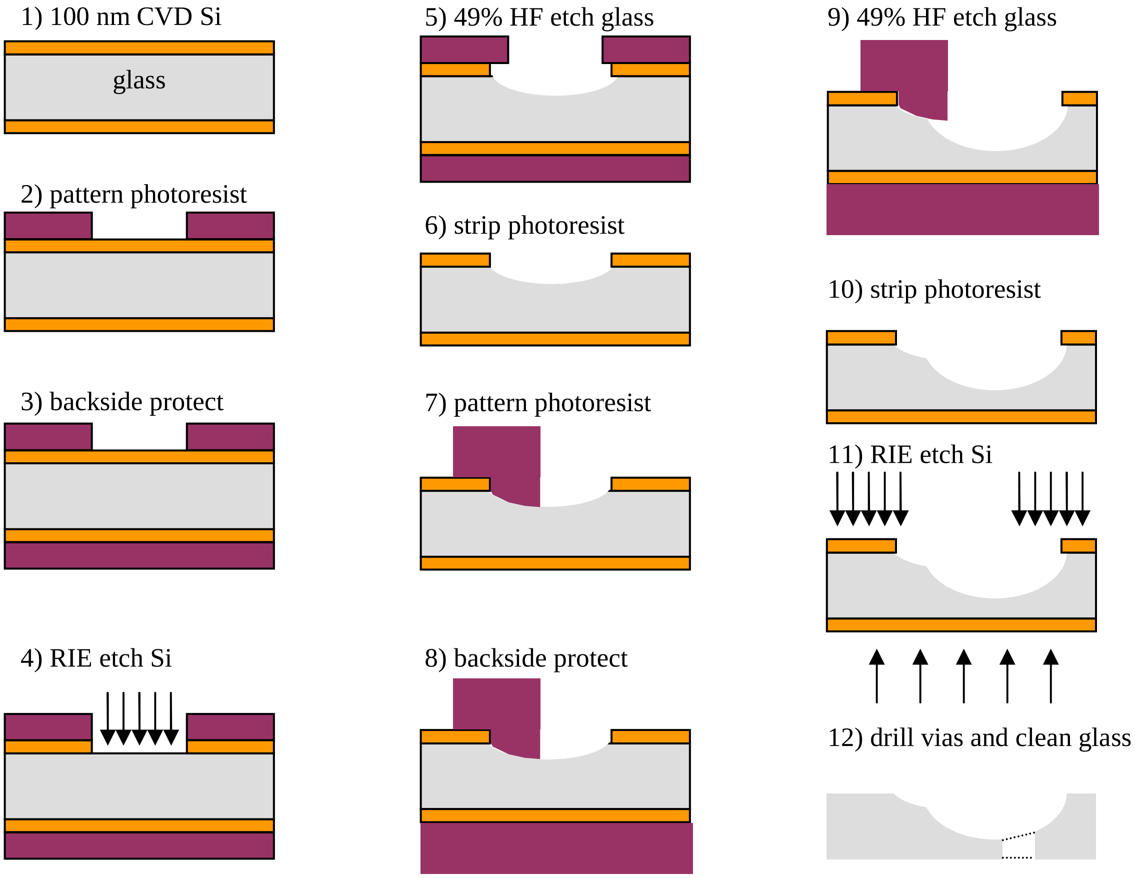

Figure 2.19: Process for fabricating glass microfluidic chips for the ABEL trap. The glass is patterned with two stages of photolithography and HF etching so that the channels near the trapping region are ∼24 μm deep, while the channels far from the trapping region are ∼80 μm deep. The small channel depth near the trapping region keeps adjacent channels from merging, while the greater depth further away decreases the electrical and viscous resistances of the channels.

both faces. Both sides of the wafer were exposed to another RIE polymer descum followed by Si etch, until all of the Si was removed from the wafer. The front of the now-transparent wafer was coated with a protection layer of 7 μm of SPR 220-7, and 0.7 mm holes were drilled in the electrode ports using a high-speed diamond micro-drill. The wafer was diced into individual cells (9 per wafer; each 25 mm x 25 mm) using a diamond-blade dicing saw, and the protection layer of resist was removed with acetone. The finished chip was cleaned by heating and sonicating in Alconox detergent for 1 hr., followed by a 10 min. etch in an Ar plasma (Harrick).

The bottom piece of glass in the trap was a standard #1 coverslip, 25 mm x 25 mm. The coverslip was cleaned by heating and sonicating in Alconox detergent for 1 hr. A $\sim$10 μm tall annular spacer was formed on the coverslip by placing a clean United States nickel over the center of the coverslip and then applying a light coat of spraypaint, with the coin acting as a shadow-mask. The procedure for preparing the coverslip was sufficiently simple that a new coverslip was prepared for each experiment.

Chapter 3

Dynamics of a single molecule of DNA

In this chapter I show how the ABEL trap can be used for detailed studies of the dynamics of biomolecules. When one piece of a biopolymer moves in water, it sets up a flow field that disturbs the motion of other pieces of the polymer. These nonlinear hydrodynamic interactions play a crucial role in determining the rates of biomolecular events which involve large-scale conformational motion, but have been difficult to probe experimentally or to model theoretically. We apply conformational spectroscopy to probe the characteristic equilibrium shape-fluctuations of a single unstretched molecule of λ-DNA in free solution, held in an ABEL trap. In contrast to earlier single-molecule experiments on stretched DNA, we find significant evidence for the underlying nonlinear hydrodynamic interactions. These interactions couple the motions of remote parts of the DNA chain, with possible implications for DNA-protein interactions and DNA packaging.

Thermal fluctuations agitate molecules in solution over a broad range of times and distances. By passively watching the shape fluctuations of a thermally driven biomolecule, one can infer properties of the underlying interactions that determine the motion. The hydrodynamic interaction (HI) is the dominant long-range force for biomolecules in aqueous buffers: it couples motion of one part of a molecule to motion of possibly remote parts of the same molecule. Understanding HI is thus crucial to understanding the rates of molecular events which involve large-scale conformational change, such as folding of proteins and RNA, packaging of DNA, motion of molecular motors, and motion of DNA-binding proteins.

Random coil polymers exhibit the essential features of HI, and hence provide a useful framework for analysis. The simplest model of a random coil polymer is a chain of beads joined by springs; for example, Rouse[102] took each bead as a Brownian diffuser with the same drag and diffusion coefficients it would have in the absence of other beads. This model neglects the fact that each bead is subject to the time-varying flow fields produced by the other diffusing beads. When this HI is included, the underlying dynamics become nonlinear, and thus analytically intractable. The well-known Zimm model[139] includes HI, but restores linearity through a mean-field approximation: each bead is made to interact with the average conformation of its neighbors. Subsequent work has applied sophisticated mathematical techniques to calculate corrections due to fluctuating hydrodynamics[128, 129], but the main questions remain: how much error is introduced by pre-averaging hydrodynamic interactions,[44] and when can the intrinsic nonlinear dynamics be observed?

Long before polymers were studied at the single-molecule level, many clever experiments applied dynamic light scattering (DLS), neutron scattering, and fluorescence correlation spectroscopy (FCS) as indirect probes of polymer dynamics[59, 16, 72]. DLS has been profitably applied to study large ensembles of free-floating DNA molecules (For reviews see [38, 95]). FCS has also been used to probe the dynamic fluctuations of small numbers of fluorescently labelled DNA molecules.[78, 118] Scattering and FCS experiments are complementary in that scattering probes the fluctuations at a particular k-vector, while FCS probes the fluctuations at a particular position vector.

Two-time correlation functions measured by DLS or FCS show complex non-exponential decay. This non-exponential decay indicates that the basis onto which the motion is projected (k-vectors or position vectors) are not the eigenstates of the time-evolution of the system. That is, each measurement mixes the dynamics of many eigenstates into a single observable. The basis functions used in DLS and FCS are determined by the measurement technique, rather than by the physics of the molecule. A primary aim of this work is to extract from experiments a natural set of basis functions with which to describe polymer dynamics.

Here are some further limitations of DLS and FCS for studying polymer dynamics:

1. Both techniques provide low-dimensional projections of the full molecular dynamics, possibly missing important physics.
2. Both techniques are insensitive to internal dynamics that are slower than the typical transit time for a molecule across the beam.
3. Both techniques only probe ensemble-averaged second-order correlation functions, without measuring the entire distribution of underlying states. This property makes these techniques insensitive to deviations from the linearized Zimm theory.

Quake *et al.* used laser tweezers to study the dynamics of partially extended DNA in solution yet failed to find deviations from the Zimm theory.[100] This negative result is not surprising, because extending a molecule weakens the internal hydrodynamic interactions, rendering the nonlinearity harder to detect. Subsequent experiments have probed DNA under a wide range of twists and extensions (for reviews see [115, 110]). In contrast, the equilibrium (i.e. unstretched) dynamics of single DNA molecules have received relatively little attention,[78, 111, 54] due to the challenge of following a molecule as it diffuses away from the field of view. One notable exception is the experiment by Maier and Rädler on DNA molecules freely diffusing on supported cationic lipid bilayers.[79] In that case the DNA diffused slowly enough to observe with video microscopy, but the conformation and dynamics were dominated by the interaction with the bilayer. It appears that these results do not generalize to DNA in 3-D solution.

3.1 DNA trapping setup

Our experimental method consists of:

1. Acquiring a large number of images showing the free-solution shape fluctuations of single fluorescently labeled molecules of DNA;
2. Identifying the conformational normal modes (analogous to the wavefunctions of an electron or the normal modes of a drum); and
3. Determining whether the dynamics in these modes can be fit to a linear model, as required by the Zimm theory.

The observed deviations from Zimm theory verify that HI effects are present in DNA, and may play an important role in the dynamics of more complex biomolecular systems.

To study a single molecule in equilibrium, one would like to eliminate the motion of the center of mass, without affecting internal motions. We used an ABEL trap with a glass cell and high-speed video feedback to achieve this. The molecule to be trapped is confined to a thin fluid layer (< 1 μm thick, slightly larger than the radius of gyration R_G for λ-DNA, ~ 700 nm) in a glass microfluidic cell. An automated video tracking system follows the Brownian displacements (via fluorescence microscopy), and for every frame, applies feedback voltages to the cell to induce an electrokinetic drift that approximately cancels the Brownian motion.

Double-stranded λ phage-DNA (Molecular Probes) was dissolved in a buffer of 10 mM Tris-HCl, 10 mM NaCl, 1 mM EDTA, pH 8.0. The fluorescent dye YOYO-1 (Molecular Probes) was added at a concentration of 1 dye:10 base pairs of DNA and the mixture was incubated at room temperature in the dark for 30 min. An oxygen scavenger system of glucose (4.5 mg/mL), glucose oxidase (0.43 mg/mL), catalase (72 μg/mL), and β-mercaptoethanol (5 μL/mL) was added to the solution to reduce photobleaching. An anti-adsorption polymer (Applied Biosystems) was added at a concentration of 10% to prevent DNA sticking to the walls of the cell. The molecules were excited at 488 nm and fluorescence was collected through a 495 nm long pass filter. Under the experimental conditions, λ-DNA has a persistence length of $l_p \approx 60$ nm and a contour length of $L \approx 20$ μm.

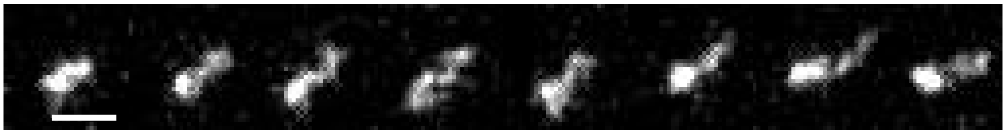

Figure 3.1: Series of images showing equilibrium conformational fluctuations of fluorescently labeled λ-DNA, taken at 4.5 ms/frame (here every 8^{th} image from the full movie is shown). Scale bar 2 μm.

Molecules of double-stranded λ-DNA were held in the ABEL trap and a two-dimensional projection of their conformational motions was recorded with video microscopy at a time resolution of 4.5 ms/frame. 21 separate molecules were trapped, each for between 9 and 18 s (yielding between 2000 and 4000 images/molecule; total data set 58,421 frames). Several frames showing the shape fluctuations that are the focus of this analysis are shown in Fig. 3.1. The molecules were labeled with a uniform density of fluorophores, so the fluorescence intensity at each point in an image was proportional to the density of DNA averaged over the point-spread function of the microscope at a corresponding point in the sample.

An important question is whether the trapping feedback fields affect the conformation or dynamics of the DNA. In a theoretical study of free solution electrophoresis of a polyelectrolyte whose persistence length l_p is greater than the Debye screening length λ_D (consistent with the present experiment; $l_p \approx 60$ nm, $\lambda_D \approx 2$ nm), Long *et al.*[77] proved (a) that application of an electric field has no effect on the internal conformation or dynamics, and (b) that the electrophoretic mobility is independent of the instantaneous conformation. An intuitive explanation for these results is that the applied electric field acts uniformly on the backbone of the molecule, imposing a body force that is independent of the conformation. To test for the presence of a coupling between the electric field and the internal conformation, we calculated the correlation of the applied voltage with the fluorescence intensity at each pixel in the image. We found no correlation above noise, and thus conclude that the trap does not affect the internal dynamics.

3.2 Average Conformation of DNA

To test the precision of the ABEL trap data and to confirm that the trap was not affecting the conformation of the DNA, we first analyzed the time-averaged conformation. A trapped molecule undergoes small fluctuations about the trap center, so we translated each image to keep the center-of-mass fixed. Let $S_i(t)$ be the intensity at pixel i, where the index i runs over all pixels in the 32 x 32 image (i.e. $i \in [1, 1024]$). The simplest measure of the molecular conformation is the time-average fluorescence intensity (and hence molecular density) at each pixel, $\langle S_i(t) \rangle$. Fig. 3.2 shows that the spatial distribution of density has fat tails relative to a Gaussian. Here we derive a model to account for this small ($\sim 2\%$) effect. The essential idea is that different segments of the molecule follow different spatial distributions (the ends wander further from the center of mass than does the middle). Although each segment follows a Gaussian distribution, the total density distribution is the sum of many Gaussians of distinct widths, and thus is not a Gaussian.

Consider a 2-D random walk of N steps joining $N + 1$ identical beads, where each step is independently chosen from a Gaussian distribution with standard deviation σ. The mean-square end-to-end separation is $N\sigma^2$, and it is simple to show that the mean-square separation of the center of mass from one end of the chain is $N\sigma^2/3$. (The derivation is exactly the same as that given in section 1.5.) Due to the Central Limit Theorem, the distribution of locations of the center of mass (keeping one end of the chain fixed), is a Gaussian:

$$P_0(\mathbf{R}_{CM}) = \frac{3}{2\pi N\sigma^2} \exp\left(\frac{-3R_{CM}^2}{2N\sigma^2}\right). \tag{3.1}$$

An internal bead divides the chain into pieces of lengths ϵN and $(1 - \epsilon)N$, where $0 \leq \epsilon \leq 1$. The centers of mass of the two pieces are independently distributed according to Eq. 3.1, with N replaced by ϵN and $(1 - \epsilon)N$, respectively. The mass of each piece of the chain is proportional to its length, so the position of the total center of mass is given by the weighted sum $R_{CM} = \epsilon R_{CM}^L + (1 - \epsilon)R_{CM}^R$, where the L, R superscripts denote the two pieces of the chain. The distribution of the center of mass is obtained from the addition-of-errors formula as:

$$P_\epsilon(\mathbf{R}_{CM}) = \frac{3}{2\pi N\sigma^2(3\epsilon^2 - 3\epsilon + 1)} \exp\left[\frac{-3R_{CM}^2}{2N\sigma^2(3\epsilon^2 - 3\epsilon + 1)}\right]. \tag{3.2}$$

While Eq. 3.2 has been derived as the spatial distribution of the center of mass relative to a fixed chain element at contour position ϵN, it can equally be thought of as the spatial distribution of the chain element at contour position ϵN relative to a fixed center of mass. The chain is uniformly labeled with fluorophores, so each chain element contributes an intensity pattern given by Eq. 3.2. The total density of chain elements at position $\mathbf{r}$ is given by integrating Eq. 3.2 over all ϵ:

$$S(\mathbf{r}) = \frac{3}{2\pi R^2}\int_0^1 \frac{\exp\left(-3r^2/[2R^2(3\epsilon^2 - 3\epsilon + 1)]\right)}{(3\epsilon^2 - 3\epsilon + 1)} d\epsilon \tag{3.3}$$

where $R^2 \equiv N\sigma^2$ is the mean-square end-to-end distance of the polymer. As with a Gaussian, Eq. 3.3 has only one free parameter. Eq. 3.3 agrees with the data to within 0.1%, implying that excluded volume interactions are not needed to describe the average density for λ-DNA under these conditions. Furthermore, this analysis illustrates the high precision attainable with data from the ABEL trap.

3.3 Conformational fluctuations

We now analyze the shapes of λ-DNA, first considering only the distribution of shapes, and then looking at the dynamics, i.e. how one shape becomes another. Principal Components Analysis (PCA), and its cousin, Normal Modes Analysis, are frequently applied to analyze molecular dynamics simulations of complex biomolecules.[22, 7] These techniques provide a systematic procedure for coarse-graining over atomic degrees of freedom while preserving the large-distance dynamics that are relevant for many functions. Furthermore, PCA is unbiased, in the sense that it uses the data to determine the characteristic motions, without requiring the experimenter to specify a model of the underlying process. We performed PCA[63] on our set of 58,421 video images of DNA to identify spatially separated parts of the DNA that fluctuate in

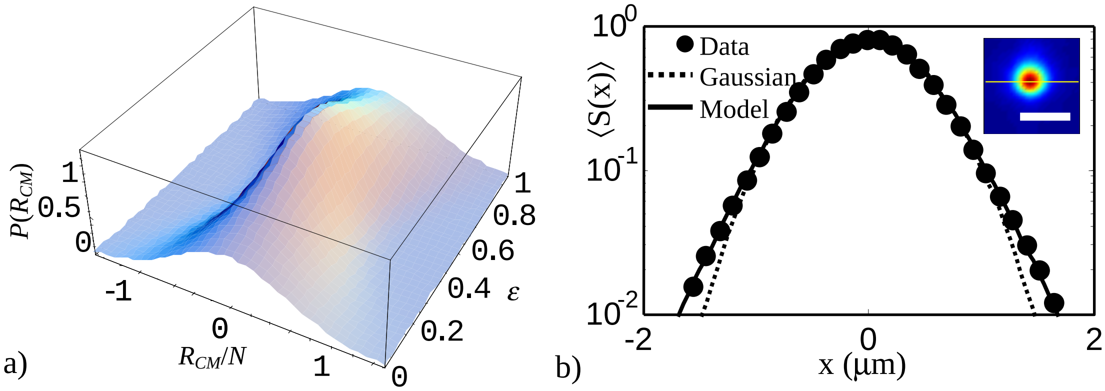

Figure 3.2: Non-Gaussian mass-distribution of a random walk polymer about the center of mass. a) Theoretical distribution of chain elements about the center of mass (Eq. 3.2). The width of the spatial distribution of any chain element depends on the contour position of the chain element. Chain elements in the middle of the chain ($\epsilon = 1/2$) are more narrowly distributed than chain elements near the ends of the chain ($\epsilon = 0, 1$). b) Experimental density distribution around the center of mass. The fitting parameters are: for the 1-D Gaussian fit, $R_G^2 = 0.48$ μm^2; for the fit to Eq. 3.3, $R^2 = 1.37$ μm^2. As expected, these two quantities are nearly in the ratio of 1:3. Inset: pseudocolor image of the average density; yellow line indicates the cross-section plotted in the main figure. Scale bar 2 μm.

synchrony.

Here is how we calculated the Principal Components (PCs). PCA is performed on the equal-time covariance matrix,

$$\rho_{ij} = \langle \delta S_i(t) \delta S_j(t) \rangle \, , \tag{3.4}$$

where $\langle \cdot \rangle$ indicates an average over all time, i and j run over all pixels in the image, and $\delta S_i(t) \equiv S_i(t) - \langle S_i(t) \rangle$ is the deviation in intensity at pixel i from its time-average value. The eigenvectors of ρ_{ij} are called the principal components and form an orthonormal basis.

The 1024 x 1024 equal-time covariance matrix, ρ_{ij}, was numerically diagonalized in Matlab. The eigenvectors with the largest eigenvalues were converted to 32 x 32 images. Eigenvectors 11, 12, 13, and 14 are nearly degenerate, and arrived mixed together due to the presence of statistical noise in the covariance matrix. The space of 4-dimensional rotations among these eigenvectors was manually searched to find linear combinations that had manifest symmetry. These linear combinations were taken to be the “true” eigenvectors. The overall sign of each eigenvector is arbitrary: if $\mathbf{U}_p$ is an eigenvector, so too is $-\mathbf{U}_p$.

Fig. 3.3a shows the first sixteen PCs for λ-DNA, representing the basis in which the DNA shape fluctuates. Starting at the upper left, the dominant PC is a radial breathing mode, followed by a pair of degenerate modes in which the molecule stretches along one axis and contracts along an orthogonal axis, followed by more complex deformations. Each PC is indexed by (n, l), where n is the number of radial nodes and l is the number of azimuthal nodes. PCA implies a picture of the molecule as a gel-like solid, with a spectrum of long-wavelength collective motions. This quasi-continuum picture differs from the traditional Rouse and Zimm pictures, which start with a microscopic model of beads on a string where the location of every bead is accounted for. In the PCA picture, only the total density of beads at each point relative to the center of mass is important. To our knowledge, analytical expressions for the principal components of a random walk polymer have not been developed.

Each PC has associated with it an eigenvalue, λ_p, which is equal to the fraction of the variance of the entire data set that falls along the PC. The equipartition theorem implies that $\frac{1}{2}\lambda_p k_p = \frac{1}{2}k_B T$, from which one can extract the stiffness, k_p of mode p. Since the persistence length is much less than our optical resolution, the stiffness is entirely due to the entropic cost of deforming the molecule. The stiffnesses of the first 45 PCs are shown in Fig. 3.3b, and follow an unexplained semi-regular pattern. In analogy to atomic spectroscopy, one can think of the PCs as the atomic wavefunctions, and the mode stiffnesses as the energy levels.

Use of the principal components achieves a large reduction in the amount of data required to describe the conformational fluctuations, compared to the raw images. While each image contains 1024 pixels, 90% of the variance in the data set is contained in the first 34 principal components. The remaining variance is mostly due to measurement noise. By working in the PC basis, we suggest that numerical simulations of polymer dynamics could be rendered more efficient.

3.4 Conformational dynamics

The PCA analysis is only sensitive to shape deformations that occur within the same video frame, so it provides no information on the dynamics, i.e. how a fluctuation at one time impacts the fluctuations at a later time. Now we study the dynamics, first in real space, and then in the PCA basis.

3.4.1 Real-space dynamics

To learn about the internal dynamics, we must compare images taken at different times. The degree of similarity of two images can be measured by the dot product $\mathbf{S}(t+\tau)\cdot\mathbf{S}(t) \equiv \sum_i S_i(t+\tau)S_i(t)$. We define a correlation function:

$$C(\tau) = \frac{\langle \delta\mathbf{S}(t+\tau)\cdot\delta\mathbf{S}(t)\rangle}{\langle \delta\mathbf{S}(t)^2\rangle}. \tag{3.5}$$

Nonexponential decay in $C(\tau)$ is expected because $C(\tau)$ aggregates fluctuations from all modes of the molecule, each with its own relaxation time. Fig. 3.4a shows $C(\tau)$

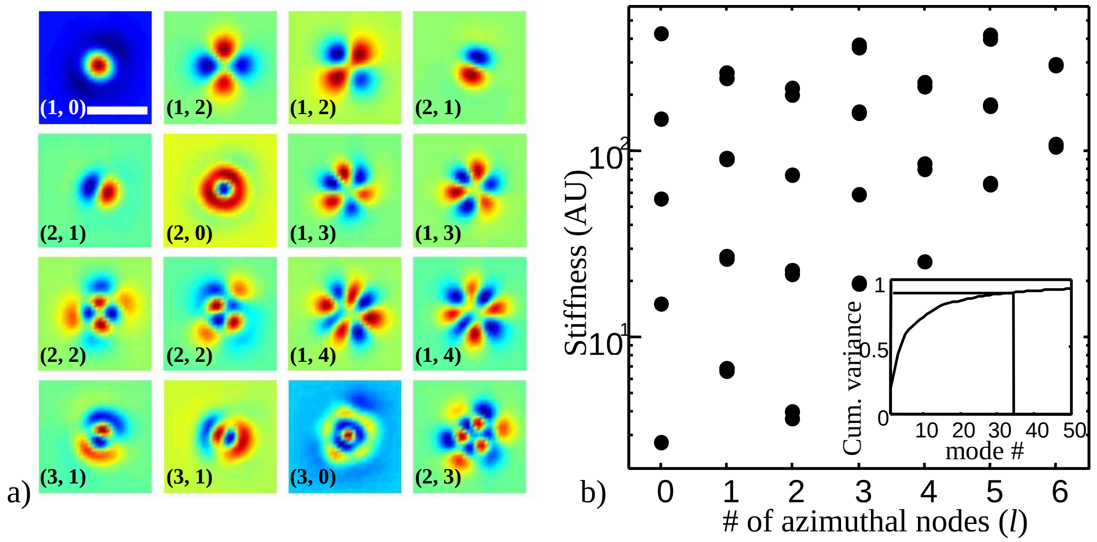

Figure 3.3: Principal Components Analysis of DNA shape fluctuations. a) Experimentally determined principal components of conformational fluctuations in λ-DNA, ordered by their associated eigenvalues. Symmetry forbids the existence of $(1, 1)$ modes (analogous to the $2p$ hydrogen wavefunctions) because amplitude in these modes leads to a displacement of the center of mass. Scale bar 2 μm. b) Stiffness of 45 of the low-energy modes. All modes with $l \neq 0$ are two-fold degenerate. The stiffness follows a semi-regular pattern when plotted on a logarithmic scale. Inset: fraction of the total variance of the data accounted for by the first p modes. The first 34 modes account for 90% of the variance.

and a fit to a stretched exponential with a stretching exponent of $\beta = 0.58$. From De Gennes' models of dynamic light scattering, we expect a stretching exponent of $\beta = 1/2$ for the Rouse model[35] and $\beta = 2/3$ for the Zimm model (see section 3.6.5).[39] The fact that we observe a value of β intermediate between the Rouse and Zimm predictions can be qualitatively explained by the presence of the walls of the ABEL trap. The no-slip condition at the walls leads to a screening of hydrodynamic interactions over distances larger than the trap depth. Thus the long-wavelength modes relax according to the Rouse model, while the shorter-wavelength modes experience hydrodynamic interactions.

The most general second-order measure of the dynamics is the density-density covariance

$$\rho_{ij}(\tau) = \langle \delta S_i(t+\tau)\delta S_j(t)\rangle \, , \tag{3.6}$$

This equation is similar to Eq. 3.4, except that now pixels i and j may be taken from different frames. Thus $\rho_{ij}(\tau)$ is a set of matrices with dimensions 1024 x 1024; one matrix for each value of τ. From $\rho_{ij}(\tau)$ one can learn how a density perturbation in any part of the molecule at time t affects the density in all other parts of the molecule at some later time $t + \tau$, i.e. the complete linear mechanical response function of the molecule (at a length scale $>$ 250 nm). The ABEL trap allows one to obtain this information without ever mechanically perturbing the molecule. Thermal fluctuations provide all possible sets of perturbations, and one merely has to filter the data to select the perturbation of interest. Fig. 3.4b shows one example of $\rho_{ij}(\tau)$. We are not aware of theoretical predictions for the form of $\rho_{ij}(\tau)$, despite its possibly fundamental role in polymer dynamics.

3.4.2 PCA dynamics

To obtain a picture of the dynamics more amenable to comparison with theory, we decomposed each image into the basis of PCs and examined the time dependence of the mode amplitudes, $a_p(t)$. Let $\mathbf{U}_p$ be the p^{th} eigenvector. Then the time-dependent amplitude in $\mathbf{U}_p$ is given by the dot product, $a_p(t) = \delta\mathbf{S}(t) \cdot \mathbf{U}_p$. By construction $\langle a_p \rangle = 0$, so each a_p describes deviations from the average conformation. The PCA

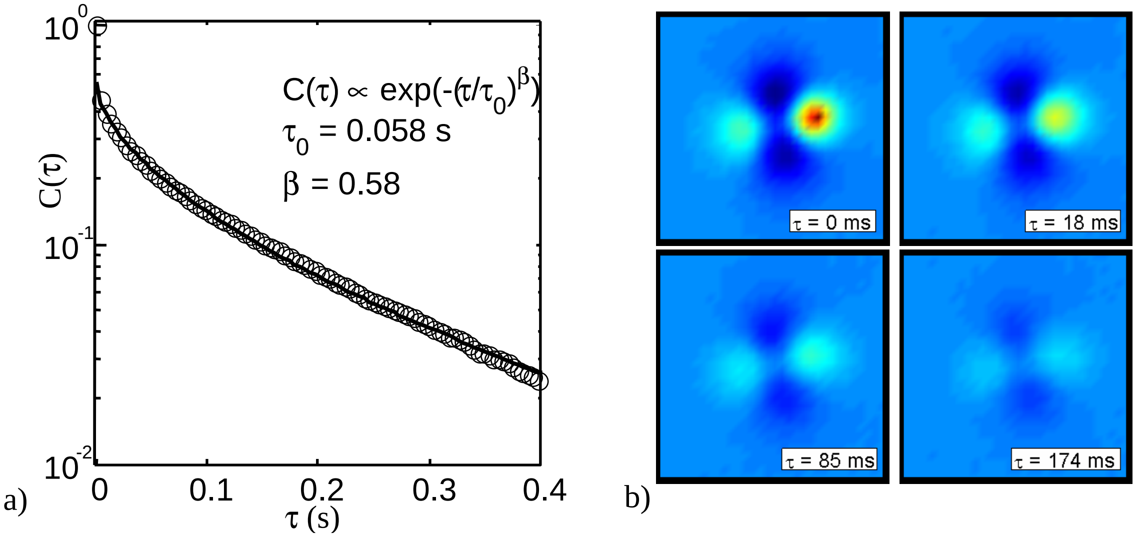

Figure 3.4: Real-space conformational dynamics of λ-DNA. a) Two-time correlation of the global conformational fluctuations, calculated by Eq. 2, (circles), and fit to a stretched exponential (line). The DNA clearly shows non-exponential relaxation at short times. (The similarity in the values of τ_0 and β is coincidental). The $\tau = 0$ term was not included in the fit because it is contaminated by measurement noise. b) Density-density response function, $\rho_{ij}(\tau)$, showing how a perturbation in one part of the molecule propagates over time. In these images index i is fixed and corresponds to a pixel 780 nm to the right of the center of mass. The lobed structure at $\tau = 0$ is due to the requirement that the center of mass remain fixed: a fluctuation in density to the right of the center of mass is necessarily accompanied by a fluctuation of the same sign to the left of the center of mass.

eigenvalues obey $\lambda_p = \left\langle a_p^2 \right\rangle$.

The amplitude in each PC ebbs and flows stochastically as thermal fluctuations and viscous damping add and remove energy. The most general second-order quantity characterizing these dynamics is the time-dependent covariance matrix,

$$\tilde{\rho}_{pq}(\tau) \equiv \langle a_p(t+\tau)a_q(t)\rangle \,, \tag{3.7}$$

where the indices p and q may be truncated at a small value, e.g. 15 in Fig. 3.5a (computed for $\tau = 18$ ms). Due to the sign ambiguity in the eigenvectors, the time-dependent amplitudes, $a_p(t)$ have an arbitrary sign. Thus in $\tilde{\rho}(\tau)$, one may arbitrarily switch the sign of the p^{th} row (for all τ), provided one also switches the sign of the p^{th} column (leaving the diagonal element positive).

If the PCs were also the eigenstates of time evolution, then $\tilde{\rho}_{pq}(\tau)$ would be diagonal for all τ. However, Fig. 3.5a shows that off-diagonal terms arise. The only significant off-diagonal elements connect mode $p = (n \pm 1, l)$ to mode $q = (n, l)$, suggesting that conservation of azimuthal mode number is a selection rule for DNA conformational transitions. That is, only vertical transitions are allowed on the plot in Fig. 3.3b. This selection rule implies that the operator that leads to conformational transitions is circularly symmetric.

The autocorrelations of the mode amplitudes (i.e. the diagonal elements $\tilde{\rho}_{pp}(\tau)$) show non-exponential decay in time (3.5b), a phenomenon due partially to the mode-mixing shown in Fig. 3.5a, and partially to the nonlinear interaction discussed below. Nonetheless, one can associate a characteristic relaxation time with each mode by examining the decay of its autocorrelation at short times. The relaxation times of the diagonal elements were calculated using the formula:

$$\frac{1}{\tau_p} = \frac{1}{\delta t}\frac{\tilde{\rho}_{pp}[2] - \tilde{\rho}_{pp}[3]}{\tilde{\rho}_{pp}[2]}. \tag{3.8}$$

The second and third elements of $\tilde{\rho}_{pp}$ were used (rather than the first and second), to avoid contaminations from shot-noise and other δ-correlated noise sources. These relaxation times are shown in Fig. 3.5b, and are well fit by a power law $\tau_p \approx p^{\alpha}$, with

$\alpha = -0.55 \pm 0.05$ (95% confidence interval).

In the Zimm model,[139] the modes are sinusoids, like the vibrations of a violin string, with a characteristic wavevector $k_p \propto p$. Zimm showed that a fluctuation with a wavevector of k has a relaxation time $\tau \propto k^{-3/2}$. What is the relation between the $p^{-1/2}$ scaling I measured and the $p^{-3/2}$ scaling predicted by Zimm?

The PC modes represents the vibrations of a 3-D spherically symmetric elastic continuum. In k-space, the number of modes with wavevector between k and $k + dk$ is $\sim k^2 dk$, and so the p^{th} mode will have a wavevector $k_p \propto p^{1/3}$. The relation $\tau \propto k^{-3/2}$ still applies, whence $\tau_p \propto p^{-1/2}$.

Thus the essential difference between the Zimm model and the PC model is that the Zimm model deals with the vibrations of a 1-D string, while the PC model deals with the vibrations of a 3-D elastic continuum.

3.4.3 Nonlinear dynamics

Now we quantify nonlinear interactions between the modes. The approach is to fit a linear model to the dynamics, and then to look for higher-order correlations among the residuals. If the time-evolution of the system were linear and Markovian (as required by both the Rouse and Zimm models), then the vector of amplitudes in each eigenstate would evolve according to a Langevin equation:

$$\mathbf{a}[k+1] = \mathbf{M}\mathbf{a}[k] + \xi[k], \tag{3.9}$$

where $\mathbf{M}$ is a transition matrix, $\xi[k]$ is a vector of Gaussian white noise describing the effect of thermal fluctuations, and k is the frame index ($t = k\,\delta t$). We considered only the first 15 eigenvectors, and estimated the elements of $\mathbf{M}$ by a least-squares fit to the data. The time-series of the residuals $\xi[k]$ was examined for signs of nonlinear dynamics. For example, a conformation-dependent internal friction would lead to a non-zero value of the 3rd order correlation function:

$$\tilde{\rho}^{(3)}_{pq}(\tau) = \frac{\left\langle \xi_p^2(t+\tau) a_q(t) \right\rangle}{\mathrm{var}(\xi_p)\mathrm{var}(a_q)^{1/2}}. \tag{3.10}$$

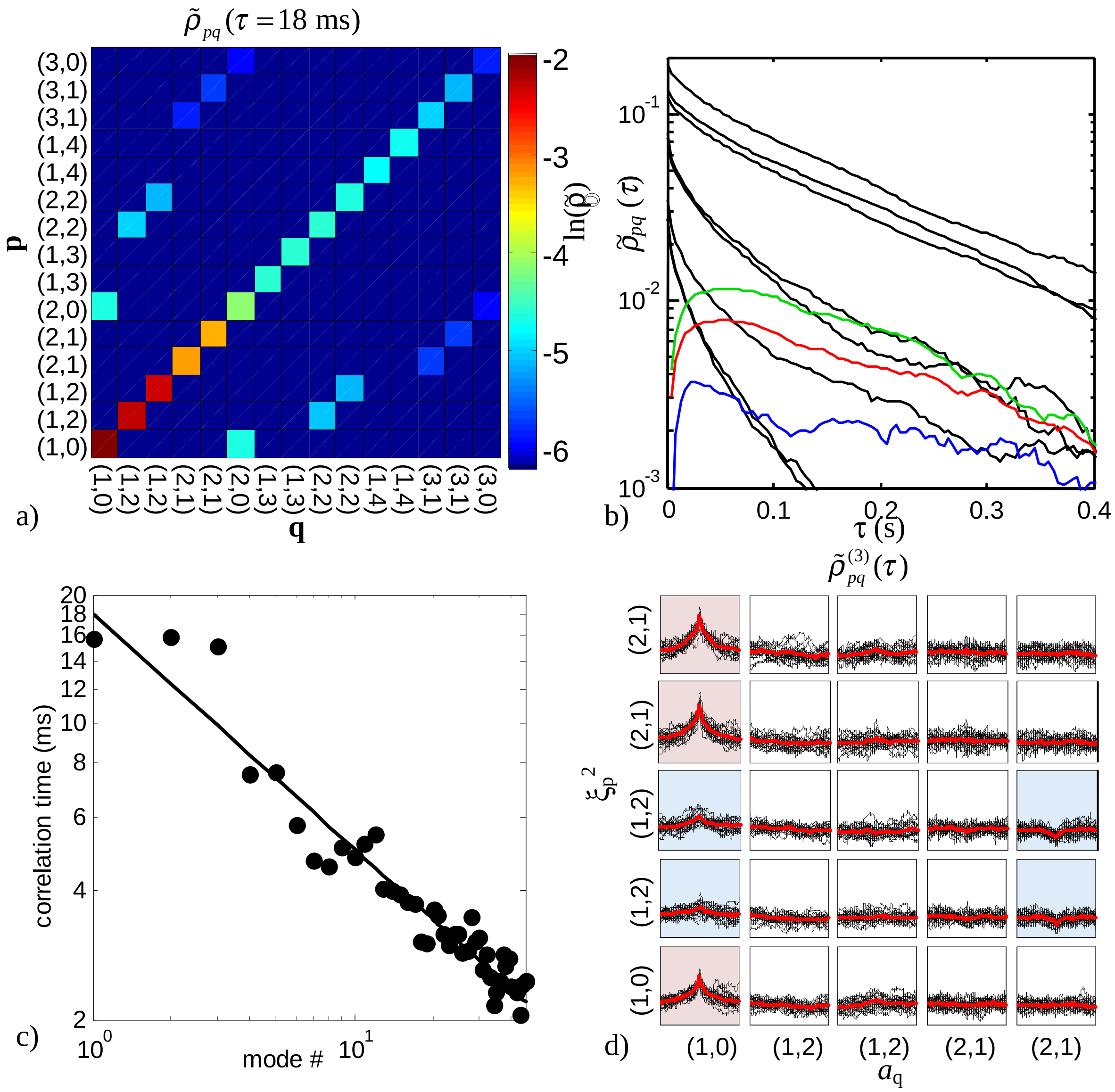

Figure 3.5: Linear and nonlinear dynamics of the principal components. a) Covariance matrix of amplitudes in the first 15 principal components at $\tau = 18$ ms. The only significant transitions conserve l (i.e. are vertical on Fig. 3.1c), and change n by ± 1. b)Time-dependence of the covariance matrix $\tilde{\rho}_{pq}(\tau)$. The eight black lines show the diagonal elements, $\tilde{\rho}_{pp}(\tau)$, for $p = 1:8$. Green: $\tilde{\rho}_{1,6}(\tau)$, red: $\tilde{\rho}_{2,9}(\tau)$, blue: $\tilde{\rho}_{4,13}(\tau)$. c) Power-law scaling of the relaxation times in the first 45 PCs. d) Nonlinear couplings in the first 5 PCs. Strong nonlinear interactions are shaded pink; weak ones blue. Each black line is the calculation for a single molecule of λ-DNA; the red lines are the ensemble average. Each box has a time axis of $\tau = (-450, 450\text{ ms})$ and a vertical axis $\tilde{\rho}^{(3)}_{pq} = (-0.1, 0.3)$.

This correlation function characterizes the effect of amplitude in mode q affecting the friction—and hence the thermal fluctuations ξ—in mode p. Fig. 3.5d shows that for several p and q, $\tilde{\rho}^{(3)}_{pq}(\tau) \neq 0$, indicating that the ansatz of Eq. 3.9 is only approximately true. Excitation in the $(1, 0)$ mode leads to the largest nonlinear effects, strongly affecting the dynamics in the mode $(1, 0)$ itself as well as the two $(2, 1)$ modes, and weakly affecting the dynamics in the two $(1, 2)$ modes. These nonzero correlations show that the intrinsic nonlinear couplings in the DNA shape dynamics are directly observable in our measurements. These effects are not predicted by the linearized Zimm model and cannot be detected by traditional scattering techniques.

3.5 Motion of the center of mass

Finally, we show that nonlinear hydrodynamic coupling also affects the motion of the center of mass. Even though each molecule we study is trapped, it is possible to learn about its center-of-mass diffusion by studying the small fluctuations about the average position. Applying the technique of pseudo-free trajectories (also known as a Wold Decomposition[21]) we used the frame-by-frame measurements of center of brightness and the applied voltages to "undo" the effects of the feedback, yielding a random walk trajectory statistically similar to the one the particle would have followed had it not been trapped (Fig. 3.6a). As expected for Brownian diffusion of the center of mass, the steps, $\Delta x(t)$, in the pseudo-free trajectories are completely uncorrelated at unequal times. Computing mean-squared displacement from the pseudo-free trajectories yields an average diffusion coefficient $D = 0.32 \pm 0.02\ \mu\text{m}^2/\text{s}$. This result is somewhat smaller than the value $0.47 \pm 0.03\ \mu\text{m}^2/\text{s}$ obtained by Smith *et al.*[112], but the difference is consistent with a modest suppression due to hydrodynamic interactions with the walls of the trap.[31]

Almost 40 years ago Dubois-Violette and De Gennes predicted that deviations from the Zimm model should appear as non-Markovian diffusion of the center of mass,[39] but surmised that this effect would be difficult to observe. This effect arises because the translational diffusion coefficient, D, depends on the instantaneous conformation: more extended conformations diffuse more slowly than more compact conformations. If one examines the diffusion on a timescale short compared to the slowest internal relaxation, the magnitudes of successive Brownian displacements should be correlated. In contrast, the Zimm model uses only the time-average conformation in calculating the diffusion coefficient, yielding statistically independent diffusive hops.

To test for non-Markovian diffusion, we examined the pseudo-free trajectories for signs of fluctuations in D, which lead to a non-zero value of the 4^{th} order correlation function:

$$C^{(4)}(\tau) = \text{corr}\left(\Delta x(t+\tau)^2, \Delta x(t)^2\right), \tag{3.11}$$

where $\Delta x(t) \equiv x(t+\delta t) - x(t)$ is the Brownian hop along the x-axis in the interval between video frames, δt (Fig. 3.6b, blue line). In the last line of the appendix of ref. [39], Dubois-Violette and de Gennes predicted that in the limit of strong internal hydrodynamic interactions, $\lim_{\tau\to 0} C^{(4)}(\tau) = 1.7\%$. Averaging $C^{(4)}(\tau)$ for the 100 ms subsequent to the $\tau = 0$ spike, we found $C^{(4)}(\tau) = 1.4\% \pm 0.4\%$ (mean ± s.d.; $n = 20$ data points), consistent with the prediction of ref. [39]. Furthermore, we compared the observed shape of $C^{(4)}(\tau)$ to what one would expect for Brownian diffusion with a time-dependent $D(t)$, where $D(t)$ was determined from the *instantaneous* value of the radius of gyration, $R_G(t)$, which was in turn extracted from the video images (solid black line in Fig. 3.6b). As Fig. 3.6 shows, this "spherical cow" approximation is in good agreement with the data, validating the hypothesis that the fluctuations in D arise from internal conformational fluctuations. The long time trajectories enabled by the ABEL trap allow probing of conformational fluctuations of a trapped molecule with high precision, solely through their effect on the Brownian motion of the center of mass.

We have shown that active trapping of single molecules of DNA in the ABEL trap provides rich dynamical information about transport properties as well as spatial conformations. The results presented here serve as a benchmark against which to test analytical theories and numerical simulations of polymer dynamics. Several quantities await theoretical explanation: the shapes of the principal components (Fig. 3.1b); the

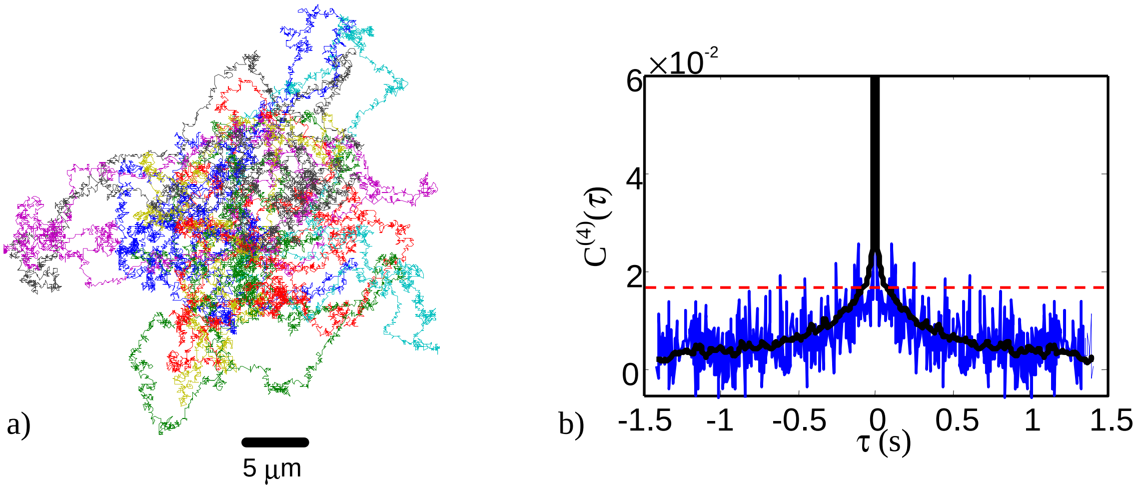

Figure 3.6: Non-Markovian diffusion of the center of mass of λ-DNA. a) Reconstructed pseudo-free trajectories of some of the DNA molecules studied, shown in different colors. The individual steps of these trajectories were analyzed for signatures of non-Markovian diffusion. b) Finite autocorrelation of the squared step-size (blue) indicates a fluctuating diffusion coefficient. The solid black line is the result one would expect if the DNA were approximated by a sphere of fluctuating radius, where the radius $R_G(t)$ is extracted from the images. The dashed red line shows the estimate from ref. [39] of 1.7% for the limit $\tau \to 0$.

regularity of the associated eigenvalues (Fig. 3.1c); the selection rules for conformational transitions (Fig. 3.5a); and the pattern of nonlinear coupling between modes (Fig. 3.5d). It will be interesting to see how the descriptive statistics presented here change when a trapped molecule of DNA is subjected to physical and chemical perturbations, such as changes in pH, temperature, ionic strength, or the addition of proteins that interact with DNA. One may also use more complex labelling schemes, such as labelling the ends of the polymer with a different color from the center. We hope that our experiments on DNA will spur efforts toward a better understanding of the role of hydrodynamic interactions in biomolecular processes.

3.6 Appendix: supplementary calculations on DNA

Below we give algorithms for analyzing and interpreting DNA conformational fluctuations. Throughout, we index quantities both by their time of measurement, t, and their measurement number, k.

3.6.1 Image acquistion and pre-processing

The ABEL trap cell was placed on an inverted optical microscope (TE300, Nikon), and epifluorescence images were acquired using an oil-immersion objective with a numerical aperture of 1.3. The video images were formatted for data analysis as follows. Each frame was 32 x 32 pixels, with a pixel width corresponding to 118 nm in the sample plane. The small image size was chosen to allow a fast frame-rate on the EMCCD camera (Cascade 512B, Roper Scientific). A background image (acquired under identical conditions to the data, except with no DNA in the field of view) was subtracted from each frame. In a small fraction of the frames ($\sim 5\%$) a second DNA molecule was seen floating through the field of view. In these frames, the pixels affected by the second molecule were manually set to the background level. When the images were shifted to align the center of mass between frames, shifts by a fraction of a pixel were accomplished with a bicubic interpolation. The total intensity of each frame was normalized to account for the slow rate of photobleaching of the YOYO-1 during the trapping period. For the present analysis, the data from all 21 molecules was aggregated, except for the third-order correlation functions in Figure 3.5d.

3.6.2 Calculation of the linear and nonlinear dynamics

In both the Rouse and Zimm models, one expects the vector of amplitudes $\mathbf{a}[k]$ in the principal components to evolve linearly subject to a transition matrix $\mathbf{M}$ and white noise ξ according to Eq. 3.9. The challenge is to extract a best-fit $\mathbf{M}$ from the record of $\mathbf{a}[k]$, and then to determine whether Eq. 3.9 adequately describes the dynamics. Multiplying Eq. 3.9 on the right by $\mathbf{a}^{\mathrm{T}}[h]$ (with $h < k$) and taking a time average yields

$$\tilde{\rho}[k-h+1] = \mathbf{M}\tilde{\rho}[k-h], \tag{3.12}$$

i.e. the covariance matrix of the vector $\mathbf{a}$ evolves deterministically under $\mathbf{M}$, and so in principle $\mathbf{M}$ can be extracted from any pair of samples of $\tilde{\rho}$. In practice,$\tilde{\rho}[0]$ is contaminated by measurement noise, so we calculated $\mathbf{M}$ from $\mathbf{M} = \tilde{\rho}[2]\tilde{\rho}^{-1}[1]$. To verify the stability of the matrix inversion, we calculated the condition number of the first $j \times j$ sub-matrices of $\tilde{\rho}[1]$, for j between 1 and 25. Fig. 3.7 shows that the matrix has small condition number for $j < 15$. The Brownian contributions to $\mathbf{a}$ are obtained from $\xi[k] = \mathbf{a}[k+1] - \mathbf{M}\mathbf{a}[k]$. To check the validity of the estimate of ξ we first calculated the linear, time-dependent correlation

$$\frac{\langle \xi_p(t+\tau) a_q(t) \rangle}{\mathrm{var}(\xi_p)^{1/2}\mathrm{var}(a_q)^{1/2}}. \tag{3.13}$$

This second-order correlation differs from Eq. 3.10 because $\xi_p(t)$ is not squared in Eq. 3.13). Only the diagonal terms of Eq. 3.13 are nonzero, as shown in Fig. 3.8. The unusual time-dependence of the diagonal elements can be understood from a scalar analogue of Eq. 3.9 with noisy observations. The governing equations are:

$$\begin{aligned} a[k+1] &= Ma[k] + \xi[k] && (3.14) \\ b[k] &= a[k] + \chi[k], && (3.15) \end{aligned}$$

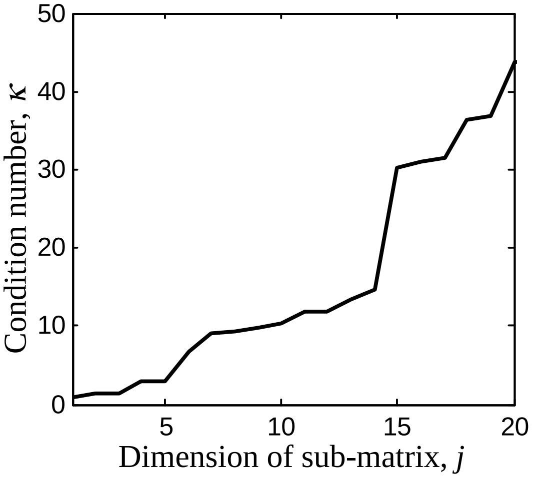

Figure 3.7: Condition number of the first $j \times j$ sub-matrices of the covariance matrix at lag $= 1$. For $j < 15$, the sub-matrix is well-conditioned, validating the procedure used for calculating the transition matrix, $\mathbf{M}$.

where $b[k]$ is the observed variable and χ is independent identically distributed Gaussian measurement noise (Eq. 1.37 is a special case with $M = 1$). After subtracting off the linear dynamics, the residuals are:

$$\begin{aligned} q[k] &\equiv b[k+1] - Mb[k] \\ &= \xi[k] + \chi[k+1] - M\chi[k]. \end{aligned} \tag{3.16}$$

Apart from a constant factor, our estimate of the diagonal elements of Eq. 3.13 in this scalar analogue is given by $\langle q[k+h]b[k]\rangle$. Several special cases need to be considered to calculate this quantity.

a) $h = 0$

$$\begin{aligned} \langle q[k]b[k]\rangle &= \langle(\xi[k] + \chi[k+1] - M\chi[k])(a[k] + \chi[k])\rangle \\ &= -M\left\langle\chi^2\right\rangle; \end{aligned} \tag{3.17}$$

b) $h = -1$

$$\begin{aligned} \langle q[k-1]b[k] \rangle &= \langle (\xi[k-1] + \chi[k] - M\chi[k-1])(Ma[k-1] + \xi[k-1] + \chi[k]) \rangle \\ &= \left\langle \chi^2 \right\rangle + \left\langle \xi^2 \right\rangle ; \end{aligned} \tag{3.18}$$

c) $h \leq -2$

$$\langle q[k+h]b[k] \rangle = M^{h-1} \left\langle \xi^2 \right\rangle \tag{3.19}$$

d) $h \geq 1$

$$\langle q[k+h]b[k] \rangle = 0. \tag{3.20}$$

The four regimes embodied in Eqs. 3.17-3.20 are clearly seen in Fig. 3.8. The correlation grows exponentially at negative times, jumps positive at $h = -1$, jumps negative at $h = 0$, and is zero for positive times.

Importantly, there is no indication from Fig. 3.8 that anything unusual is going on in the off-diagonal elements. Only when ξ_p is squared do the nonlinear couplings appear. The overall sign of each column of $\tilde{\rho}^{(3)}$ is arbitrary because the sign of each component of **a** is arbitrary.

3.6.3 Pseudo-free trajectories

Pseudo-free trajectories for trapped DNA molecules were calculated as outlined in section 1.7. Fig. 3.9 shows the autocorrelation functions of the measured x-displacements and of the reconstructed pseudo-free trajectory. The negative autocorrelation in the pseudo-free displacements at lag = 1 is due to measurement noise as explained in section 1.5.2.

3.6.4 Fluctuating transport coefficients

In section 1.7.1 I showed that fluctuations in the mobility show up in the autocovariance of the steps of the pseudo-free trajectory. Fig. 3.9 shows that in our data the autocovariance is a delta-function, except for the already-explained bounce at lag = 1. Thus we detect no fluctuations in the electrokinetic mobility of λ-DNA.

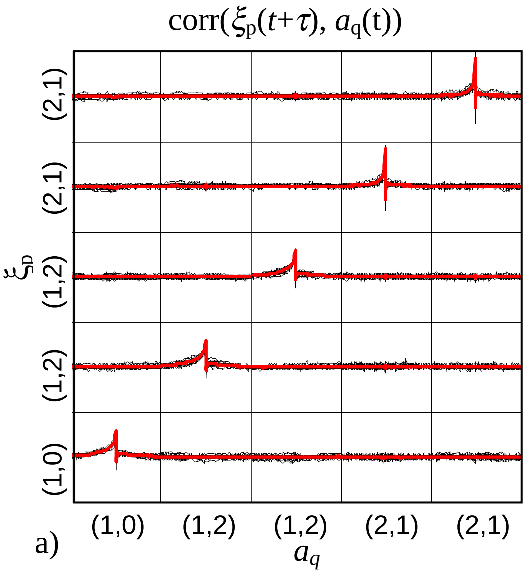

corr(ξ_p^2, a_q)

(2, 1)	0.19	0.004	0.021	0.018	-0.004
(2, 1)	0.19	-0.006	0.020	0.014	-0.009
(1, 2)	0.065	0.010	-0.021	-0.011	-0.043
(1, 2)	0.049	-0.007	0.003	-0.016	-0.039
(1, 0)	0.14	-0.002	0.027	-0.007	-0.000
ξ_p^2 \ a_q	**(1, 0)**	**(1, 2)**	**(1, 2)**	**(2, 1)**	**(2, 1)**

b)

Figure 3.8: Statistical properties of the residuals after fitting to the linear model of Eq. 3.9. a) Cross-correlation of the Brownian displacements and the measured mode amplitudes in the first 5 eigenstates (Eq. 3.13). The black lines show the calculation for individual molecules of DNA and the red lines are the average. The unusual time-dependence of the diagonal elements is explained by a model of a linear autoregressive process with measurement noise. Each box has a time axis of $\tau = (-450, 450)$ ms, and a vertical axis of $(-0.6, 0.6)$. b) Table of numerical values at $\tau = 0$ of the third-order cross-correlation $\tilde{\rho}^{(3)}(\tau)$. Statistical errors on all elements are approximately ±0.006. These are the peak-heights of the plot in Fig. 3.5d.

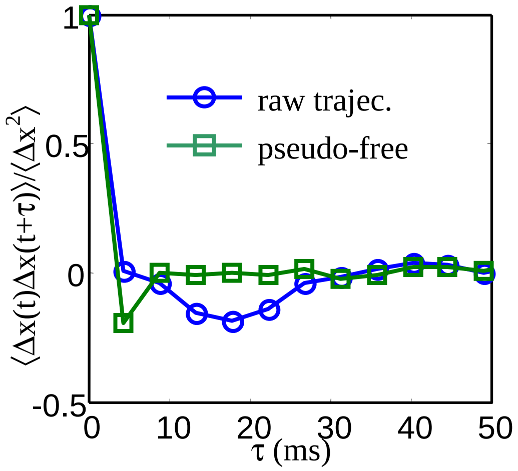

Figure 3.9: Two-time autocorrelation of the displacements in the measured and pseudo-free trajectories. The slow overshoot in the measured trajectories is due to the finite response time of the feedback: at the settings used in this experiment, the feedback was slightly underdamped. Calculating the pseudo-free trajectory undoes the effects of the feedback. The slight overshoot at the shortest nonzero lag ($\tau = 4.5$ ms) is due to errors in the estimate of the position of the particle.

Now we consider a fluctuating diffusion coefficient, which leads to fluctuations in the variance Δx^2 of the Brownian steps as discussed in Section 1.7.1. The 4^{th} order correlation, $C^{(4)}[k]$, of the pseudo-free steps is plotted in Fig. 3.6b. First we describe the “spherical cow” model (blue line in Fig. 3.6b), which models the diffusion as a sphere with fluctuating radius $R_G[k]$. The 2-D radius of gyration, $R_G[k]$, at video frame k, is:

$$R_G[k] = \left(\sum_i (\mathbf{r}_i - \mathbf{r}_{CM})^2 S_i[k] \right)^{1/2}, \tag{3.21}$$

where the index i runs over all pixels in the image, $\mathbf{r}_i$ is the position of pixel i, $\mathbf{r}_{CM}$ is the position of the center of mass, and S_i is the intensity at pixel i (recall that the images are normalized so $\sum_i S_i[k] = 1$).

In the Zimm model, the translational diffusion coefficient is:

$$D = 0.196 \frac{k_B T}{\sqrt{6}\pi\eta R_G} \tag{3.22}$$

where η is the viscosity of the medium (compare to Eq. 1.2 for the diffusion coefficient of a sphere). We calculated a time-dependent diffusion coefficient, $D[k]$, by substituting $R_G[k]$ of Eq. 3.21 for R_G in Eq. 3.22.

The 1-D diffusion of a particle with changing radius, sampled at discrete intervals δt, obeys:

$$x[k+1] = x[k] + \sqrt{2D[k]\delta t}N(0,1), \tag{3.23}$$

where $N(0,1)$ is Gaussian white noise with mean 0 and variance 1. Multiplication of the simulated trajectory by a constant factor does not affect the value of $C^{(4)}[k]$. Thus we simulated trajectories according to the rule:

$$x[k+1] = x[k] + N(0,1)/\sqrt{R_G[k]}, \tag{3.24}$$

which uses the instantaneous radius of gyration to set the diffusion coefficient and hence the next displacement at each time step. From the simulated trajectories we extracted $C^{(4)}[k]$ in the same manner as for the pseudo-free trajectories. We simulated 1000 trajectories, each of length 58,421 (the same length as the data). This approach avoids the problem of performing a full simulation of the polymer dynamics, which would have required us to assume a model for the internal dynamics. It is remarkable that this very crude approximation is in such good agreement with the data.

It is also possible to calculate $C^{(4)}[k]$ directly from the time-varying radius of gyration. Inserting the displacements of Eq. 3.24 into Eq. 1.67 and assuming the fluctuations in R_G are small, yields:

$$C^{(4)}[k] = \frac{\mathrm{cov}(R_G[k+h], R_G[k])}{2\left\langle R_G\right\rangle^2}, \tag{3.25}$$

i.e. $C^{(4)}[k]$ is a direct probe of the conformational fluctuations. The value of $\lim_{k\to 0} C^{(4)}[k]$ can be estimated from a random walk model of the polymer conformation, without making assumptions about the internal dynamics. We simulated 10^6 polymer conformations, where each conformation was a Gaussian 3-D random walk of $N = 100$ steps, and then extracted R_G from each conformation. From Eq. 3.25 we obtained

$\lim_{k\to 0} C^{(4)}[k] \approx 0.0278$. This result is independent of N for $N > 50$ and is somewhat larger than our experimental result, implying that the molecule exists in between the non-draining and freely draining limits. Based on a calculation using only the dominant conformational mode, Dubois-Violette and de Gennes estimated $\lim_{k\to 0} C^{(4)}[k] \approx 0.017$.

3.6.5 Relation to scattering experiments

Dynamic light scattering (DLS) and neutron scattering indirectly probe polymer conformations by diffracting particles (photons or neutrons) off polymers in solution. The fundamental quantity measured by scattering techniques is the dynamic structure factor. For coherent scattering it is given by:

$$G(\mathbf{q},\tau) = |F(\mathbf{q})|^2 \sum_{\alpha,\beta} \langle \exp\left[i\mathbf{q}\cdot(\mathbf{r}_\alpha(\tau) - \mathbf{r}_\beta(0))\right]\rangle , \tag{3.26}$$

where the brackets indicate an ensemble average, $\mathbf{q}$ is the scattering vector, and α and β denote individual chain elements. The quantity $F(\mathbf{q})$ is the form factor for an individual chain element and is typically replaced by $F(0)$. On timescales much shorter than the slowest internal relaxation, $\mathbf{r}_\alpha(\tau) - \mathbf{r}_\beta(0)$ is Gaussian distributed, so Eq. 3.26 becomes:

$$G(\mathbf{q},\tau) \sim \sum_{\alpha,\beta} \exp\left[-\frac{1}{2}q^2 \left\langle (\mathbf{r}_\alpha(\tau) - \mathbf{r}_\beta(0))^2\right\rangle\right]. \tag{3.27}$$

De Gennes found that $G(\mathbf{q},\tau) \sim \exp[-(\tau/\tau_0)^{1/2}]$ for the Rouse model and Dubois-Violette and de Gennes found $G(\mathbf{q},\tau) \sim \exp[-(\tau/\tau_0)^{2/3}]$ for the Zimm model. For a nice review of light scattering from DNA, see [62].

In the case of a real-space imaging, as in the ABEL trap, each bead on the polymer contributes a roughly Gaussian point spread function (PSF) in the image plain. Thus the total intensity distribution is:

$$S(\mathbf{r},t) = \frac{1}{2\pi N\sigma^2} \sum_{\alpha} \exp\left[-\frac{1}{2\sigma^2}\left(\mathbf{r}_\alpha(t) - \mathbf{r}\right)^2\right], \tag{3.28}$$

where σ is the width of the PSF and N is the total number of elements in the chain. The normalization is chosen so $\int d^2\mathbf{r}S(\mathbf{r}) = 1$. Then the image-image correlation function is

$$\begin{aligned} C(\tau) &= \int d^2\mathbf{r}\,\langle S(\mathbf{r},\tau)S(\mathbf{r},0)\rangle \\ &= \frac{1}{(2\pi N\sigma^2)^2}\int d^2\mathbf{r}\sum_{\alpha,\beta}\left\langle \exp\left[-\frac{1}{2\sigma^2}\left(\mathbf{r}_\alpha(\tau)-\mathbf{r}\right)^2-\frac{1}{2\sigma^2}\left(\mathbf{r}_\beta(0)-\mathbf{r}\right)^2\right]\right\rangle \\ &= \frac{1}{4\pi N^2\sigma^2}\sum_{\alpha,\beta}\left\langle \exp\left[-\frac{1}{4\sigma^2}\left(\mathbf{r}_\alpha(\tau)-\mathbf{r}_\beta(0)\right)^2\right]\right\rangle. \end{aligned} \tag{3.29}$$

Eqs. 3.29 and 3.27 are similar, except that the average is taken inside the exponential in Eq. 3.27 and outside the exponential in Eq. 3.29.

The displacement $\mathbf{r}_\alpha(\tau) - \mathbf{r}_\beta(0)$ is the sum of many small independent thermal kicks, and thus is expected to have a Gaussian distribution with width $\sigma_{\alpha,\beta}(\tau)$. The average in Eq. 3.29 can then be evaluated explicitly, to yield:

$$C(\tau) = \sum_{\alpha,\beta}\frac{2}{2+\sigma^2_{\alpha,\beta}(\tau)/\sigma^2}. \tag{3.30}$$

At this point the situation looks grim—there does not seem to be a clear relation between the image-image correlation function and the DLS structure factor. However, a slightly different approach makes this relationship apparent. Suppose that instead of assuming a Gaussian PSF, we assumed a δ-function PSF. Then Eq. 3.28 becomes

$$S(\mathbf{r},t) = \sum_\alpha \delta^2(\mathbf{r}_\alpha(t)-\mathbf{r}). \tag{3.31}$$

Inserting the Fourier decomposition of the δ-function,

$$\delta^2(\mathbf{x}) = \int d^2\mathbf{q}\; e^{-2\pi i\mathbf{q}\cdot\mathbf{x}}, \tag{3.32}$$

the image-image correlation function becomes

$$\begin{aligned} C(\tau) &= \sum_{\alpha,\beta} \int\int d^2\mathbf{q}\, d^2\mathbf{q}' \int d^2\mathbf{r}\ \langle \exp\left[-2\pi i \mathbf{q}\cdot(\mathbf{r}_\alpha(\tau)-\mathbf{r}) - 2\pi i \mathbf{q}'\cdot(\mathbf{r}_\beta(0)-\mathbf{r})\right]\rangle \\ &= \sum_{\alpha,\beta} \int d^2\mathbf{q}\, \langle \exp\left[-2\pi i \mathbf{q}\cdot(\mathbf{r}_\alpha(\tau)-\mathbf{r}_\beta(0))\right]\rangle \\ &= \int d^2\mathbf{q}\ G(\mathbf{q},\tau). \end{aligned} \tag{3.33}$$

In going from the first to the second line of Eq. 3.33 I evaluated the integral over $\mathbf{r}$, which led to a factor of $\delta^2(\mathbf{q}-\mathbf{q}')$. The δ-function then killed the integral over $\mathbf{q}'$. From Eq. 3.33 we see that the time-dependence of the image-image correlation function is expected to be the same as that of the dynamic structure factor, obeying a stretched exponential with an exponent of $-1/2$ in the Rouse model $-2/3$ in the Zimm model.

Chapter 4

The shape of a random walk

Random walks are widely applied to model processes in biology, chemistry, physics, and finance.[29] Here we analyze the shape of a random walk in 1, 2, and 3 dimensions. We apply Principal Components Analysis (PCA) to identify the characteristic long wavelength shape fluctuations. These principal components form an efficient basis with which to describe the shape of a random walk. This theoretical work was inspired by experiments on trapped molecules of λ-DNA, and can safely be skipped by readers interested only in data and instrumentation.

4.1 Introduction

There are many ways to analyze the shape of a random walk. The central limit theorem requires that the endpoint follows a Gaussian distribution relative to the starting point. Since any two internal points can be thought of as the start and end of a shorter random walk (recall that the "free" ends do not affect what happens in the interior segment), the vector connecting any two internal points is also Gaussian distributed. One can also consider the distribution of the greatest excursion of a random walk (extreme value statistics), or the distribution of the length of random walk required to attain an excursion of a certain value (mean first passage time).

All of the above measures relate to the relative positions of only two points on the walk. Are there ways to obtain a more "global" measure of the shape? One common approach is to fit a d-dimensional random walk to a d-dimensional ellipsoid. For a random walk of N steps, the radius of gyration tensor is given by:

$$T_{ij} = \frac{1}{N}\sum_{n=1}^{N}[x_i(n) - \langle x_i\rangle][x_j(n) - \langle x_j\rangle], \tag{4.1}$$

where $i, j \in (1, \ldots, d)$ are the indices of the Cartesian directions. The center of mass along dimension i is

$$\langle x_i\rangle = \frac{1}{N}\sum_{n=1}^{N} x_i(n). \tag{4.2}$$

The eigenvectors of $\boldsymbol{T}$ are the principal axes of the random walk, and the eigenvalues are the mean-square extent along those axes. One finds, for instance, that random walks in 3 dimensions are surprisingly anisotropic [126], with

$$\left\langle R_1^2\right\rangle : \left\langle R_2^2\right\rangle : \left\langle R_3^2\right\rangle = 11.80 : 2.69 : 1.00, \tag{4.3}$$

where the principal radii have been ordered by size and averaged over many walks. A nice review of the principal radii of random walks is given in [103].

Random walks are not ellipsoids. Is there a way to describe the shape and internal structure of a random walk that doesn't involve fitting the walk to some arbitrarily selected geometry? Principal Components Analysis (PCA) provides a systematic expansion procedure for describing the shape of a random walk at varying levels of detail, and with no prior assumptions about its shape.

4.1.1 Lagrangian vs. Eulerian approaches to PCA

In Eulerian fluid dynamics, one calculates fluid properties (e.g. pressure, velocity, shear) as a function of position in some fixed reference frame. The Lagrangian approach follows the trajectories of distinct fluid elements (one can imagine tracer particles) as a function of time. The Eulerian approach leads to the well-known Navier-Stokes equations, and is generally preferred due to its simplicity. The Eulerian approach takes advantage of a symmetry of the fluid: that all elements of the fluid are identical, so there is no need to follow a *particular* fluid element. [104]

A similar situation prevails when one wishes to perform PCA on a random walk. One can follow the trajectory $x_i(t)$ of mass element i, and calculate correlation functions such as $C_{ij}(\tau) = \langle x_i(t)x_j(t+\tau)\rangle$. This approach is necessary when considering a multi-component system such as a protein, where two elements i and j may not be interchangeable (e.g. they have different chemical properties). For a homogeneous system, however, one can adopt a reduced description, where one only considers the density $\rho(x)$. Then one can calculate correlation functions such as $C_{xy}(\tau) = \langle \rho(x,t)\rho(y,t+\tau)\rangle$. For determining many dynamical properties of polymers, this information is sufficient. The standard Rouse and Zimm models of polymer dynamics are developed in the Lagrangian language (following every mass element), but we suggest here that an Eulerian approach might be more effective.

Starting with the pioneering work of Karplus [67] PCA has been widely applied to analyze molecular dynamics trajectories. The idea is to reduce the motion of a protein in $3N$-dimensional space, where N is the number of atoms in the system, to motion in m-dimensional space ($m \ll 3N$), where each of the m dimensions describes motion along some collective coordinate. Such an approach is productive because the secondary structure of proteins is fairly rigid, so many motions involve entire domains. The principal components are an efficient basis in the sense that if the fluctuations of the system are Gaussian, then for a given m, projection of the dynamics onto the principal components accounts for a larger fraction of the total variance than would a projection onto any other basis with m elements. For a review of PCA of proteins, see [55].

4.2 Random walk in the Lagrangian perspective

First we consider the principal components of a 1-D random walk, starting at the origin. The covariance matrix and its eigenfunctions can be calculated explicitly.

Consider a random walk of N steps:

$$\begin{aligned} x(0) &= 0 \\ x(n+1) &= x(n) + \xi(n) \end{aligned} \tag{4.4}$$

where $\xi(n)$ is Gaussian white noise with unit variance. If one averages over many walks, it is clear that $\langle x(n) \rangle = 0$.

We wish to calculate the covariance matrix

$$C(n,m) = \langle x(n)x(m) \rangle_{.} \tag{4.5}$$

Suppose $n < m$. Due to the Markov property of random walks, the point $x(n)$ can be considered the origin for a shorter random walk that contains $x(m)$. Clearly, $x(m)$ will be on average symmetrically distributed around $x(n)$. Thus for $n < m$ $\langle x(n)x(m) \rangle = \langle x(n)^2 \rangle$. But for a random walk the mean-square displacement of the n^{th} step is simply n. Thus the covariance matrix takes the simple form:

$$C(n,m) = \min(n,m). \tag{4.6}$$

To calculate the eigenfunctions, we consider n and m to be continuous variables and require

$$\int_0^N C(n,m) f(m)\, dm = \lambda f(n). \tag{4.7}$$

Eq. 4.7 is solved by breaking the l.h.s. into two parts:

$$\int_0^n m f(m)\, dm + \int_n^N n f(m)\, dm, \tag{4.8}$$

and then differentiating twice with respect to n, to obtain

$$\lambda \frac{d^2 f}{dn^2} = -f. \tag{4.9}$$

The allowed values of λ are determined by the conditions that 1) the eigenvectors be

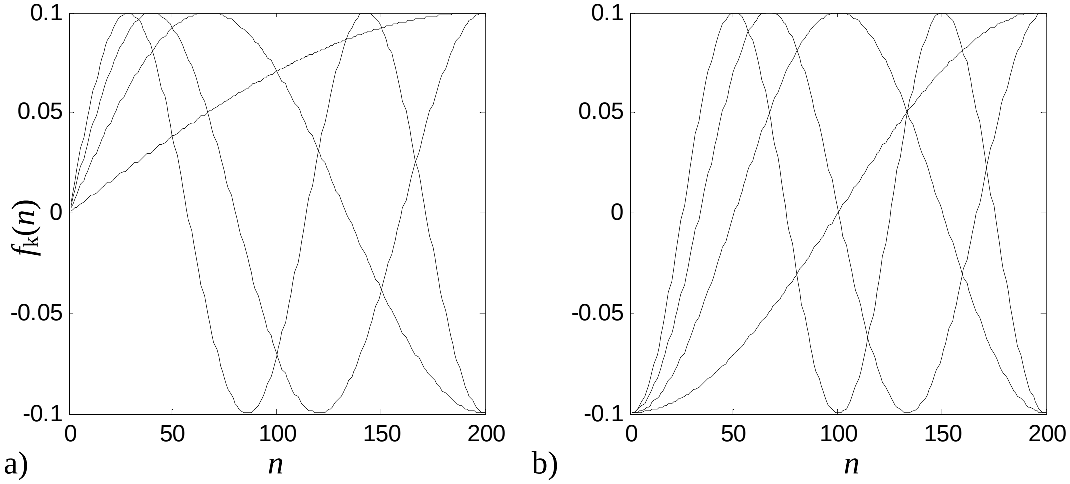

Figure 4.1: Principal components of a 1-D random walk in the Lagrangian perspective, a) with one end fixed and b) with the center of mass fixed. These principal components are precisely the Rouse modes of a 1-D polymer chain.

orthonormal, and 2) $f_k(0) = 0$ for all k. Thus

$$f_k(n) = \sqrt{\frac{2}{N}} \sin\left(\frac{2\pi n(k + \frac{1}{4})}{N}\right), \tag{4.10}$$

$(k = 0, 1, \ldots)$ and

$$\lambda_k = \left(\frac{N}{2\pi(k + \frac{1}{4})}\right)^2. \tag{4.11}$$

Fig. 4.1a shows the first few principal components of a 1-D random walk of 200 steps.

The principal components can also be found for random walks with both ends free, and the center of mass fixed. Again consider an ensemble of random walks generated according to Eq. 4.4, but now calculate

$$C^{CM}(m, n) = \left\langle (x(n) - x^{CM})(x(m) - x^{CM}) \right\rangle \tag{4.12}$$

where

$$x^{CM} = \frac{1}{N} \int_0^N x(n)\, dn. \tag{4.13}$$

Eq. 4.12 expands to

$$C^{CM}(m,n) = \langle x(n)x(m)\rangle - \left\langle x(n)x^{CM}\right\rangle - \left\langle x(m)x^{CM}\right\rangle + \left\langle (x^{CM})^2\right\rangle . \tag{4.14}$$

The first term on the r.h.s. is just $\min(n,m)$ as before. The second term becomes

$$\begin{aligned} \left\langle x(n)x^{CM}\right\rangle &= \frac{1}{N}\int_0^N \langle x(n)x(m)\rangle \, dm \\ &= \frac{1}{N}\int_0^N \min(n,m)\, dm \\ &= n - \frac{n^2}{2N}, \end{aligned} \tag{4.15}$$

and similarly for the third term. The fourth term is well known to be

$$\left\langle (x^{CM})^2\right\rangle = N/3. \tag{4.16}$$

Making the above substitutions in Eq. 4.12, and then applying Eq. 4.7, yields

$$\lambda \frac{d^2 f(n)}{dn^2} = -f(n) + \frac{1}{N}\int_0^N f(m)\, dm. \tag{4.17}$$

This equation is solved by

$$f_k(n) = \sqrt{\frac{2}{N}}\cos\left(\frac{\pi n k}{N}\right) \tag{4.18}$$

with eigenvalues

$$\lambda_k = \left(\frac{N}{\pi k}\right)^2 \tag{4.19}$$

and $k = 1, 2, \ldots$. The principal components that we have just found are precisely the normal modes of the Rouse model of polymer dynamics. [102]

The procedure outlined here generalizes trivially to higher dimensions because the components along different dimensions are statistically independent. Thus in d dimensions each normal mode is d-fold degenerate.

4.3 Random walk in the Eulerian perspective

Often in experimental situations, one does not know the contour coordinate of a given piece of a random walk polymer. For instance, all pieces of the polymer might scatter radiation equally. Then it is more natural to think of the polymer as a density distribution $\rho(\mathbf{r})$. We will now analyze random walks from this perspective, first considering one end fixed, and then considering the center of mass fixed.

4.3.1 Mean distribution, end fixed

Consider a random walk starting at the origin. The piece of the walk at step number α has a density distribution

$$P_\alpha(x) = \frac{1}{\sqrt{2\pi\alpha}} \exp\left[-\frac{x^2}{2\alpha}\right]. \tag{4.20}$$

The total density distribution is the sum of the distributions for each piece of the polymer:

$$P(x) = \int_0^N d\alpha \, P_\alpha(x). \tag{4.21}$$

Here are the explicit formulas for the distribution in 1, 2, and 3 dimensions, where $\mathbf{r}$ is a 1, 2, or 3-component vector:

$$P(\mathbf{r}) = \begin{cases} \sqrt{\frac{2N}{\pi}} e^{-\frac{r^2}{2N}} - |r| \mathrm{erfc}\left(\frac{|r|}{\sqrt{2N}}\right) & \text{1-D} \\ \frac{1}{2\pi} \Gamma_0\left(\frac{r^2}{2N}\right) & \text{2-D} \\ \frac{1}{2\pi r}\left[1 - \mathrm{erf}\left(\frac{r}{\sqrt{2N}}\right)\right] & \text{3-D} \end{cases} \tag{4.22}$$

In 1-D the distribution has a cusp at $r = 0$ but is everywhere finite. In 2 and 3-D the distribution diverges at $r = 0$. With real polymers this divergence does not occur because there is a short-distance cutoff at which the polymer no longer behaves as a random walk. Nonetheless, 2-D video images of surface-tethered polymers should show a sharply peaked non-Gaussian density distribution.

4.3.2 Mean distribution, CM fixed

The density distribution about the center of mass of 1-D random walks is also not a Gaussian, although the deviation is much smaller than in the end-tethered case. Recall from Eq. 4.16 that the center of mass is located a mean square distance of $N/3$ from the ends of a 1-random walk. The distribution of one end relative to the center of mass is a Gaussian with variance $N/3$:

$$P_{\mathrm{end}}(x) = \sqrt{\frac{3}{2\pi N}} \exp\left(-\frac{3x^2}{2N}\right). \tag{4.23}$$

An internal chain element can be considered as the ends of two conjoined random walks, of lengths ϵN and $(1-\epsilon)N$, where $0 \leq \epsilon \leq 1$. The centers of mass of the two pieces are independently distributed according to Eq. 4.23, with N replaced by ϵN and $(1-\epsilon)N$, respectively. The mass of each piece of the chain is proportional to its length, so the position of the total center of mass is given by the weighted sum $x^{CM} = \epsilon x_L^{CM} + (1-\epsilon)x_R^{CM}$, where the L, R subscripts denote the two pieces of the chain. The distribution of the chain element at ϵN relative center of mass is obtained from the addition-of-errors formula as:

$$P_\epsilon(x) = \sqrt{\frac{3}{2\pi N(3\epsilon^2 - 3\epsilon + 1)}} \exp\left[-\frac{3x^2}{2N(3\epsilon^2 - 3\epsilon + 1)}\right]. \tag{4.24}$$

Since all pieces of the random walk contribute equally to the density, the total density distribution is

$$P(x) = \int_0^1 d\epsilon \sqrt{\frac{3}{2\pi N(3\epsilon^2 - 3\epsilon + 1)}} \exp\left[-\frac{3x^2}{2N(3\epsilon^2 - 3\epsilon + 1)}\right], \tag{4.25}$$

which looks qualitatively like a Gaussian near $x = 0$, but has fat tails relative to a Gaussian. Similar formulas apply in higher dimensions, with the minor modification that in d dimensions the normalization of the Gaussian of variance σ^2 is $(2\pi\sigma^2)^{d/2}$. In Section 3.2 we saw that this distribution accurately describes the average density distribution of a molecule λ-DNA held in the ABEL trap.

4.3.3 Principal components

The principal components of a random walk in the Eulerian perspective are, unfortunately, difficult to calculate analytically. I have obtained expressions for the covariance matrix, but these expression must be evaluated on a grid and then diagonalized numerically to obtain the eigenfunctions. The derivation is complicated and the expressions are huge. Rather than going down that route here, I will describe numerical simulations that yielded the same results.

Numerical simulations of random walks were performed in MATLAB. In each simulation I generated a large number of random walks in 1, 2, or 3 dimensions. Each random walk was turned into a density distribution on a grid, $\rho(x)$, either with the end-point or center of mass fixed. The density distribution was then convolved with a narrow Gaussian to represent the finite resolution of any imaging experiment and to hide artifacts from pixilation. The mean density distribution and covariance matrices were then calculated numerically. The covariance matrix of a set of images (in any dimension) is

$$C(x,y) = \langle \rho(x)\rho(y) \rangle - \langle \rho(x) \rangle \langle \rho(y) \rangle , \tag{4.26}$$

where x and y are indices that run over all pixels in the image. The covariance matrices were diagonalized.

Fig. 4.2 shows the principal components of a random walk in 1 dimension. While the principal components look qualitatively like the Hermite polynomial solutions to the 1-D quantum simple harmonic oscillator (or the diffusion equation in a parabolic potential), Fig. 4.2 shows that this similarity is only approximate. The dominant eigenfunction with the end fixed does not have a counterpart with the center of mass fixed, because this eigenfunction corresponds to translation of the center of mass. Fig. 4.3 shows the eigenvalues of the first 45 principal components of a 1-D random walk. With either the end or center of mass fixed, the eigenvalues scale like $\lambda_k \propto k^{-3/2}$, compared to the k^{-2} scaling obtained in the Lagrangian perspective. I do not know what is the relation between these two quantities.

An analysis similar to the above was performed in two and three dimensions. In two dimensions the results compared favorably with the experimental data on λ-DNA.

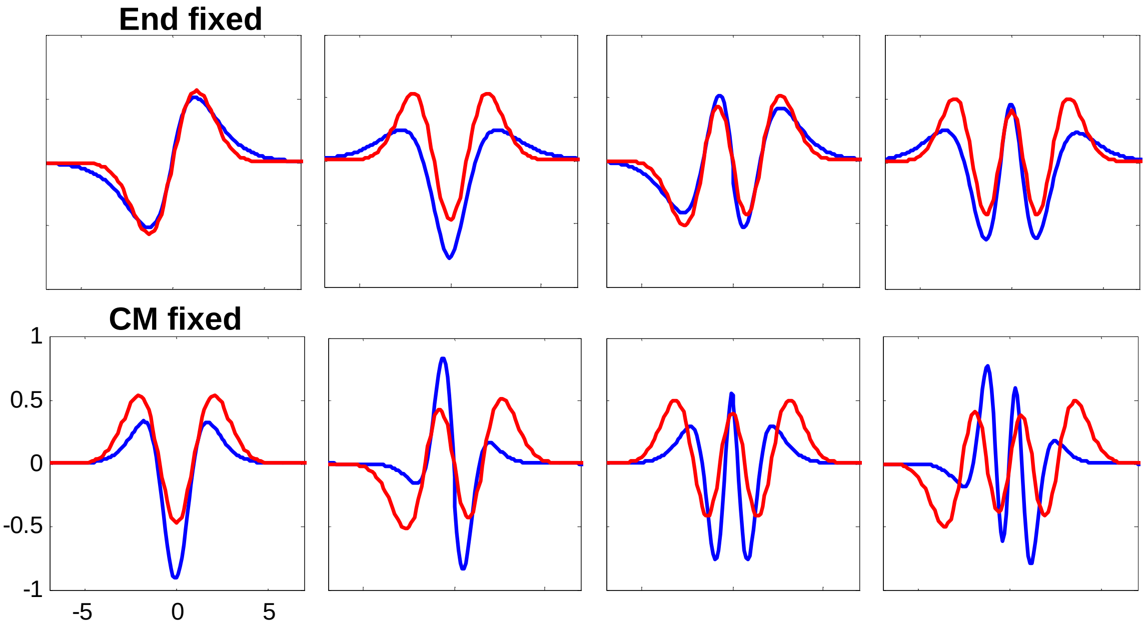

Figure 4.2: Principal components of a 1-D random walk in the Eulerian perspective (blue). The top row shows the principal components with the end of the walk fixed and the bottom row shows the components with the center of mass fixed. The red traces show the corresponding harmonic oscillator wavefunctions.

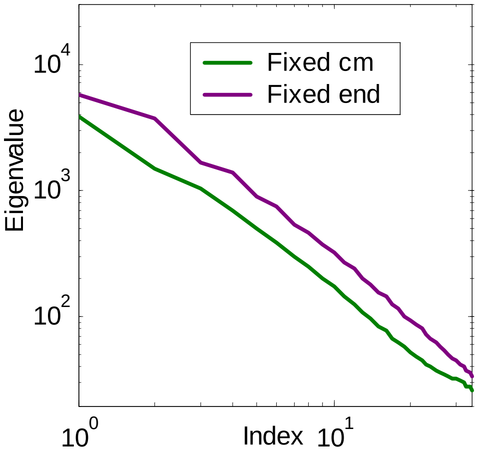

Figure 4.3: Eigenvalues of a random walk in the Eulerian perspective. The eigenvalues show power law scaling with an exponent of -3/2, different from the value -2 obtained in the Lagrangian perspective

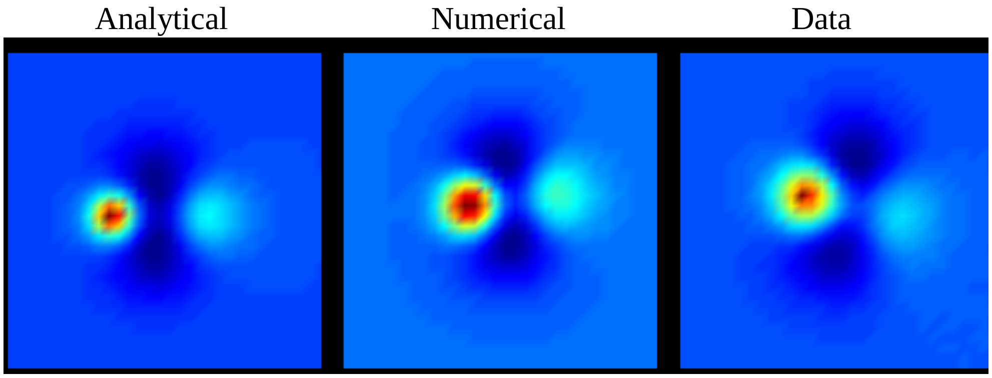

Figure 4.4: Comparison of analytical, numerical, and experimental results for the covariance matrix of a 2-dimensional random walk with the center of mass fixed. The full covariance matrix is a 4-dimensional quantity (function of two 2-D vectors), so here the first vector has been fixed to the left of the center of mass.

Fig. 4.4 shows a piece of the two-point covariance of a two dimensional random walk with the center of mass fixed. In each panel the point x was arbitrarily chosen to the left of the center of mass, and the covariance is plotted as a function of the second 2-D coordinate, y. The three panels correspond to my quasi-analytical model, a numerical simulation 10^6 2-D random walks, and image analysis of trapped molecules of λ-DNA held in the ABEL trap. The lobed structure arises from the requirement that the center of mass remain fixed: a density fluctuation on one side of the center of mass is necessarily accompanied by a density fluctuation on the opposite side. These two density fluctuations come at the expense of density above and below the center of mass.

Once we have an expression for the covariance matrix, it is a simple matter to calculate the eigenvectors numerically. Fig. 4.5 shows the result, using an analytically calculated covariance matrix, and the comparison with the experimental results on trapped λ-DNA. The experimental and theoretical eigenvectors are in good agreement, and the eigenvalues are in reasonable agreement. I do not know whether the differences between theory and experiment in the eigenvalues 2–5 are due to an experimental artefact or an oversimplification in the theory.

Finally, I performed the same analysis in 3 dimensions. This was a computationally challenging task because if each random walk is expressed as a density distribution

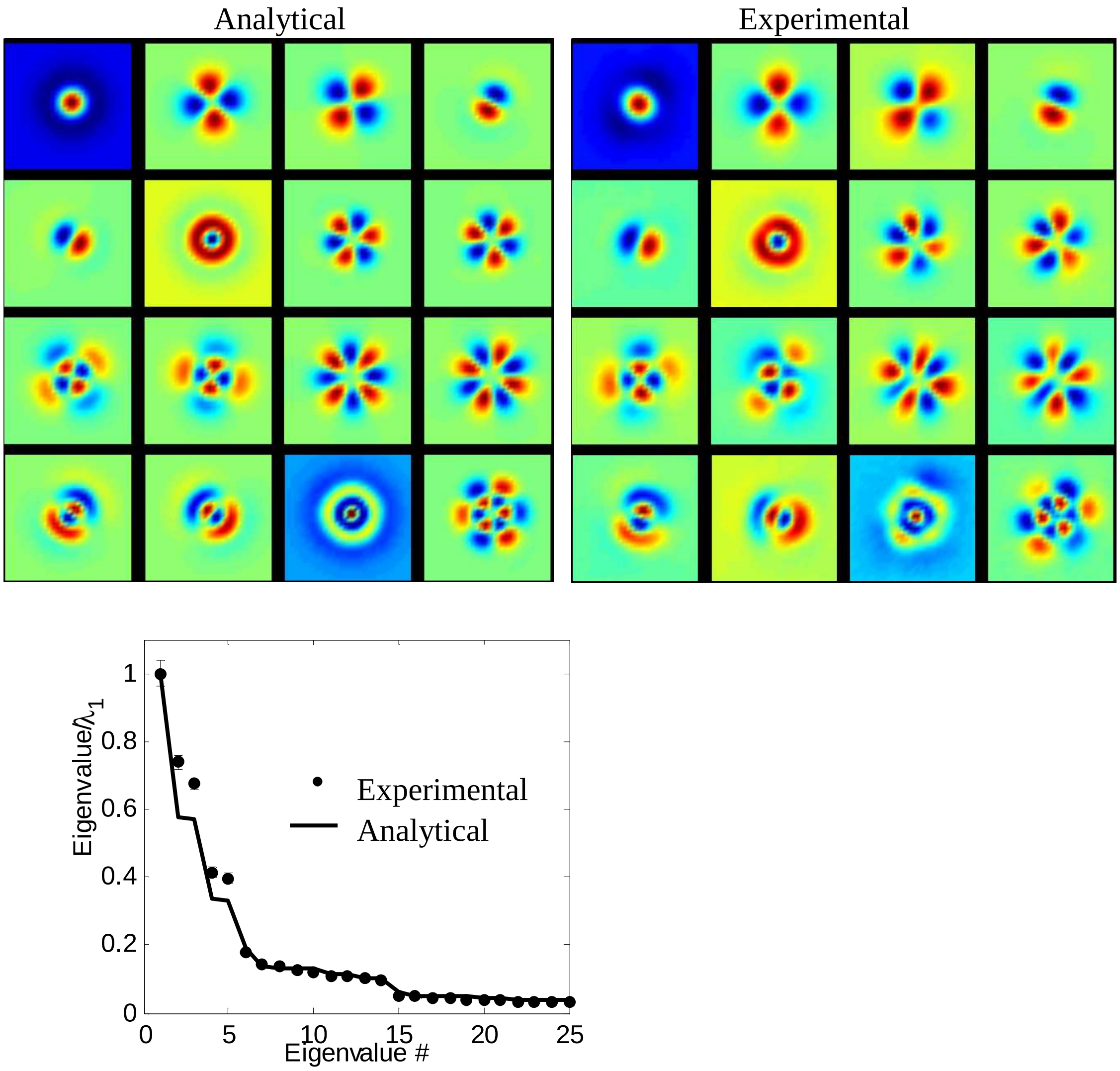

Figure 4.5: Comparison of experimental and theoretical principal components of a 2-D random walk (top) and the associated eigenvalues (bottom).

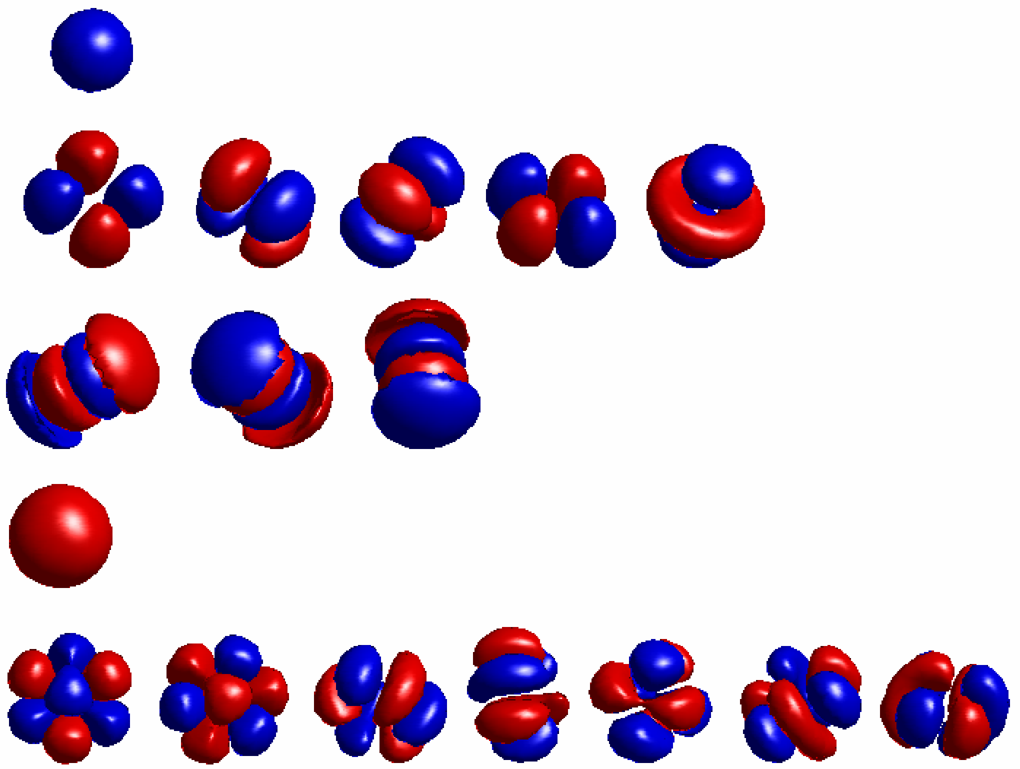

Figure 4.6: Principal components of a 3-D random walk with the center of mass fixed. These principal components form the most efficient basis in which to describe the shape of a 3-D random walk.

on a grid of side n, then the covariance matrix has dimension $n^3 \times n^3$. This matrix must then be diagonalized numerically. The largest grid I could handle had sides of length 16, corresponding to a covariance matrix with 2^{24} elements. Due to the coarseness of the grid, I do not place much faith in the eigenvalues returned by the analysis. Fig. 4.6 shows isosurfaces of the eigenvectors. These surfaces look qualitatively like atomic wavefunctions, but of course differ in the details.

4.4 Conclusion

In this chapter I presented a new way to think about the shape of a random walk. The principal components in the Eulerian perspective are directly relevant to experiments that probe the density distribution of a polymer. Thus they play a role in light scattering and fluorescence imaging. These principal components may also form a good starting point for thinking about polymer rheology, dynamics, and phase transitions.

Chapter 5

Hardware Trap

The invention of traps for individual atoms and molecules in the gas phase led to new physical measurements (e.g. of the anomalous magnetic moment of the electron[122]), and new analytical techniques (e.g. ion cyclotron mass spectrometry[34]). Molecules in solution show much more complex behavior than molecules in the gas phase, but until now there have not existed devices capable of trapping small molecules in solution. We used a redesigned ABEL trap to confine individual fluorophores (molecular weight ~ 500) in water at room temperature. These fluorophores have a mass smaller by a factor of 6×10^4 than that of the smallest objects previously trapped under comparable conditions.

Since its invention, the ABEL trap has had the potential to trap very small objects. Until now, its trapping strength was limited by the latency of the feedback loop. An ABEL trap based on video tracking and computer-controlled feedback had a minimum latency of 4.5 ms, principally due to the 300 Hz maximum frame-rate of the camera. This latency set a lower bound of 20 nm on the diameter of objects that could be trapped in water (although smaller objects could be trapped by increasing the viscosity of the solution).

The ABEL trap described here has a feedback latency of 25 μs, almost 200 times faster than earlier devices. At photon count rates below 40 kHz, feedback is provided on every detected photon, which is the quantum limit for a feedback trap. Single molecules can be trapped to an area with dimension roughly given by the distance the molecule diffuses between photon detection events. For a molecule with a diffusion coefficient of 280 $\mu\text{m}^2/\text{s}$ (Rhodamine 6G in water), and a photon count-rate of 20,000 counts/s, this distance is 170 nm.

5.1 Tracking and feedback apparatus

Our tracking system is a variant of the rotating laser method originally proposed by Enderlein, [42] and first implemented by Berglund and Mabuchi.[14, 15] Fig. 5.1 shows a schematic of the apparatus. The essential idea is that the laser beam rotates in a circle at a high speed, and the amplitude and phase of the fluorescence modulation of the target particle indicate its position.

5.1.1 Illumination train

The centerpiece of the illumination subsystem is an X-Y acousto-optic beam deflector (AOBD; Neos Technologies, Melbourne FL). The AOBD consists of a pair of shear-wave TeO_2 crystals, each with a 5 mm aperture. I built a custom mount to hold these crystals perpendicular to each other and to the direction of beam propagation. The 2 W RF driver for the crystals allows both FM and AM modulation, so one can control both the angle and the intensity of the diffracted beam. The AOBD is designed to deflect light with wavelengths between 488 nm and 633 nm, although we have only used 532 nm. The diffraction efficiency is very sensitive to proper alignment. The best I have achieved is 35% power transmission into the (1,1) diffracted beam. With no OD in front of the laser, this power (11 mW) is sufficient to saturate single molecules.

Ideally one would like the rotation frequency of the laser beam to be as high as possible. The rotation frequency sets the maximum bandwidth of the feedback loop. As long as the rotation frequency is much higher than the maximum photon detection rate, the bandwidth is limited by photon statistics. A further advantage of a high rotation frequency is that it pushes the dynamics of the feedback to a higher frequency, freeing low-frequency bandwidth for studies on the dynamics of the trapped object.

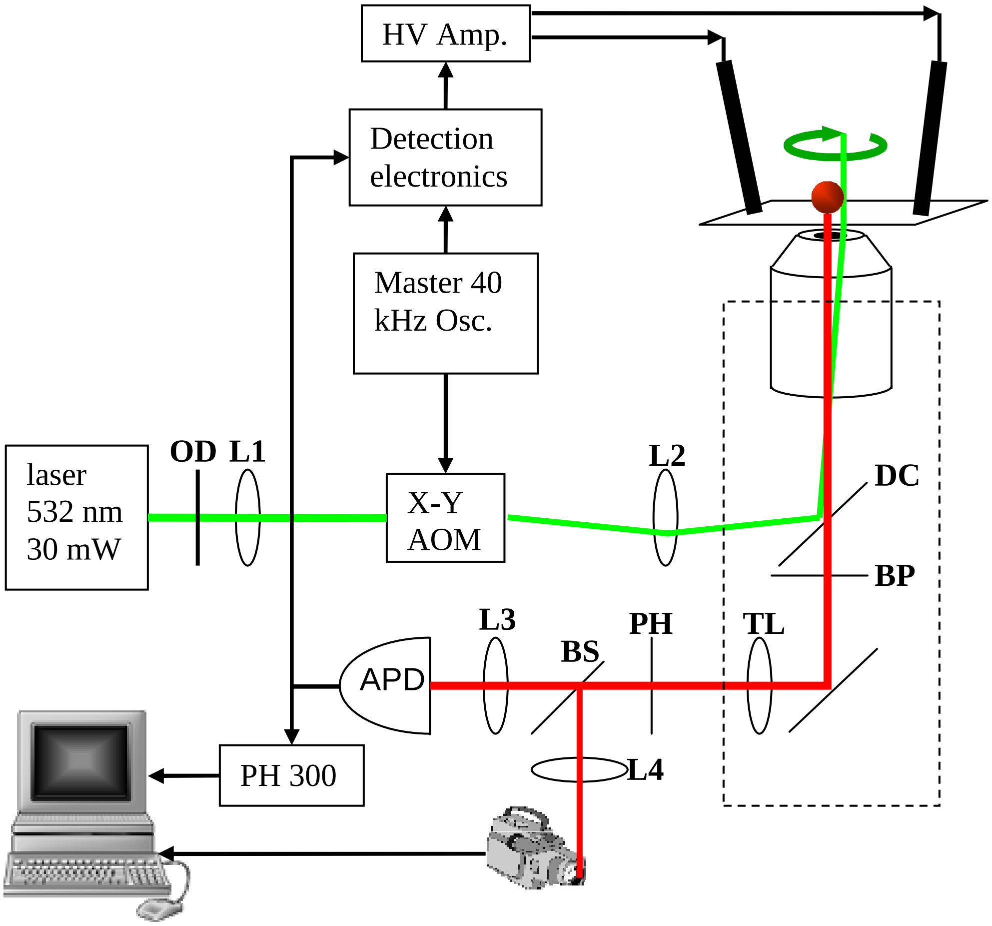

Figure 5.1: Schematic of the hardware-feedback ABEL trap.

The physical properties of the AOBDs constrain the maximum rotation rate. TeO_2 AOBDs come in two varieties, shear-wave and longitudinal. The maximum rate at which the beam can be swept depends on the time for the acoustic wave to propagate across the illuminated area of the crystal. Shear waves travel at 660 m/s, while longitudinal waves travel at 4260 m/s. With a 1 mm illuminated region, the transit times are 1.5 μs (shear) and 230 ns (longitudinal). To avoid blurring, the deflection angle must change on a timescale much slower than the transit time, setting a maximum frequency of 40 kHz for shear waves or 260 kHz for longitudinal waves. Shear-wave AOBDs achieve a larger angular deflection than the longitudinal ones and I was concerned about achieving a large enough deflection angle, so I selected the shear-wave AOBDs. It turns out that we only need a small deflection angle, so the longitudinal-wave AOBDs would have worked, and would have allowed rotation frequencies $>$ 200 kHz. If I build another ABEL trap it will use longitudinal-wave AOBDs.

A pair of 40 kHz sinusoids controls the deflection of the AOBDs. The two channels of the AOBD undergo different phase lags and have different sensitivities (change in beam angle per applied voltage), so it is necessary to control the amplitude and relative phase of the two drive signals independently. This is accomplished with a pair of phase-locked function generators. An adjustable DC offset is added to the drive signals to tune the RF drivers to center frequencies where the diffraction is most efficient (Fig. 5.2). An additional low-frequency signal from the computer or other source can be added to the AOBD drive voltages. This signal is used to move the trap-position by a small amount in real time. By modulating the position of the trap center one can learn about the electrokinetic mobility of the trapped object (see sec. 5.2.2).

The placement of lenses in the illumination train is a subtle issue subject to several constraints. Inside the trapping region, the laser beam has a width and a divergence angle. Furthermore, the AOBD causes the center of the beam to describe a cone, with its own width in the trapping region and divergence angle. How should one select these four parameters (beam width w_b, beam divergence θ_b, cone width w_c, cone divergence θ_c) for optimal trapping? How can one implement this choice subject to

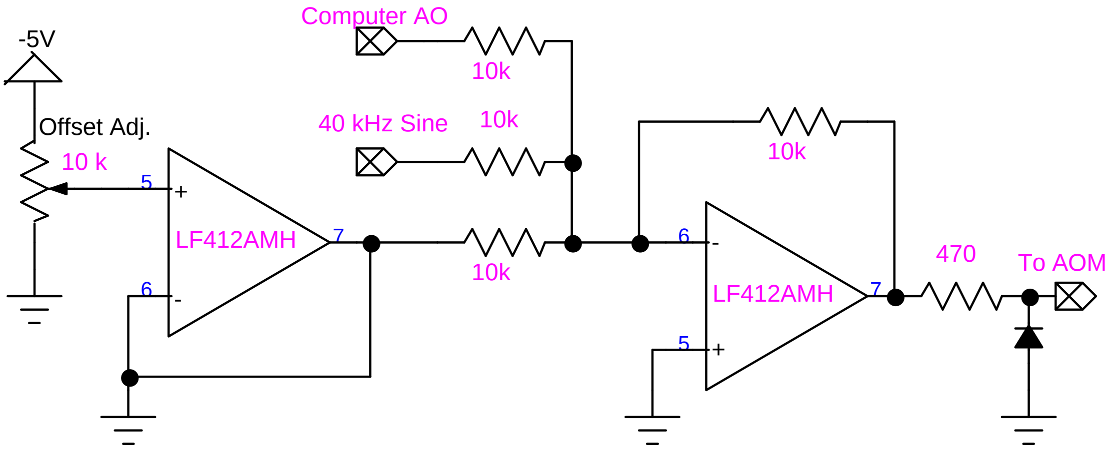

Figure 5.2: One channel of the AOM driver circuit. A second identical channel drives the perpendicular direction.

the limitations of diffraction and the AOBD? We will now start with the illumination pattern we want, and then work backward through the optical system.

Let's start by considering the two-dimensional problem. In the limit of a very thin trapping region, the divergence angles of the beam and of the cone are irrelevant; one only has to consider their widths. Clearly one wants $w_b \sim w_c$. If $w_c \gg w_b$ then the illumination is annular and particles in the center of the trapping region are not pumped. If $w_c \ll w_b$ then there is very little modulation in the fluorescence intensity as a particle moves away from the center. The largest modulation is obtained when the center of revolution coincides with the point of maximum gradient in the intensity of the beam. But this still leaves the question of how big to make the illumination pattern.

Increasing the radius of the illuminated region increases the distance a particle must go before it escapes. This decreases the average force required to set a well-depth of several $k_B T$, and allows more time for the feedback to catch a particle before it diffuses out of the trap. Thus regardless of whether the trap is limited by feedback latency or feedback strength, larger trapping regions help.

On the other hand, the signal from the particle is proportional to the time-average *intensity* of the excitation, while the background is proportional to the time-average *power*. Thus the signal-to-noise ratio (SNR) increases with *decreasing* illumination area. The background may come from Raman scattering, autofluorescence, laser light leaking through the emission filters, or the presence of other fluorescent particles in the solution. This last issue is particularly important. The illuminated region sets the capture radius of the trap. The larger this region, the more likely it is that at a given concentration more than one particle will enter the trapping region. Thus to maintain a certain trapping time without interference from other fluorescent particles, larger illumination regions require working at lower concentrations. This in turn increases the requirements on sample purity, an important factor when working at picomolar concentrations. I found a 2 micron diameter illumination region (with a 0.75 μm illumination spot) worked well under most conditions.

The question of the two divergence angles, θ_b and θ_c is more tricky. As the illumination spot becomes smaller, diffraction requires that the divergence angles increase. Ideally the beam itself will come to a focus in the trapping region, and will have a confocal length greater than the depth of the trapping region. The confocal length b is given by

$$b = \frac{2\pi w_b^2}{\lambda}, \tag{5.1}$$

where λ is the wavelength of light and w_b is the radius of the waist. With $w_b = 0.75$ μm we achieve $b = 6.6$ μm with 532 nm light, which is long enough to consider the beam as purely collimated in the trapping region. The far-field divergence angle of this beam is

$$\theta_b = \frac{\lambda}{\pi w_b}, \tag{5.2}$$

which for the scenario we are considering is 13°. Since we can achieve a pencil beam in a trapping region of reasonable depth (< 1 μm), we want this beam to propagate purely perpendicular to the trapping plane, i.e. $\theta_c = 0$. Fig. 5.3a shows the desired illumination pattern.

We will now follow the beam backward through Fig. 5.3b, first considering the beam shape, and then considering the effect of the AOBD. The 100x objective has a focal length $f_O = 2$ mm. To achieve a convergence angle of 13°, the beam entering the objective should be collimated and have a radius of $2\sin(13^\circ) = 0.45$ mm. Such a beam has a Rayleigh length of 1.2 m, so we can consider it to propagate as a pencil beam on the scale of tens of centimeters. The lens combination **L1,L2** spaced by $f_1 + f_2$ decreases the diameter of the beam emerging from the laser by a factor of f_1/f_2. Our 532 nm 30 mW green laser diode (World Star Tech, Toronto, Canada) generates a beam with a radius of ~ 1 mm, so we want $f_1/f_2 \sim 2$.

Now we turn to the AOBD. We want the AOBD to change the position at which the beam emerges from the objective, without changing the direction of propagation. Following the beam backward from the objective, this means that the AOBD must change the *angle* of the beam at the back focal plane of the objective, but not its position. Placing lens **L2** a distance $2f_2$ from the back focal plane, and the AOBD another $2f_2$ behind **L2** achieves this. The net result of the optics shown in Fig. 5.3b is that the beam itself experiences confocal optics (albeit with a low NA to generate an expanded focal spot), while the modulation imposed by the AOBD experiences Köhler optics.

5.1.2 Detection train

The collection optics are shown in Fig. 5.4. Fluorescence from the particle is collected by the objective and passes through a dichroic longpass filter (545DCLP Chroma), followed by two bandpass emission filters (550LP, Chroma). The tube lens, **TL**, has a focal length of $f_{TL} = 200$ mm and focuses the image onto a 200 μm pinhole (corresponding to 2 μm in the sample plane). A filter wheel allows the beamsplitter **BS** to be selected from the values R/T = 100/0, 90/10, 50/50, 4/96, 0/100. Different beamsplitters have different thicknesses, and thus translate the transmitted beam by different amounts. A slight shift in the image registration on the camera is unimportant, while on the APD shifting the image would cause the light to miss the active area. This is why the transmitted light is sent to the camera and the reflected light to the APD. A 20x air objective **L3** focuses the light on the APD (SPCM-CD 2801, Perkin Elmer, 250 dark counts/sec). Lens **L4** has a focal length of $f_4 = 10$ cm and focuses the light onto the camera (Cascade 512B, Roper Scientific). The images from the camera are recorded on a computer. The TTL pulses from the APD go to a 1:3 TTL fanout box. One output of the fanout goes to a PicoHarp 300 Time-Correlated

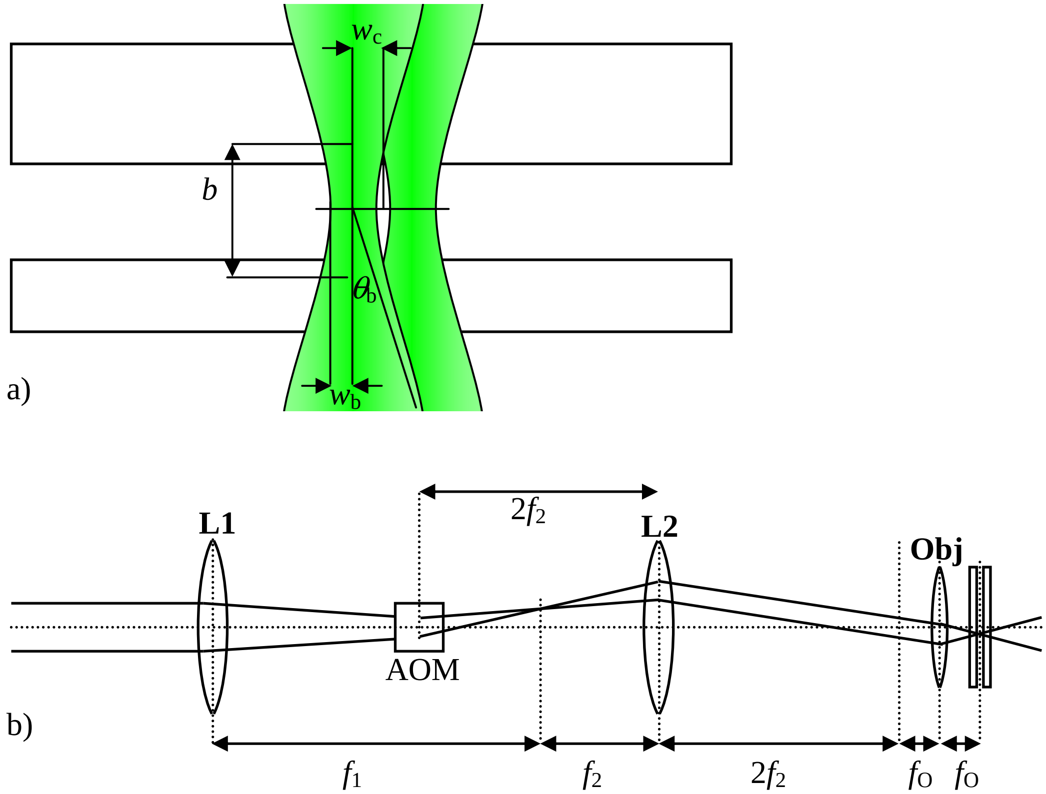

Figure 5.3: Excitation path for the hardware-feedback ABEL trap. a) Geometry of the excitation beam in the trapping region. We want the beam to propagate perpendicular to the trapping plane, and to have a confocal depth much greater than the depth of the trapping region. b) Optical setup to create the beam pictured in (a). Lens **L1** has a focal length of $f_1 = 40$ cm and lens **L2** has a focal length of $f_2 = 18$ cm.

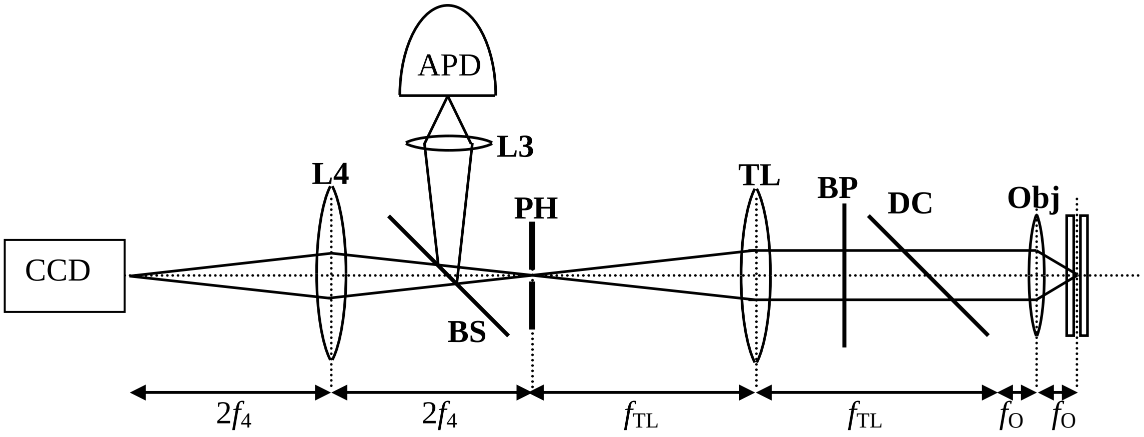

Figure 5.4: Detection path for the hardware-feedback ABEL trap.

Single Photon Counting (TCSPC) module (Picoquant, Berlin, Germany), and the other output goes to the demodulation electronics.

5.1.3 Photon-by-photon feedback

Initially I used a vector lock-in amplifier (SR-844, Stanford Research Systems, Sunnyvale, California) for the demodulation. The raw signal from the APD went into the input channel, and a 40 kHz reference square wave went into the reference channel. By adjusting the "phase" knob on the lock-in I could adjust the x and y output channels to reflect the x and y displacements of the trapped particle. While this approach worked, it introduced too long a latency for trapping of very small objects. Even with the shortest possible integration time of 100 μs, the device had a fixed system delay of $\sim$ 150 μs, leading to a total feedback latency of 250 μs, or 10 times the laser rotation period.

To reach the ultimate feedback bandwidth allowed by the 40 kHz AOBD frequency, I built two versions of the demodulation electronics, applicable to average count rates either greater than or less than 40 kHz.

Count rates < 40 kHz

In the system designed for low count rates, feedback is provided almost instantaneously on every detected photon. Every time a photon is detected, the electronics generate a pair of voltages which, treated as a vector, point in the instantaneous direction of the beam deflection. These voltages are amplified, inverted, and applied to the trap. Thus whenever the particle emits a photon it receives a kick directed radially inward toward the target location. Fig. 5.5 shows the circuit.

Starting on the upper left of Fig. 5.5, op-amp **U2** takes a reference 40 kHz sine wave phase locked to the AOBD drive signal and generates a cosine of the same amplitude (nominally 2 V peak). This quadrature pair forms the reference signals. The AD8182 is a dual high-speed analog multiplexer, originally designed for video switching applications. The TTL pulses from the APD switch the outputs of the AD8182 between ground and the reference sinusoids. Each APD pulse is 5 V high and 30 ns long. Thus the two outputs of the AD8182 are pulses 30 ns long, sampled from a sine and cosine, respectively.

The diagram in Fig. 5.5 only shows the electronics for the sine channel; identical electronics process the cosine channel. The 30 ns pulses from the AD8182 are too short to send to the high-voltage amplifier, so I send them through a one-pole low-pass filter with a time constant of 25 μs. This filter extends the duration of each pulse to ~ 25 μs, but also diminishes the amplitude to ~ 3 mV. The two op-amps **U3** and **U4** together provide a factor of ~ 2100 gain, bringing the amplitude of the pulse up to ~ 6 V. I used a simple low-pass filter to extend the pulse, rather than a one-shot, because the low-pass filter is linear: if a second pulse arrives within 25 μs of the first, the signals from the two pulses simply add together. This prevents any pulses from getting dropped, as would occur with a one-shot. The output of op-amp **U4** goes to a high voltage amplifier, with a variable gain of 0–10 and a bipolar output up to ± 150 V. The muscle for the amplifier comes from four PA-83 high voltage op-amps (Apex Microtechnologies, Tucson Arizona).

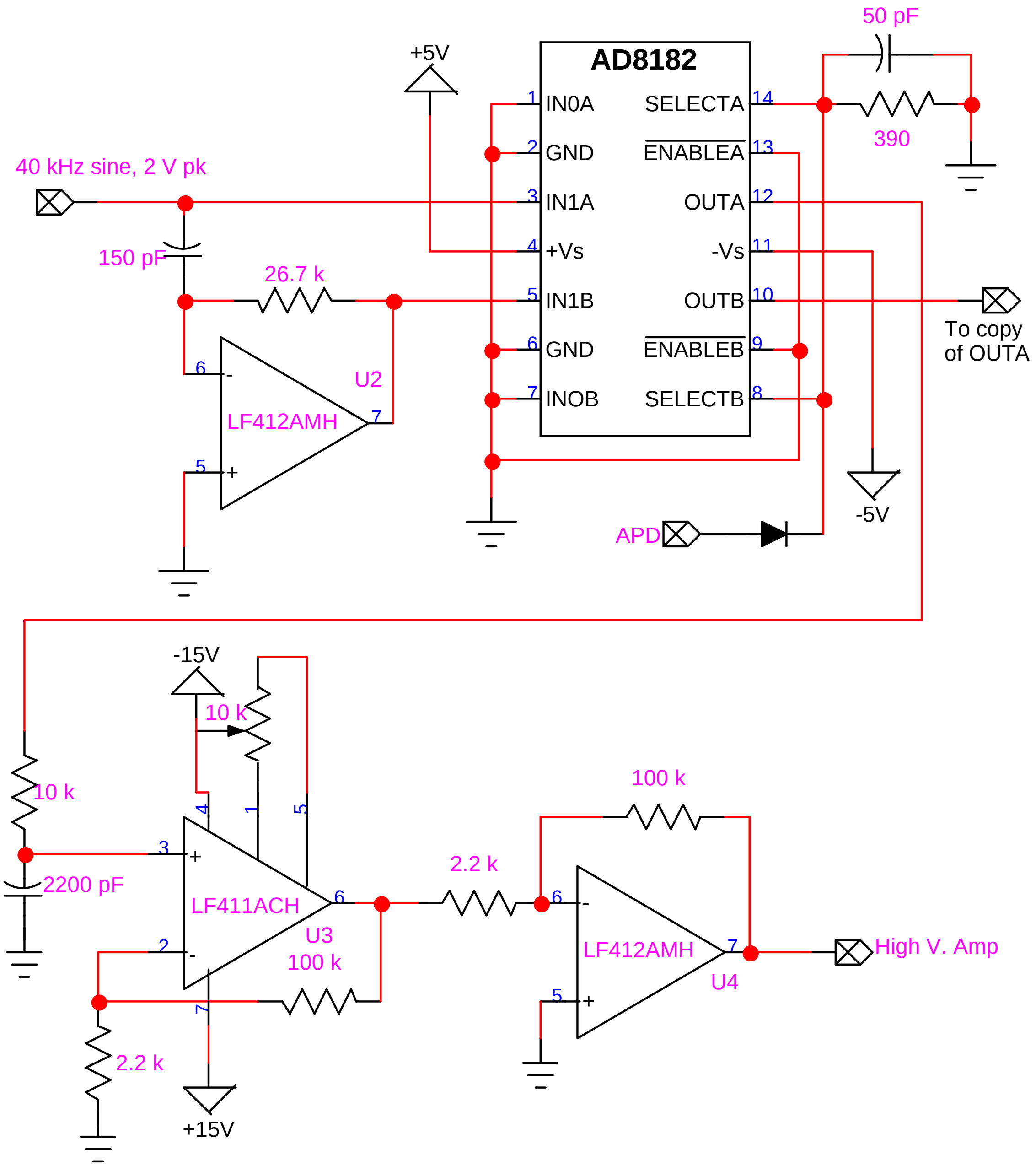

Figure 5.5: Demodulation circuit for providing instantaneous feedback on every detected photon in the hardware-feedback ABEL trap. The lower part of the circuit is replicated for the cosine channel.

Count rates > 40 kHz

At count rates greater than 40 kHz, the circuit of Fig. 5.5 introduces a strong spurious signal at the 40 kHz rotation frequency. This signal leads to unnecessary heating of the solution and causes a trapped particle to spin in a circle at 40 kHz. The problem is that if many photons arrive in one rotation period, each photon causes a kick radially inward, even if the particle is fixed exactly at the center of rotation of the laser beam. Thus a bright particle will experience a strong electric field rotating at 40 kHz.

To remedy this problem, I built a circuit with a zero in the feedback response at 40 kHz (and all harmonics). The idea is to integrate the effect of all the photon pulses for one rotation period, and only then to apply the feedback voltages. The cost of this procedure is an increase in the feedback latency from essentially zero to ~ 25 μs. Nonetheless, this delay should be short enough to trap single fluorophores in water. The circuit starts the same as the circuit in Fig. 5.5: an AD8182 multiplies the APD pulses by a sine and cosine. But then these pulses go through additional processing. During each revolution of the laser beam, an integrator adds up the effects of all the pulses in each channel. At the end of the revolution a sample-and-hold circuit grabs the voltage from the integrator and applies it as feedback during the subsequent revolution. Meanwhile the integrator is reset to zero and starts accumulating pulses anew.

Now I will discuss this circuit in detail. Fig. 5.6 shows the auxiliary timing electronics for generating the sample-and-hold and integrator-reset pulses. As in Fig. 5.5, the op-amp **U2** generates a cosine from the input sine wave, as a reference signal to multiply the APD pulses. The three LM311 comparators generate the timing pulses. The first comparator generates a square wave phase-locked to the input sine wave. The relative phases of the sine and square waves are unimportant, as long as the relationship remains fixed. On the downward transition of the square wave the second comparator generates an upward pulse, *PULSE A*, of duration ~ 0.7 μs. *PULSE A* drives the sample-and-hold circuit in Fig. 5.7. The falling edge of *PULSE A* causes the third comparator to generate an upward pulse, *PULSE B*, also of duration ~ 0.7 μs. *PULSE B* resets the integrator in Fig. 5.7.

Fig. 5.7 shows the integrator and sample-and-hold circuits. The LF411 op-amp

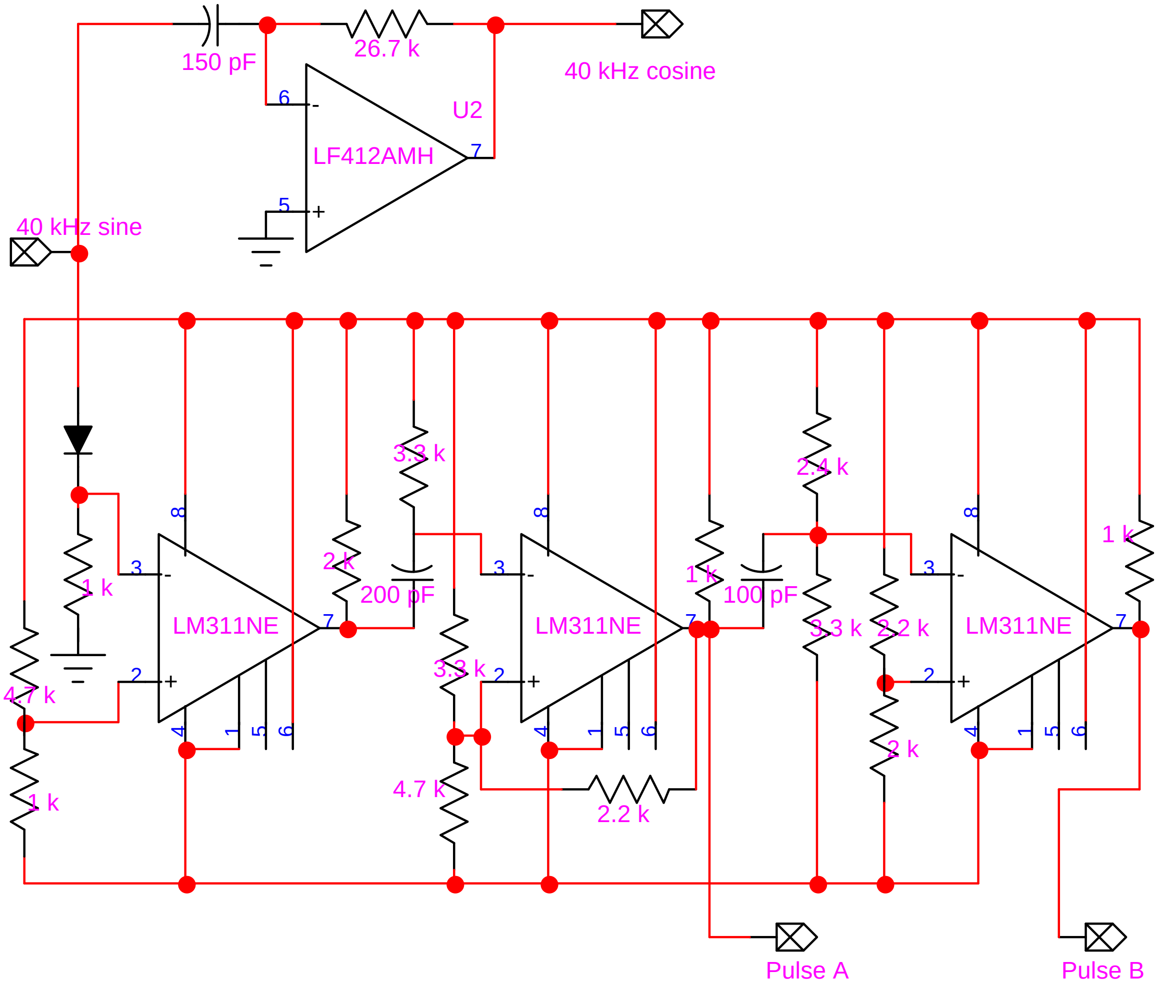

Figure 5.6: Subcircuit for generating timing pulses for the integrated-feedback ABEL trap.

on the left is configured as an integrator, so it adds up the effects of all the impulses it receives from the AD8182. The ADG333A is a quad SPDT analog switch. On receipt of *PULSE A* from the timing subcircuit, one unit of the ADG333A briefly connects the output of the integrator to a 10 nF capacitor. The voltage on the capacitor is buffered, amplified, and filtered (to remove some high-frequency noise) by the LF411 op-amp on the right. On receipt of *PULSE B* (immediately following *PULSE A*) a second unit of the ADG333A short circuits the capacitor in the integrator circuit, resetting the output to zero. Thus the output of the circuit is proportional to the offset of the particle integrated over the preceding revolution of the laser. An identical copy of the gated integrator and sample-and-hold circuit is used for the cosine channel.

A further advantage of the integrated feedback circuit is that it maps exactly onto the discrete-time feedback scheme discussed in Section 1.6. Thus all the computational machinery developed for the software-tracking ABEL trap (e.g. pseudo-free trajectories, calculated fluctuation spectra) can be equally well applied to the hardware-tracking ABEL trap.

5.1.4 Fused silica sample cell

The hardware-feedback ABEL trap is much more sensitive to background autofluorescence than the software ABEL trap because the hardware setup collects *all* the photons from the 2 μm-diameter trapping region onto a single APD pixel. Also the hardware-feedback ABEL trap is fast enough to trap very small objects, which tend to be dim and thus have a low SNR. I found that the glass microfluidic cells used in the software trap had too much autofluorescence to be used in the hardware trap. When excited at 532 nm, fused silica has $\sim 40\times$ less autofluorescence than Corning 7740 borosilicate glass. The problem with fused silica is that it is an extremely difficult material to work with: it is harder than most other materials and resistant to most dry or wet etching procedures.

Fused silica microfluidic cells were made in the Stanford Nanofabrication Facility through a variant of the process used to make the glass cells (Section 2.8). Fused silica wafers were coated with a CVD layer of Si. A pattern similar to that used

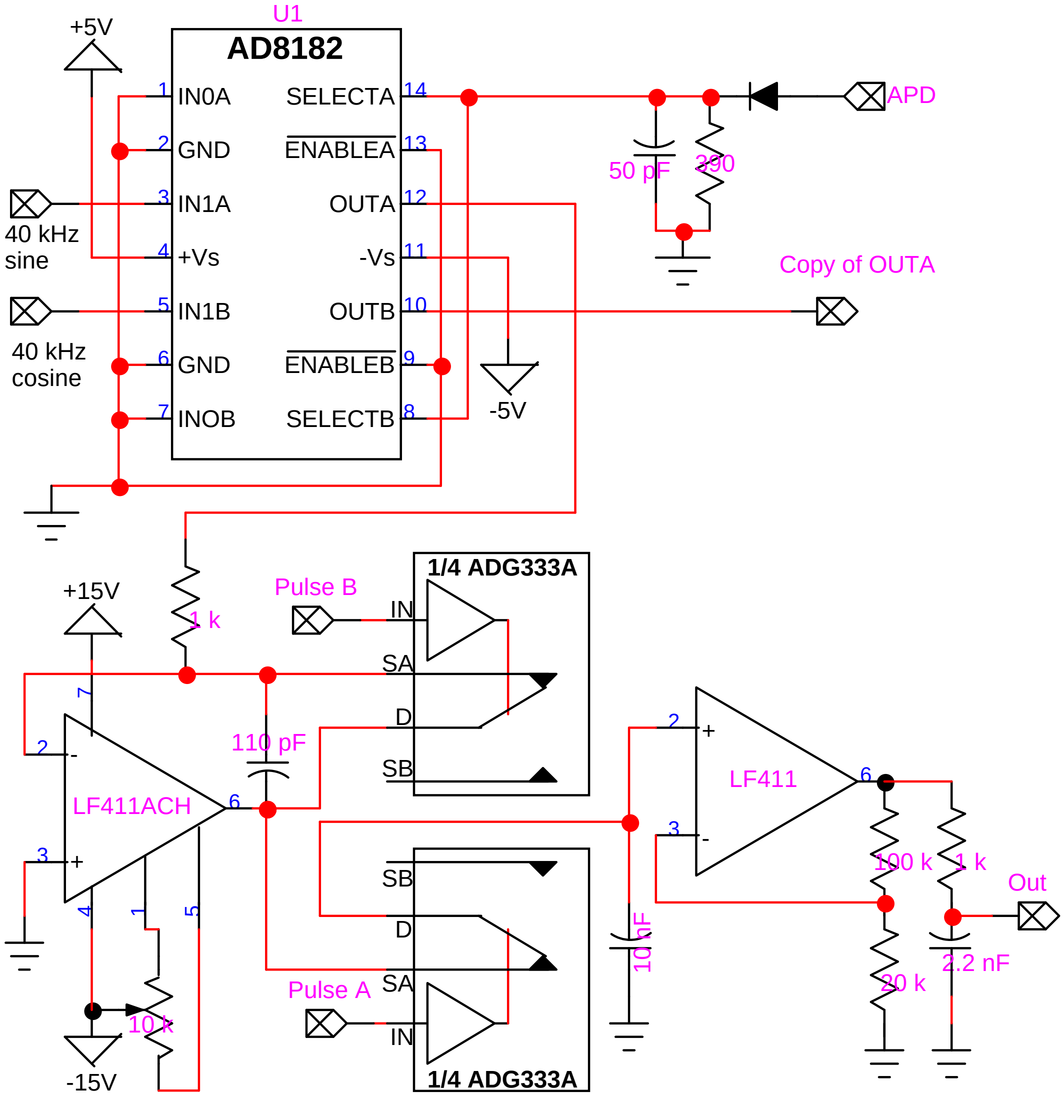

Figure 5.7: Demodulation circuit for providing hardware feedback integrated over one 25 μs rotation period of the laser beam.

for the glass cells was transferred into the Si, and then $\sim 20\ \mu$m into the silica via an etch in 6:1 BOE. The etch rate of fused silica in HF is many times slower than that of glass, so the etch lasted several hours. In the glass cells, the depth of the trapping region was set by mechanical pressure bowing the glass down toward the coverslip. This procedure was inconvenient because it was difficult to determine the precise depth of the trapping region. In the fused silica cells, I chose to use another step of lithography to determine the depth of the trapping region. After forming the deep channels leading to the control electrodes, I exposed a second pattern that consisted of support "wedges" extending into the trapping region. I transferred the pattern into the Si via a SF_6 RIE, and then transferred the pattern ~ 400 nm into the silica via a brief etch in 6:1 BOE. I then stripped the remainder of the Si.

I wanted the channels connecting the electrodes to the trapping region to be several hundred microns deep, but this was not possible with the HF etch, both because of the slow etch rate and because the etch is isotropic so such a deep etch would fuse adjacent channels. To make deep channels leading to the trapping region I used a high speed diamond micro-drill (Abrasive Technology, Lewis Center, Ohio) and manually milled out deeper channels. Fig. 5.8 shows the center of the trapping region in the fused silica cell. I used the same sample holder as for the glass cells, but now I compressed the trapping region as far as possible, relying on the topography of the sample cell to set the depth to $\sim 400\ \mu$m.

5.2 Characterization of the trap

One of the challenges of working with the hardware-feedback ABEL trap is that the system is very sensitive to the optical alignment and to small phase shifts in the electronics. These sources of error are not simple to detect or to diagnose. To aid with troubleshooting and calibration, I built an additional subsystem for scanning a fixed fluorescent bead through the trapping region. The scanning was performed using a three-axis piezoelectric stage (Physik Instrumente, Karlsruhe, Germany), controlled by home-made software written in Visual Basic. Fig. 5.9 shows a typical calibration scan, made using a 100 nm bead and a 400 μm pinhole (corresponding to 4 μm in the

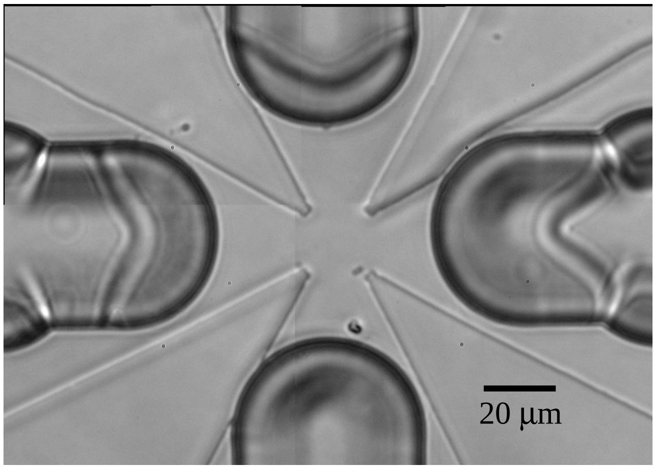

Figure 5.8: Fused silica microfluidic cell for the hardware-feedback ABEL trap. The ends of the deep channels extend from the edges of the image. The wedges jutting from the corners are raised $\sim$ 400 nm above the trapping region and set the depth of the trapping region. These wedges also act to focus the electric field into the center of the trapping region.

sample plane. From Fig. 5.9 we see that the average photon count rate is relatively independent of the position of the bead within the trapping region and that the feedback voltages is relatively independent of the the z position of the bead.

How accurate is the hardware tracking system? Clearly one can obtain a better estimate of the position of a stationary particle by averaging for a longer time. Higher photon count rates also yield improved accuracy. We seek a measure that is independent of integration time or photon count rate, and depends purely on the geometry of the optical system. This is achieved by calculating the resolution times *square-route photons detected*. The units of resolution are $[R] = \mu\text{m}\sqrt{N}$, where N is the total number of photons detected in some interval. Given R, one can calculate the resolution for any given integration time and photon count rate.

Fig. 5.10 illustrates the procedure for obtaining R. A linear sweep of a bead through the trapping region yields a sensitivity of 0.76 V/μm of displacement in the central part where the response is linear. This number depends on the precise optical alignment, and is proportional to the photon count-rate and the gain in the electronics. Meanwhile, the standard deviation of the mean voltage (averaged over a

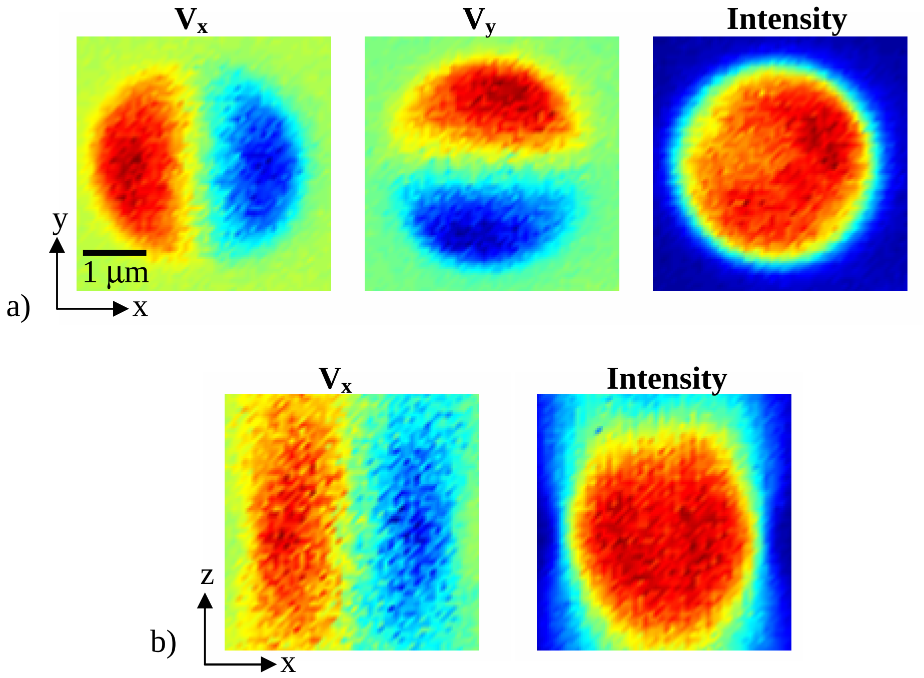

Figure 5.9: Calibration of the ABEL trap performed by scanning a fixed 100 nm fluorescent bead through the trapping region. a) Scan in the x-y plane. The x and y feedback voltages are proportional to the respective offsets of the particle, and the total photon count rate is independent of the offset. b) Scan in the x-z plane. The x feedback voltage is proportional to the offset, with a gain that does not vary strongly with z. Within a large region, the photon count rate is independent of position.

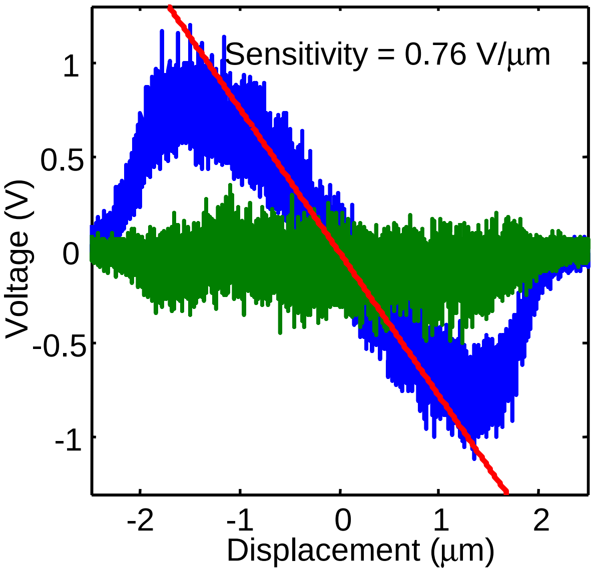

Figure 5.10: Feedback voltages as a 100 nm fluorescent bead is scanned through the trapping region. Blue: feedback voltage along the scan axis; green: voltage perpendicular to the scan axis. The sensitivity in this case is 0.76 V/μm and the noise is 1.4 μm$\sqrt{N}$.

25 ms interval) is 49.4 mV, which corresponds to an error in the position measurement of 65 nm. The average count rate during this experiment was 18,500 counts/s, which corresponds to 463 counts in a 25 ms interval. Thus the resolution of the system is $R = 65 \text{ nm} \times \sqrt{463} = 1.4\ \mu\text{m}\sqrt{N}$.

From this analysis we conclude that the accuracy of the tracking system described here is far below the diffraction limit of $R = 250 \text{ nm}\sqrt{N}$. This is because the beam is expanded to be much larger than the diffraction limit. By shrinking the beam one can increase the gradient in intensity in the center of the tracking region, without increasing the overall excitation intensity. Ideally the excitation region will be just large enough to keep the particle from escaping—any extra space only contributes to decreased SNR. Future designs will work toward shrinking the trapping region.

5.2.1 Trapping beads

Using the hardware-feedback ABEL trap, fluorescent polystyrene beads of diameter 100 nm and 26 nm were trapped so tightly that the video images showed no discernable Brownian motion. Fig. 5.11 shows the results of trapping a 100 nm bead, using the lock-in amplifier to provide feedback. In this experiment the lock-in was set to have an integration time of 100 μs and a roll-off of 6 dB/octave. Since the feedback bandwidth (several kHz) is far greater than the video frame rate (92 Hz in this case), it is not possible to determine the amplitude of the position fluctuations from the sequence of video images. However, an upper bound on the position fluctuations may be obtained from the histogram of feedback voltages. The sensitivity measured with a fixed bead at 12,200 counts/s was 0.49 V/μm; in the experiment the count rate was 119,000 counts/s, yielding a sensitivity of 4.78 V/μm. The voltage fluctuations were 1.12 V r.m.s.; if all of this were due to real fluctuations of the bead as opposed to shot-noise, the position fluctuations would be 230 nm, r.m.s. From the histogram of voltages alone it is not possible to determine how much smaller than 230 nm are the position fluctuations of the bead.

Next we examine the dynamics of the trapped particle. Our only measure of the activity of the particle is the record of feedback voltages used to hold it still. The dynamics of these voltages depends on the properties of the particle, but also on the properties of the feedback system, i.e. the measurement noise and the response function of the feedback electronics. Fortunately all of the variables that do not pertain directly to the particle can be measured off-line in other experiments. Thus we obtained the sensitivity of the trap by scanning a fixed particle through the trapping region. Similarly, we obtained the dynamic response function of the lock-in amplifier by applying a sinusoid at the reference frequency, amplitude modulated with a low-frequency square wave. The response function of the lock-in is the time-derivative of the output voltage measured under these conditions. Fig. 5.11c shows the response function of the lock-in. In this figure you can clearly see the unpleasant delay of $\sim$ 150 μs between $t = 0$ when the stimulus is applied and when the lock-output reaches its maximum value. Assuming that the velocity of the particle responds instantaneously to a feedback voltage, the dynamics of the system along one dimension

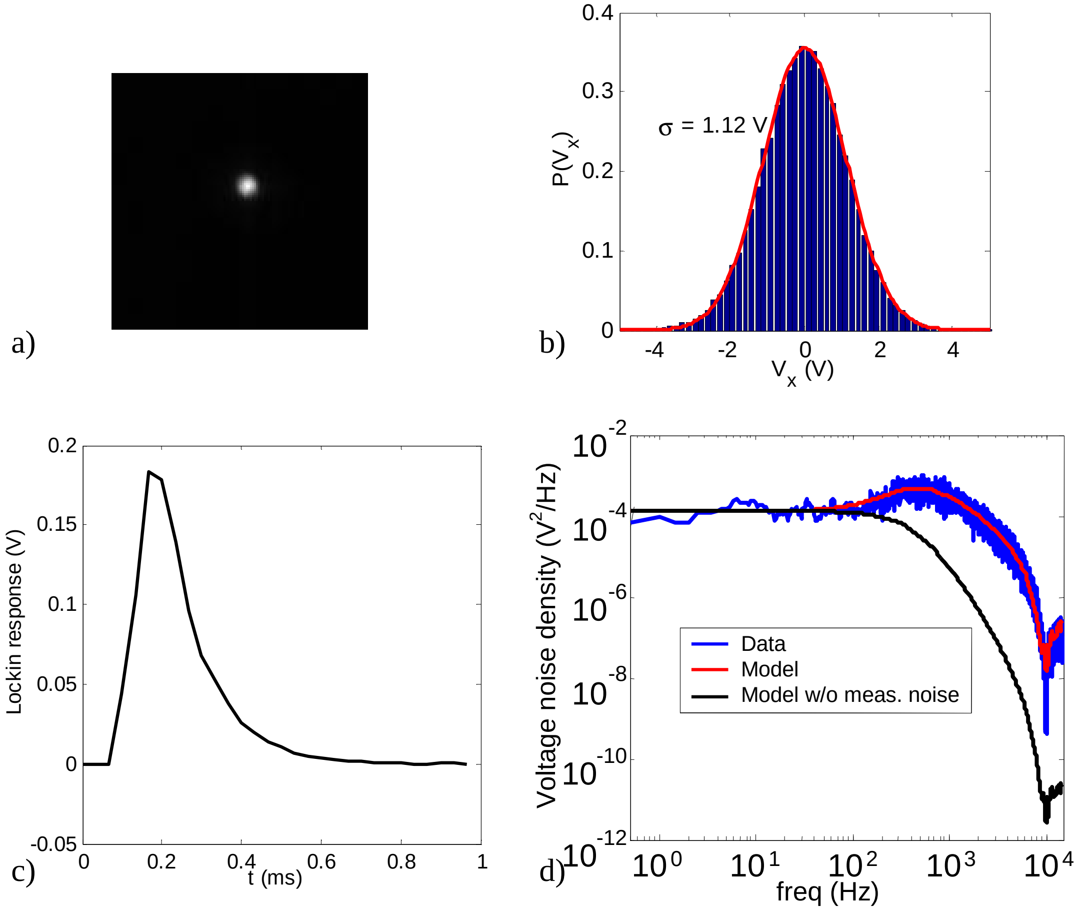

Figure 5.11: Trapping of a 100 nm bead in the hardware-feedback ABEL trap. a) Time-lapse image of a trapped bead. b) Histogram of voltages applied along the x-axis to keep the bead trapped. c) Impulse response function of the feedback electronics. The latency is dominated by the cruddy SR844 lock-in amplifier. d) Power spectrum of the voltage oscillations (blue), and fits based on Eq. 5.5 including the effect of measurement noise (red), and without measurement noise (black).

obey:

$$\begin{aligned} \frac{dx}{dt} &= -\mu E(t) + \xi(t) &(5.3)\\ E(t) &= \int_0^\infty d\tau\, AG(\tau)[x(t-\tau)+\chi(t-\tau)], &(5.4)\end{aligned}$$

where $G(\tau)$ is the impulse response of the lock-in (Fig. 5.11c), A is the gain of the tracking system, ξ is the Brownian noise, and χ is the measurement noise. Referring back to the discussion of control theory in Section 1.6 we can immediately determine the expected power spectrum of electric field (or voltage) fluctuations:

$$|\tilde{E}(\omega)|^2 = \frac{|A\tilde{G}|^2(|\tilde{\xi}|^2 + \omega^2|\tilde{\chi}|^2)}{\omega^2|1+\frac{A\mu\tilde{G}}{i\omega}|^2}. \tag{5.5}$$

Since the Brownian fluctuations and shot noise are both white noise, the terms $|\tilde{\xi}|^2$ and $|\tilde{\chi}|^2$ can both be replaced by constants. In the absence of other information, this formula has three free parameters, related to the mobility, the diffusion coefficient, and the measurement noise. If one takes data on a fixed particle of similar brightness, the measurement noise $|\tilde{\chi}|^2$ can be obtained independently, leaving two fitting parameters. Fig. 5.11d shows the measured power spectrum of the voltage fluctuations in trapping a 100 nm bead (blue), the fit obtained from Eq. 5.5 (red), and the fit that would be obtained if measurement noise were neglected (black).

It is simple to solve Eq. 5.3 for the power spectrum of the *position* fluctuations. Doing this yields:

$$|\tilde{x}(\omega)|^2 = \frac{|\tilde{\xi}|^2 + |A\mu\tilde{G}\tilde{\chi}|^2}{\omega^2|(1+\frac{A\mu\tilde{G}}{i\omega})|^2}. \tag{5.6}$$

Given the parameters obtained from the fit to the voltage fluctuations, and the known tracking sensitivity A, one can evaluate the power spectrum of the position fluctuations. Parseval's identity then yields the total variance in the position of the particle. For the particle in Fig. 5.11, this procedure yields r.m.s. position fluctuations of 88 nm, or an effective spring constant of 5.3×10^{-7} N/m. These numbers are reasonable given what we know about the diffusion coefficient and the latency. A 100 nm sphere has $D = 22\ \mu\text{m}^2/\text{s}$. With a latency of $t = 150\ \mu\text{s}$, we expect the sphere to diffuse $\sqrt{2Dt} = 81$ nm.

In principle the fitting parameters used to generate Fig. 5.11d could be used for highly precise measurements of the transport coefficients of a trapped bead, although I have not yet converted these parameters into sensible units.

5.2.2 Manipulating beads

Thermal fluctuations provide all possible sets of perturbations to a trapped particle, so the time series of feedback voltages for a stably trapped particle holds all the information one could hope to obtain about the particle. As we have seen, extracting information from stochastic trajectories can be a complicated task. Often the same information can be obtained far more directly by judiciously modulating the position of the center of the trap. In analogy to optical spectroscopy, there are several quantities beyond the vanilla mobility and diffusion coefficients one might like to measure:

1. Fluctuations in transport coefficients. These fluctuations may arise from conformational fluctuations, interactions with the environment, or ionization events, and their manifestations in the feedback statistics have already been discussed in Sections 1.7.1 and 3.5.

2. Dynamic electrokinetic response. In Section 1.4.4 I discussed why the velocity of a particle might depend on past electric fields as well as the instantaneous field.

3. Nonlinear response. The notion that the velocity is purely proportional to the electric field is an approximation. At high enough electric fields this proportionality will break down, either due to uninteresting effects such as Joule heating, or to interesting effects such as polarization or deformation of the particle.

These quantities are easier to measure if one wiggles the particle a little.

The AOM driver circuit (Fig. 5.2) accepts x and y voltages to move the center of rotation of the laser in an arbitrary pattern. As long as the modulation is small enough to keep the center of rotation within the field of view defined by the collection pinhole, a trapped particle will follow the indicated pattern.

Fig. 5.12 shows how one can measure the mobility of a trapped particle by stepping the trap center back and forth in a square-wave pattern. In this experiment, the trap center was stepped at 100 Hz, with increasing step sizes. Fig. 5.12a shows the the cycle-average response of the feedback voltage. Since the steps of the trap center are uncorrelated with the Brownian motion or the shot noise, these two effects do not contribute to the cycle-averaged response. The area under the voltage vs. time curve is a measure of the impulse the feedback system delivers to the particle. The slope of this impulse as a function of the step size gives the mobility (Fig. 5.12b). So for the bead studied here, the mobility was 26 μm/V·s.[1]

The modulation method for measuring mobility has some technical advantages over inferring the mobility from the feedback voltages with a fixed trap center. To derive Eq. 5.5 for a fixed trap center, we had to assume that the feedback signal was linear in the displacement. Fig. 5.10 shows that this is not true for large displacements. On the other hand, when we modulate the position of the trap center, we know *exactly* how far the center moved (this can be calibrated off-line). Just after the center undergoes a large step, the particle may be displaced far enough to be in the region where the tracking is nonlinear. This nonlinearity affects the shape of the voltage relaxation curve (Fig. 5.12a), but not the area under the curve. Thus the modulation method is insensitive to the details of the illumination pattern and to abberations in the optics.

To compare the function of my photon-by-photon feedback circuit with the SR844 lockin amplifier, I translated the trap center in a square wave pattern, and measured the cycle-averaged voltage response. Fig. 5.13 shows these results for two settings of the lock-in and for my circuit. From Fig. 5.13 it is clear that photon-by-photon feedback has a faster relaxation than any of the settings available on the lock-in amplifier.

---

[1] The usual units of mobility are μm^2/V·s. I do not know the precise electric field in the trapping region–only the voltage I apply–so I prefer to give mobilities in units of μm/V·s

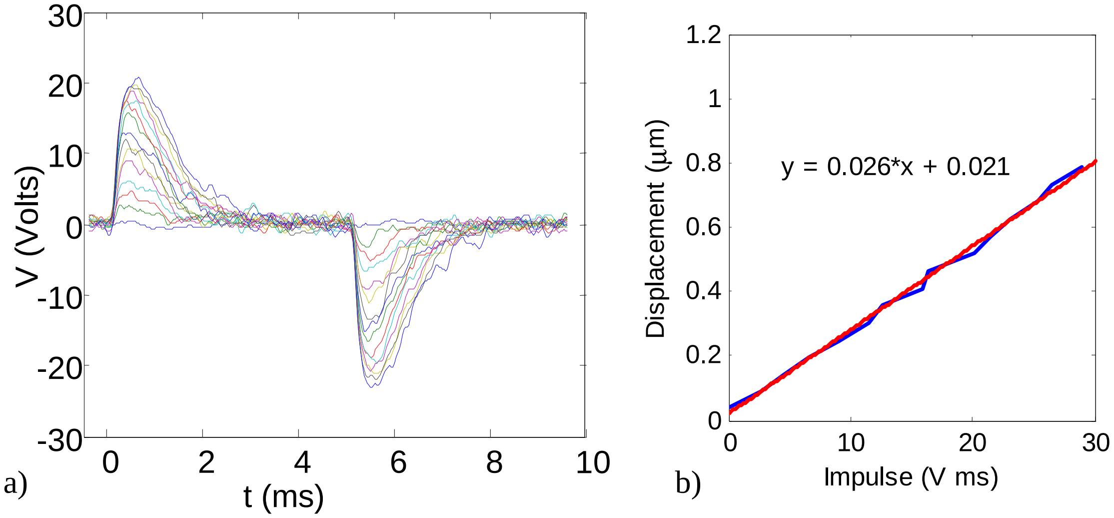

Figure 5.12: Measurement of the mobility of a trapped 100 nm bead. a) The position of the trap center was modulated with a square wave of increasing amplitude and the cycle-average voltage was recorded. b) The area under the voltage vs. time curve is proportional to the mobility.

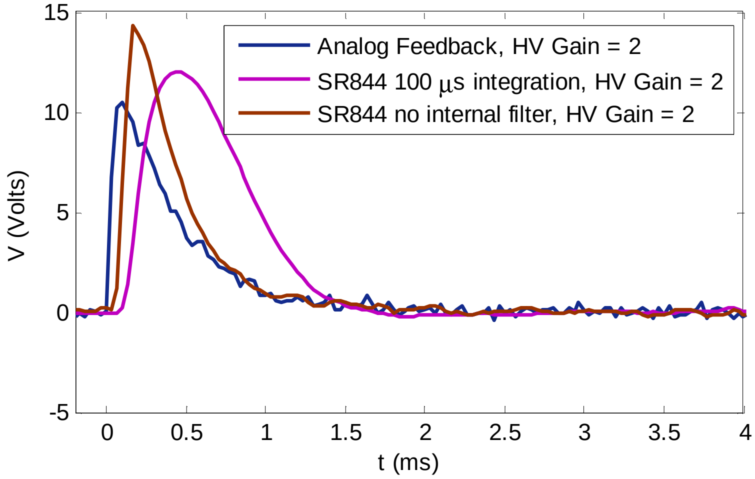

Figure 5.13: Comparison of the relaxation curves for a 100 nm bead subjected to a step displacement, where the feedback is provided either by a lock-in amplifier (brown, purple) or photon-by-photon (blue). The photon-by-photon feedback is faster.

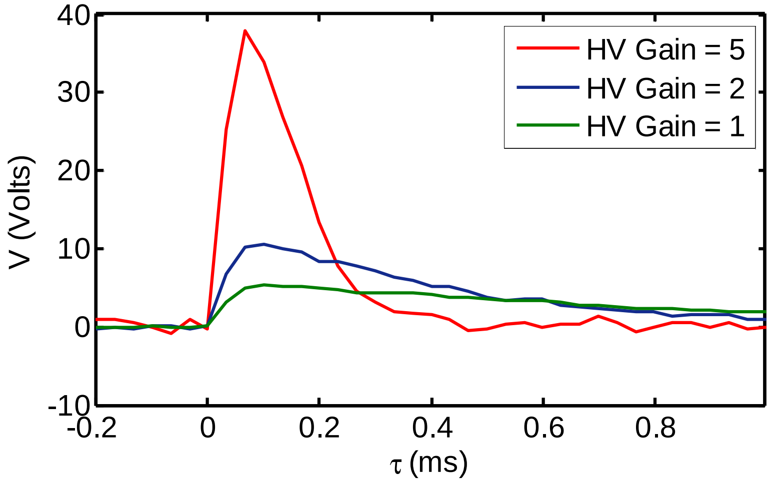

Figure 5.14: Relaxation curves of a trapped 100 nm bead with photon-by-photon feedback. The position of the trap center was modulated with a square wave, and the cycle-average voltage response was recorded. Even at the highest gain, the feedback mechanism avoids overshooting the target position.

When trapping particles with software feedback or with the lock-in amplifier, the particle would go into oscillations if the feedback gain was set too high. To test whether this occurred with the photon-by-photon feedback, I measured the voltage response to a step in the trap center as a function of the loop gain. Fig. 5.14 shows that even at the highest gains available, the voltage relaxation did not show any overshoot or ringing. At the highest gain setting, the relaxation time of the trap is ~ 100 μs, which should be fast enough to trap single molecules.

5.3 Trapping single molecules of GroEL

To test the trapping strength of the hardware-feedback setup, single molecules of fluorescently labeled GroEL were loaded into the trap. These were the same molecules that So Yeon Kim prepared for trapping in 50% glycerol under software feedback (Section 2.7.3), but here the molecules were trapped in buffer without glycerol. Each GroEL was labeled with, on average, 6 molecules of Cy3. Fig. 5.15 shows the results. Single molecules were clearly held in the trap, although surface-sticking and photobleaching were problems. Future work will focus on surface passivation and techniques for removing oxygen.

5.4 Trapping single molecules of Cy3

A “typical” protein has a diameter of 2.5 nm.[114, 47]. GroEL is much larger, roughly 14 nm by 18 nm. In fact, most of the proteins studied by single-molecule methods are either very large, or interact with something very large, e.g. DNA, actin, cell membrane, etc. This is because the molecule must somehow be immobilized for extended observation. For the ABEL trap to be truly useful, it should be able to trap objects smaller than ~ 2.5 nm in buffer. The smallest object one could conceive of trapping is a single fluorophore. Except for the rare cases of autofluorescent proteins, any protein held in the ABEL trap would be fluorescently labeled. Thus if one can trap a single fluorophore, one can trap any protein.

I worked on trapping single molecules of the fluorophore Cy3. This molecule has a molecular weight of 507, and is roughly 1.4 nm along its longest dimension. Cy3 absorbs in the green, and is relatively photostable in the absence of oxygen. A solution of Cy3-succinimidyl ester was incubated with a 1:2 molar ratio of DTT in order to hydrolyze the succinimide groups. Trapping was performed in an oxygen-scavenging buffer (HEPES (50 mM), glucose (4.5 mg/mL), glucose oxidase (0.43 mg/mL), catalase (72 μg/mL), and β-mercaptoethanol (5 μL/mL)) at a Cy3 concentration of 0.2 nM. HEPES was chosen as the trapping buffer because it is zwitterionic: it contributes very little to the conductivity of the solution, so Joule heating should not be a problem even at high feedback strengths. However, I later found that the HEPES contained fluorescent impurities, and thus is not ideal for trapping single fluorophores.

I was not able to definitively trap a single Cy3 for an extended time, although Fig. 5.16 shows that the residence times of single Cy3 molecules in the trap was dramatically enhanced. Fig. 5.16b shows histograms of the intensity in the trapping region, with the feedback on, off, and negative. The strong peak at 18 counts/ms is the background signal from scattered laser light, Raman scattering, and autofluorescence. The green trace (no feedback) shows a long tail extending up to 60 counts/ms.

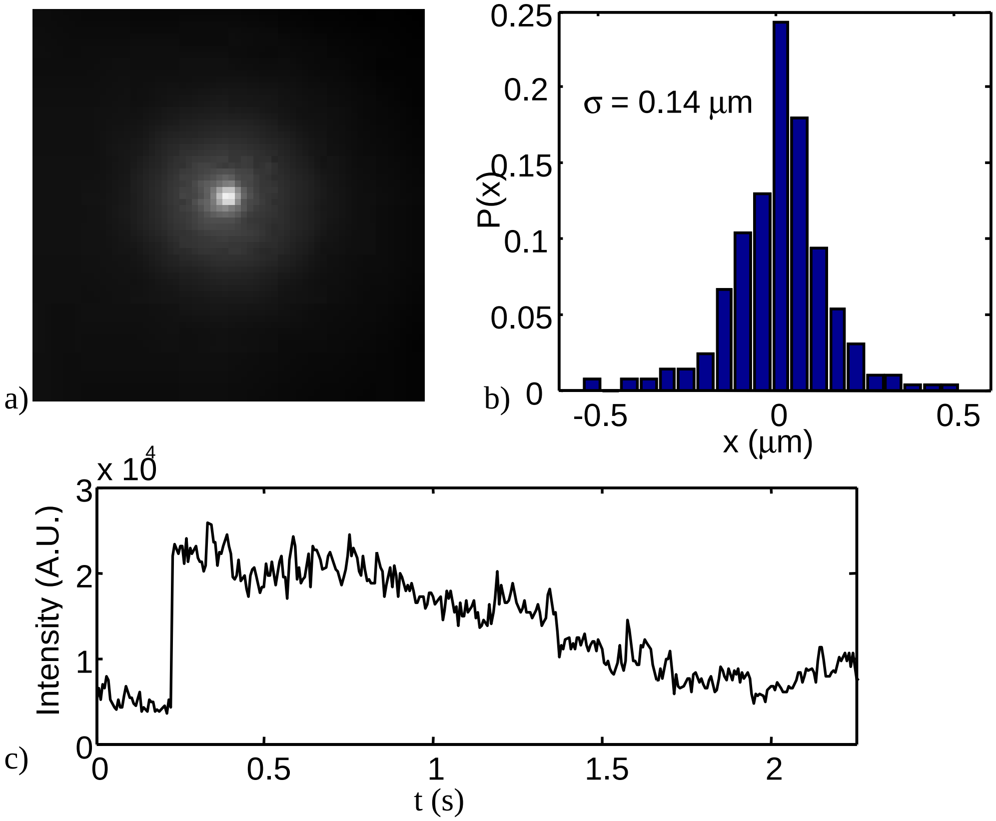

Figure 5.15: Trapping of a single GroEL in buffer. a) Time-lapse image of a single trapped molecule (held for ∼ 1.7 s). b) Histogram of the displacements of the molecule, extracted from the trajectory of video images. In this case it was not possible to estimate the position fluctuations from the voltage fluctuations (the trap was not calibrated at the time of the experiment). The true position fluctuations are likely to be larger than 140 nm because fast fluctuations are not detected by the camera. c) Photobleaching time-trace of the single molecule. If one looks at the time-trace charitably, one can see discrete photobleaching steps.

This tail is due to fluorophores diffusing in and out of the trapping region. When the feedback is turned on (blue trace) a discrete peak develops centered around 55 counts/ms. This peak corresponds to the intensity from a single fluorophore in the trap.

I was concerned that simply applying huge voltages to the trap (up to 100 V) was making molecules stick to the surface, or increasing the fluorescence in some way other than by canceling Brownian motion. As a control, I reversed the sign of the feedback, so any particle in the trapping region received kicks directed radially *outward*. The red curve shows that under these "anti-trapping" conditions, the long tail present in the free-diffusion trace disappeared. Thus it is possible to use the ABEL trap to create a localized *dip* in the concentration of fluorescent molecules.

Fig. 5.16c shows typical time-traces of the fluorescence intensity with the feedback off and on. The brief bursts in the top panel correspond to particles diffusing randomly through the trapping region. With the feedback on, the bursts last much longer; some as long as 500 ms. Fig. 5.16d shows the autocorrelation of the fluorescence intensity. Clearly the average residence time is greatly increased by feedback and decreased by anti-trapping. Nonetheless, molecules appear not to be held stably. At this point it is not clear whether the limitation is escape from the edges of the trap (due to the finite restoring force), or from the molecule going dark (due to a triplet state or photobleaching). Future work will examine other fluorophores with different photophysics, and the role of triplet-state quenchers such as KI. There are still many tricks to be played in the game of catching a single fluorophore.

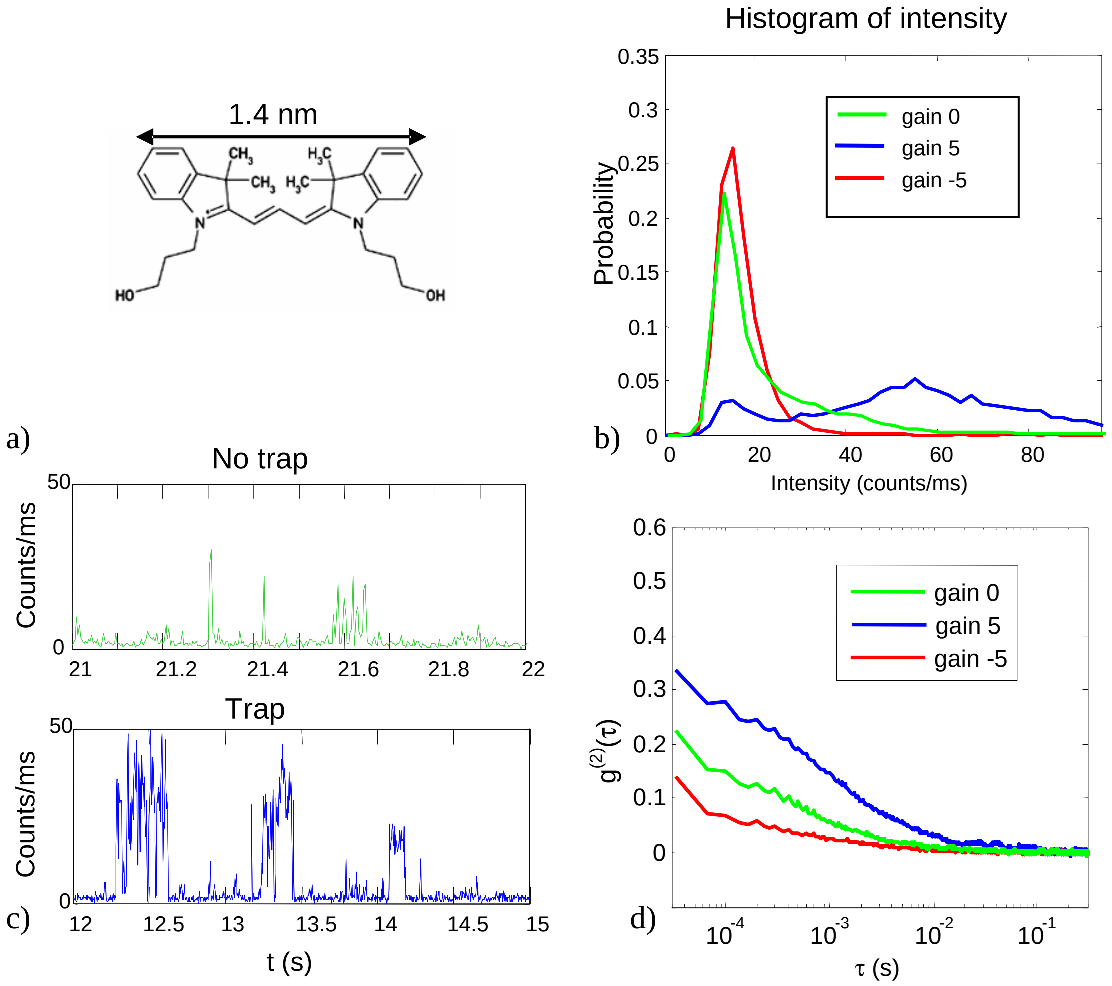

Figure 5.16: Trapping of Cy3. a) Molecular structure of Cy3. The molecular weight is 507 g/mol. b) Histogram of count-rates in the trapping region, with no feedback, feedback, and anti-feedback. c) Representative time-traces with and without feedback. d) Autocorrelation of the intensity with no feedback, feedback, and anti-feedback.

Chapter 6

Conclusion

In this thesis I have discussed the theory underlying the ABEL trap, described in detail how to build ABEL traps optimized for different types of experiments, and illustrated how the ABEL trap can be used to learn new things about molecules. In all three areas much work remains.

6.1 More theory

We are just beginning to understand how to interpret data from the ABEL trap. One can perform all the usual spectroscopic measurements on a trapped object (e.g. fluorescence lifetime, polarization, spectrum, FRET) and analyze this data as one would for a mechanically immobilized molecule. But the ABEL trap also provides new types of time-domain data. We recently added a PicoHarp 300, which gives the arrival time of every photon to within 4 ps. A minute of data can generate tens of millions of photon records. All this information is an embarrassment of riches: it is not totally clear what to do with the data.

The photon statistics contain information about the dynamics of the fluorophore and its interaction with the environment, but they also contain information about the feedback itself—the intensity power spectrum has a strong component at the rotation frequency of the laser. On timescales much longer and much shorter than the trap relaxation time, one may safely assume that any fluctuations are intrinsic to the trapped fluorophore; but on intermediate timescales many effects may be overlayed. Ultimately, we may need to develop a numerical simulation of the trap. Given a model of the fluorescence dynamics, one can simulate the expected record of photon statistics, and then compare with the data. Such simulations can be based on recent maximum likelihood[134, 130] and Bayesian[71] approaches to analyzing single-molecule data, or on hidden Markov models.[1, 117]

Besides the usual spectroscopic observables, the ABEL trap data contains information on the transport coefficients (mobility and diffusion coefficient), and possibly on fluctuations in these coefficients. There has been considerable interest in analyzing diffusion in heterogeneous environments,[28, 88] but much less attention has been paid to the case where the fluctuations are intrinsic to the diffusing particle. The ABEL trap may also be sensitive to fluctuations in the mobility, and such fluctuations have been predicted for small RNA fragments.[135] It is not clear how to extract such information from the record of feedback voltages, or how one should move the trap center to magnify the effect of fluctuations in transport coefficients. It is possible that models of Generalized Autoregressive Conditional Heteroskedasticity (GARCH), originally developed for financial markets, will provide a useful angle of attack.

With the hardware-feedback ABEL trap, fluctuations in the transport coefficients will change the feedback dynamics, and thus change the photon statistics. Also, fluctuations in the fluorescence intensity will change the feedback dynamics, and thus the voltage statistics. If there are changes in both the fluorescence dynamics and the transport coefficients at the same time, the problem of disentangling the various effects is even more complicated, and may be intractable.

6.2 Better apparatus

Over the last three years, I have disassembled, redesigned, and reassembled the ABEL trap about 10 times. Nonetheless, there are still many potential improvements to the hardware. Here are a few:

1. Better fluid handling. Most people who make glass or fused silica microfluidic

cells permanently seal the top and bottom pieces to make a monolithic device. This has the advantage that the geometry is well defined and one does not have to worry about leaks. On the other hand, it is then difficult or impossible to clean the interior of the device, and devices can only be used a small number of times before they get gunked up. I chose to keep the top and bottom pieces separate so they could be cleaned independently. But then forming a sub-micron gap is difficult because a single dust particle can get lodged between the pieces of glass. Furthermore, the device is prone to messy leaks. It would be nice to have a way of rigidly but reversibly mounting the top and bottom pieces of fused silica together.

2. Ability to change solutions in real-time. It would also be nice to be able to hold an object in the ABEL trap, and then to change the solution conditions around it while keeping the object trapped (e.g. adding a ligand, drug, or enzyme). Such a stunt could be accomplished by flowing solution through all four deep channels in a symmetric way, so there is no fluid exchange in the trapping region, and then relying on diffusion to carry the new molecules the last 100 μm or so. A while ago I started to design a microfluidic system that would sit on top of the fused silica trapping cell and perform the fluid handling for this operation. Unfortunately this task hasn't been completed.

3. New optical capabilities. We are currently looking into a pulsed laser source so we can perform dynamic measurements of the fluorescence lifetime of trapped objects. It would also be nice to add a spectrometer to the output, or polarization-sensitive or multi-color APDs so we can obtain more detailed spectral information on trapped objects.

4. Faster software feedback. We recently bought an Andor iXon+ EMCCD camera, capable of frame rates as high as 2,500 Hz. This device could achieve much of the performance of the hardware-feedback system, but with the ease of use and convenience of software feedback. At such high video rates, the limiting factor becomes the ability of the computer to process the data in real time. Naveen Sinha is currently writing software to achieve this.

6.3 New molecules

The purpose of the ABEL trap is to enable new measurements on interesting and complex molecules. Now that the ABEL trap is working, we have a solution looking for a problem. Fortunately many biological and biochemical groups have expressed interest in giving us interesting fluorescently labeled molecules to trap and study.

We are particularly keen to use the ABEL trap to study transmembrane proteins at the single-molecule level. The idea is to put the protein in ~ 100 nm lipid vesicles labeled with many copies of an IR dye (Dyomics 780). We will use an IR laser and a CCD with software feedback to trap the vesicle, and then probe individual fluorophores on the protein with visible light. We bought a new Olympus microscope for this setup, and Kit Werley designed and assembled an optical system with two detection channels in the visible and one in the IR. The visible detection channels each go to an APD for FRET studies. Fig. 6.1 shows the layout of this new system.

We hope to use this setup in collaboration with Michael Börsch (Albert-Ludwigs-Universität Freiburg) to study the action of the F_0F_1 ATP synthase.[37] His group has produced enzymes with a FRET pair on the rotor and stator. The goal is to detect conformational substeps in the rotary motion. We also hope to use the same setup to trap lipid vesicles containing single β_2-adrenergic receptors (in collaboration with Brian Kobilka, Stanford).[96] The goal of this project is to see how different agonists and antagonists affect the dynamics of different parts of the receptor.

Both the Börsch group and the Kobilka groups have already attempted single-molecule studies on freely diffusing vesicles. These experiments yielded some valuable insights, but were hampered by the short observation times of each vesicle. In the case of the experiments on the β_2-adrenergic receptor, a distribution of underlying states was measured, but the dynamics of how one state became another. In the case of the experiments on the F_0F_1 ATP synthase, discrete substeps were observed, but no molecules were observed to undergo more than 3 or 4 steps—too little to acquire good statistics on the transitions of a single molecule.

Here are a few of the other leads we are pursuing:

1. Trapping single aggregates of the protein Huntingtin, which is the causative

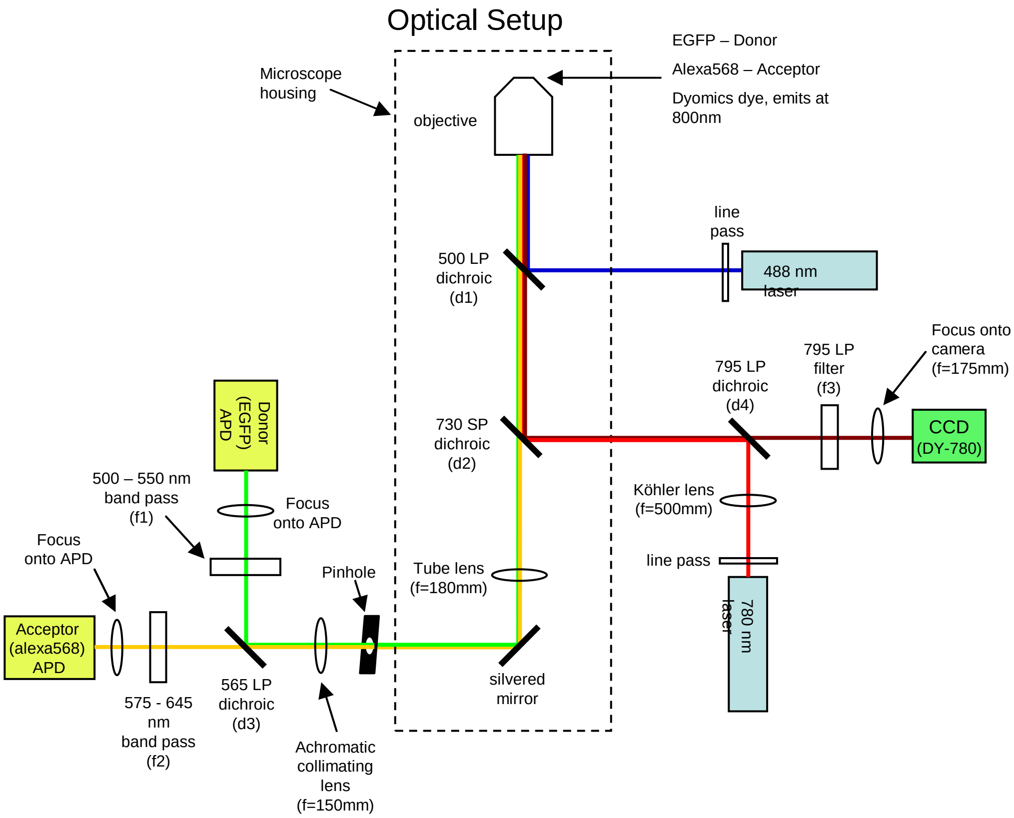

Figure 6.1: Optical setup for a three-color ABEL trap for performing FRET studies on transmembrane proteins held in IR-labeled vesicles. Image from Kit Werley.

agent in Huntington's disease. By dynamically measuring the diffusion coefficient and mobility of the aggregate, we hope to watch aggregation and growth of this important disease-causing molecule. This is a collaboration with Michael Tam in Judith Frydman's lab at Stanford.

2. Trapping of fluorescently labeled chaperonins. In collaboration with the lab of Judith Frydman (Stanford), we hope to learn all about the mechanism of the chaperonins GroEL and TriC. Our first goal is to trap many fluorescently labeled chaperonins to obtain accurate measures of diffusion coefficient and mobility. Then we hope to trap molecules bound with different numbers of fluorescently labeled ATPs, to learn how many ATPs are attached in different parts of the enzymatic cycle. Ultimately we want to trap a single substrate protein labeled with a FRET pair, and watch it fold inside the GroEL cavity.

3. Trapping of mKO.[66] Monomeric Kusabira-Orange (mKO) is one of the brightest and most photostable of the fluorescent proteins.[109] The wild-type version exists as a multimer in solution, but the Miyawaki lab (RIKEN, Japan) genetically modified it to exist as a 28.0 kDa monomer. Miyawaki has generously provided us with some mKO to try to trap.

4. Trapping single fluorophores. The attempts with Cy3 were only moderately successful. I think the problem is not with the strength of the trap, but rather with the blinking of the fluorophore—once the Cy3 goes into a dark state we lose it. I have found in bulk experiments that addition of 300 μM KI can significantly increase the brightness of a Cy3 solution, especially under intense irradiation. I believe that the KI is decreasing the lifetime of the dark triplet state. I hope soon to repeat this experiment inside the ABEL trap. I am also interested in trying to use Xe gas to purge the system of oxygen. Xenon is isoelectronic with the I^- anion, and has been reported to reduce triplet lifetimes in some species. Xenon has the further advantage of being completely inert. I would also like to trap other fluorophores, such as the Alexa dyes (strongly recommended by Amit Meller). Particularly interesting are the water-soluble terrylene diimide dyes provided by Klaus Mullen.[65] These dyes have exceptionally long lifetimes

and high brightness. The only problem is that in water, they only show these properties when solubilized with certain cationic surfactants.

6.4 Far-out ideas

In the longer run, there are many possible directions in which to take the ABEL trap. Here I list a few:

1. Fabrication. By trapping objects suspended in a photopolymerizable medium, one could move the object to a desired location, and then use a pulsed laser to immobilize the object there. This could be useful for making arrays of quantum dots for quantum optics applications.

2. Precise measurements on nanospheres to detect binding. One can hold a fluorescent polystyrene nanosphere in the ABEL trap for tens of minutes or even hours. During this time, one could measure its mobility and diffusion coefficient with very high accuracy. If the nanosphere binds molecules from the solution, one might be able to detect this in the transport properties of the nanosphere. For instance, one can measure the diffusion coefficient of a 20 nm sphere to within 1%. This corresponds to knowing its hydrodynamic radius to within 0.2 nm. Thus binding of a single protein to the nanosphere should be detectable.

3. Application of additional DC and AC electric fields. Intense AC electric fields can stretch and orient molecules. I did some preliminary experiments using these fields to stretch molecules of DNA in the ABEL trap, but more work needs to be done in this area. One could also apply quadrupolar fields (see Section 1.4.6) to stretch and orient molecules. Finally, circularly polarized AC fields may be able to rotate trapped objects, even if the object is not anisotropic.

4. Single-molecule isoelectric focusing. In the ABEL trap, I adjust the electric field around a molecule with fixed charge, to keep the molecule at a target position. One could also imagine adjusting the charge on a molecule in a fixed electric field. Since charge is a scalar, this can only be used to trap in one dimension.

In isoelectric focusing, one performs electrophoresis in a pH gradient, with the negative electrode on the high pH side and the positive electrode on the low pH side. If the molecule moves in either direction away from the point where the pH equals its isoelectric point, the molecule acquires a charge which experiences a force back toward the isoelectric point. I designed and partially built a microfluidic cell for performing isoelectric focusing to trap single fluorophores in narrow 1-D channels. Unlike the ABEL trap, the feedback mechanism here is intrinsic to the molecule. Thus the molecule does not need to be fluorescently labeled, and one could trap many molecules at once.

6.5 Comparison to other single-molecule techniques

A large number of beautiful single-molecule experiments have been conducted without the ABEL trap. Is the ABEL trap really necessary, and how does it compare to the other techniques? As explained in Section 1.2, single-molecule studies traditionally fall into one of two categories: surface-attached or free-solution. Surface-attachment procedures are difficult to perform and risk perturbing the molecule under study. Free-solution measurements are far easier, but are restricted to very brief observations of each molecule. I have discussed at length how the ABEL trap circumvents the problems of these other techniques. But the ABEL trap also retains some of their drawbacks, and creates some new drawbacks, which are worth discussing.

A molecule in the ABEL trap is certainly more perturbed than a molecule in free solution. Part of the perturbation comes from the walls of the trap, which confine the molecule to a thin film. In the case of large molecules, such as λ-DNA, the walls clearly distort the average shape of the molecule. Smaller molecules may also adhere to the walls of the trap, or undergo other specific chemical interactions with the walls. As the walls are squeezed closer together to reduce fluorescence background, the frequency of collisions with the walls increases. Coatings can ameliorate surface interactions to some extent, but not completely. The choice of surface coatings may be restricted by the requirement to maintain some electroosmotic flow for trapping.

The other perturbation comes from the electric fields. If all components of the solution are neutral and the feedback acts entirely through electroosmotic flow, then the feedback field does not affect the dynamics of molecules in the solution. However, real molecules have charges, ion clouds, and dipole moments. An external field creates stresses in systems with inhomogeneous charge distributions. Thus dipolar molecules experience a torque and stretching. Electric fields may be particularly significant if one is studying the interaction of two species in the solution (say one labeled and the other dark) that have different electrokinetic mobilities. Then the field leads to relative motion, which increases the rate of collisional encounters. But if the field is strong enough it may prevent molecules from sticking when they do collide. By distorting the ion clouds around trapped molecules, the electric field also modifies the short-range ionic forces. I have often observed that very large electric fields increase the probability of particles sticking to the walls of the trap. I do not have an explanation for this effect, but suspect it has to do with the electric field distorting the ion distribution around the particle, the walls, or both. Thus the ABEL trap is not immune to the criticism that the experiment is perturbing the dynamics. In general, any data from the ABEL trap will have to be supplemented by other single-molecule and bulk controls.

The other potential drawback of the ABEL trap is the difficulty of studying a vast number of molecules in one sitting. In experiments that use surface-attachment, wide field imaging often allows one to study dozens or hundreds of molecules simultaneously. In a few minutes of data collection one can image enough molecules to make beautiful histograms and correlation functions. In FCS experiments one typically studies only one molecule at a time, but the experiments often last for hours, again leading to data from thousands of molecules. The ABEL trap is currently not stable enough to run for more than a few tens of minutes without changing the solution. Some of the problems may be solved by better engineering: fluid leakage and mechanical stability can be improved. Undesirable electrochemical byproducts from the trapping electrodes diffuse into the trapping region on the 10-minute timescale too. This may be solved by putting the electrodes further away. A more fundamental problem is that because each molecule is studied for a longer time, solutions in the ABEL trap must be more dilute than in FCS experiments to avoid having multiple molecules in the trapping region. If it takes a long time for a second molecule to diffuse into the trapping region when one molecule is trapped, then it also takes a long time for a first molecule to diffuse in when the trap is empty. This means that one often spends long periods of time staring at a blank oscilloscope, waiting for a molecule to float by.

A further disadvantage of the ABEL trap compared to surface-attachment is that a single surface-attached molecule may be studied for an almost arbitrarily long time, while this is not the case in the ABEL trap. The total number of photons from a surface-attached molecule is finite, but the molecule can evolve in the dark in between widely spaced periods of observation. Alternatively, one may use a low excitation intensity if one is content with a low photon count-rate. The ABEL trap requires a high photon count-rate to keep an object trapped. This places a severe restriction on the observation time of molecules that are prone to photobleaching.

A good experiment will not rely on the ABEL trap as the sole experimental technique, but will corroborate the data with other single-molecule and bulk studies. My hope is for the ABEL trap to cease being a special technique, and to become one of the many items in the arsenal of single-molecule researchers.

Bibliography

[1] M. Andrec, R. M. Levy, and D. S. Talaga, *Direct determination of kinetic rates from single molecule photon arrival trajectories using hidden markov models*, J. Phys. Chem. A **107** (2003), 7454–7464.

[2] S. Arnold and N. Hessel, *Photoemission from single electrodynamically levitated microparticles*, Rev. Sci. Inst. **56** (1985), 2066–2069.

[3] A. Ashkin, *Optical trapping and manipulation of neutral particles using lasers*, Proc. Natl. Acad. Sci. USA **94** (1997), 4853–4860.

[4] A. Ashkin and J. M. Dziedzic, *Optical trapping and manipulation of viruses and bacteria*, Science **235** (1987), 1517–1520.

[5] A. Ashkin, J. M. Dziedzic, J. E. Bjorkholm, and S. Chu, *Observation of a single-beam gradient force optical trap for dielectric particles*, Opt. Lett. **11** (1986), 288–290.

[6] A. Bacciotti, *Liapunov functions and stability in control theory*, Springer, Berlin, 2005.

[7] M. A. Balsera, W. Wriggers, Y. Oono, and K. Schulten, *Principal component analysis and long time protein dynamics*, J. Phys. Chem. **100** (1996), 2567–2572.

[8] A. J. Bard and L. R. Faulkner, *Electrochemical methods*, John Wiley & Sons, New York, 1980.

[9] Christoph G. Baumann, Steven B. Smith, Victor A. Bloomfield, and Carlos Bustamante, *Ionic effects on the elasticity of single DNA molecules*, Proc. Natl. Acad. Sci. USA **94** (1997), no. 12, 6185–6190.

[10] J. Bechhoefer, *Feedback for physicists: A tutorial essay on control*, Rev. Mod. Phys. **77** (2005), 783–836.

[11] D. Belder, A. Deege, F. Kohler, and M. Ludwig, *Poly(vinyl alcohol)-coated microfluidic devices for high-performance microchip electrophoresis*, Electrohporesis **23** (2002), 3567–3573.

[12] D. Belder and M. Ludwig, *Surface modification in microchip electrophoresis*, Electrophoresis **24** (2003), 3595–3606.

[13] H. Berg, *How to track bacteria*, Rev. Sci. Inst. **42** (1971), 868–871.

[14] A. J. Berglund and H. Mabuchi, *Feedback controller design for tracking a single fluorescent molecule*, Appl. Phys. B **78** (2004), 653–659.

[15] ———, *Tracking-FCS: Fluorescence correlation spectroscopy of individual particles*, Opt. Express **13** (2005), 8069–8082.

[16] B. J. Berne and R. Pecora, *Dynamic light scattering: With applications to chemistry, biology, and physics*, Dover, 2000.

[17] G. Binnig, C. F. Quate, and Ch. Gerber, *Atomic force microscope*, Phys. Rev. Lett. **56** (1986), 930–933.

[18] G. Binnig, H. Rohrer, Ch. Gerber, and E. Weibel, *7×7 Reconstruction on Si(111) Resolved in Real Space*, Phys. Rev. Lett. **50** (1983), 120–123.

[19] F. Booth, *Surface conductance and cataphoresis*, Trans. Faraday Soc. **44** (1948), 955–959.

[20] E. Boukobza, A. Sonnenfeld, and G. Haran, *Immobilization in surface-tethered lipid vesicles as a new tool for single biomolecule spectroscopy*, J. Phys. Chem. B **105** (2001), 12165–12170.

[21] P. J. Brockwell and R. A. Davis, *Introduction to time series and forecasting*, 2nd ed., Springer, New York, 2002.

[22] B. Brooks and M. Karplus, *Harmonic dynamics of proteins: Normal modes and fluctuations in bovine pancreatic trypsin inhibitor*, Proc. Natl. Acad. Sci. USA **80** (1983), 6571–6575.

[23] R. Brown, *On the existence of active molecules in inorganic bodies*, Phil. Mag. New Ser. **4** (1828), 161–173.

[24] D. Brune and S. Kim, *Predicting protein diffusion coefficients*, Proc. Natl. Acad. Sci. USA **90** (1993), 3835–3839.

[25] Z. Bubnicki, *Modern control theory*, Springer, Berlin, 2006.

[26] C. Bustamante, Z. Bryant, and S. B. Smith, *Ten years of tension: single-molecule DNA mechanics*, Nature **421** (2003), 423–427.

[27] H. Cang, C. M. Wong, C. S. Xu, A. H. Rizvi, and H. Yang, *Confocal three dimensional tracking of a single nanoparticle with concurrent spectroscopic readouts*, Appl. Phys. Lett. **88** (2006), 223901.

[28] J. Cao, *Single molecule tracking of heterogeneous diffusion*, Phys. Rev. E **63** (2001), 041101.

[29] S. Chandrasekhar, *Stochastic problems in physics and astronomy*, Rev. Mod. Phys. **15** (1943), 1–89.

[30] S. Chaudhary and B. Shapiro, *Arbitrary steering of multiple particles independently in an electro-osmotically driven microfluidic system*, IEEE Transactions on Control Systems Technology (2005), 669–680.

[31] Y.-L. Chen, M. D. Graham, J. J. de Pablo, G. C. Randall, M. Gupta, and P. S. Doyle, *Conformation and dynamics of single DNA molecules in parallel-plate slit microchannels*, Phys. Rev. E **70** (2004), no. 6, 060901.

[32] D. T. Chiu and R. N. Zare, *Biased diffusion, optical trapping, and manipulation of single molecules in solution*, J. Am. Chem. Soc. **118**, 6512–6513.

[33] A. E. Cohen and W. E. Moerner, *Method for trapping and manipulating nanoscale objects in solution*, Appl. Phys. Lett. **86** (2005), 093109.

[34] M. B. Comisarow and A. G. Marshall, *Frequency-sweep fourier transform ion cyclotron resonance spectroscopy*, Chem. Phys. Lett. **26** (1974), 489–490.

[35] P.G. de Gennes, *Quasi-elastic scattering of neutrons by dilute polymer solutions. 1. free-draining limit*, Physics **3** (1967), 37–45.

[36] H. Dehmelt, *Experiments with an isolated subatomic particle at rest*, Rev. Mod. Phys. **62** (1990), 525–530.

[37] M. Diez, B. Zimmermann, M. Börsch, M. König, E. Schweinberge, S. Steigmiller, R. Reuter, S. Felekyan, V. Kudryavtsev, C. A. M. Seidel, and P. Gräber, *Proton-powered subunit rotation in single F_0F_1-ATP synthase.*

[38] M Doi and S. F. Edwards, *The theory of polymer dynamics*, Oxford University Press, Oxford, 1988.

[39] E. Dubois-Violette and P.G. de Gennes, *Quasi-elastic scattering by dilute, ideal, polymer solutions. ii. effects of hydrodynamic interaction*, Physics **3** (1967), 181–198.

[40] D. M. Eigler and E. K. Schweizer, *Positioning single atoms with a scanning tunnelling microscope*, Nature (1990), 524–526.

[41] A. Einstein, *On the motion of small particles suspended in liquids at rest required by the molecular-kinetic theory of heat*, Annalen der Physik **17** (1905), 549–560.

[42] J. Enderlein, *Tracking of fluorescent molecules diffusing within membranes*, Appl. Phys. B **71** (2000), 773–777.

[43] A. Evilevitch, L. Lavelle, C. M. Knobler, E. Raspaud, and W. M. Gelbart, *Osmotic pressure inhibition of DNA ejection from phage*, Proc. Natl. Acad. Sci. USA **100** (2003), 9292–9295.

[44] H. Fujita, *Some unsolved problems on dilute polymer solutions*, Macromolecules **21** (1988), 179–185.

[45] J. Gaudioso and H. Craighead, *Characterizing electroosmotic flow in microfluidic devices*, J. Chromatography A **971** (2002), 249–253.

[46] C. Gell, D. J. Brockwell, G. S. Beddard, S. E. Radford, A. P. Kalverda, and D. A. Smith, *Accurate use of single molecule fluorescence correlation spectroscopy to determine molecular diffusion times*, Single Molecules **2** (2001), 177–181.

[47] S. Ghaemmaghami, W. Huh, K. Bower, R. W. Howson, A. Belle, N. Dephoure, E. K. O'Shea, and J. S. Weissman, *Global analysis of protein expression in yeast*, Nature **425** (2003), 737–741.

[48] C. Gosse and V. Croquette, *Magnetic tweezers: micromanipulation and force measurement at the molecular level*, Biophys. J. **82** (2002), 3314–3329.

[49] M. Goulian and S. M. Simon, *Tracking single proteins within cells*, Biophys J **79** (2000), 2188–2198.

[50] D. G. Grier, *A revolution in optical trapping*, Nature **424** (2003), 810–816.

[51] A. Yu. Grosberg, T. T. Nguyen, and B. I. Shklovskii, *Colloquium: The physics of charge inversion in chemical and biological systems*, Rev. Mod. Phys. **74** (2002), 329–345.

[52] P. D. Grossman and D. S. Soane, *Orientation effects on the electrophoretic mobility of rod-shaped molecules in free solution*, Anal. Chem. **62** (1990), 1592–1596.

[53] J. T. Groves, C. Wulfing, and S. G. Boxer, *Electrical manipulation of glycan-phosphatidyl inositol-tethered proteins in planar supported bilayers*, Biophys. J. **71** (1996), 2716–2723.

[54] C. Haber, S. A. Ruiz, and D. Wirtz, *Shape anisotropy of a single random-walk polymer*, Proc. Natl. Acad. Sci. USA **97** (2000), 10792–10795.

[55] S. Hayward and N. Go, *Collective variable description of native protein dynamics*, Annu. Rev. Phys. Chem. **46** (1995), 223–250.

[56] D. C. Henry, *The cataphoresis of suspended particles. Part I. The equation of cataphoresis*, Proc. Roy. Soc. Lond. Ser. A **133** (1931), 106–109.

[57] ______, *The electrophoresis of suspended particles. iv. the surface conductivity effect*, Trans. Faraday Soc. **44** (1948), 1021–1026.

[58] S. T. Hess, S. Huang, A. A. Heikal, and W. W. Webb, *Biological and chemical applications of fluorescence correlation spectroscopy: a review*, Biochemistry **41** (2002), no. 3, 697–705.

[59] Julia S. Higgins and Henry C. Benoit, *Polymers and neutron scattering*, Oxford University Press, Oxford, 1994.

[60] R. E. Holmlin, M. Schiavoni, C. Y. Chen, S. P. Smith, M. G. Prentiss, and G. M. Whitesides, *Light-driven microfabrication: Assembly of multicomponent, three-dimensional structures by using optical tweezers*, Angewandte Chemie **39** (2000), 3503–3506.

[61] S. Hu, X. Ren, M. Bachman, C. E. Sims, G. P. Li, and N. L. Allbritton, *Tailoring the surface properties of poly(dimethylsiloxane) microfluidic devices*, Langmuir **20** (2004), 5569–5574.

[62] M. A. Ivanova, A. V. Arutyunyan, A. V. Lomakin, and V. A. Noskin, *Study of DNA internal dynamics by quasi-elastic light scattering*, Appl. Optics **36** (1997), 7657.

[63] J. E. Jackson, *A user's guide to principal components*, John Wiley & Sons, Hoboken, NJ, 2003.

[64] Y. J. Juan, S. Wang, X. Hu, and L. J. Lee, *Dynamics of single polymers in a stagnation flow induced by electrokinetics*, Phys. Rev. Lett. **93** (2004), 268105.

[65] C. Jung, B. K. Muller, D. C. Lamb, F. Nolde, K. Mullen, and C. Brauchle, *A new photostable terrylene diimide dye for applications in single molecule studies and membrane labeling.*

[66] S. Karasawa, T. Araki, T. Nagai, H. Mizuno, and A. Miyawaki, *Cyan-emitting and orange-emitting fluorescent proteins as a donor/acceptor pair for fluorescence resonance energy transfer*, Biochem. J. **381** (2004), 307–312.

[67] M. Karplus and J. N. Kushick, *Method for estimating the configurational entropy of macromolecules*, Macromol. **14** (1981), 325–332.

[68] S. Katsura, A. Yamaguchi, H. Inami, S. Matsuura, K. Hirano, and A. Mizuno, *Indirect micromanipulation of single molecules in water-in-oil emulsion*, Electrophoresis **22** (2001), 289–293.

[69] M. G. Khaledi (ed.), *High-performance capillary electrophoresis: Theory, techniques, and applications*, John Wiley & Sons, New York, 1998.

[70] K. Kis-Petikova and E. Gratton, *Distance measurement by circular scanning of the excitation beam in the two-photon microscope*, Microscopy Research and Technique **63** (2004), 34–49.

[71] S. C. Kou, X. S. Xie, and J. S. Liu, *Bayesian analysis of single-molecule experimental data*, Appl. Statist. **54** (2005), 469–506.

[72] K. Kroy and E. Frey, *Dynamic scattering from solutions of semiflexible polymers*, Phys. Rev. E **55** (1997), 3092.

[73] V. Levi, Q. Ruan, and E. Gratton, *3-d particle tracking in a two-photon microscope: Application to the study of molecular dynamics in cells*, Biophys. J. **88** (2005), 2919–2928.

[74] E. A. Lipman, B. Schuler, O. Bakajin, and W. Eaton, *Single-molecule measurement of protein folding kinetics*, Science **301** (2003), 1233–1235.

[75] X. Liu, D. Erickson, D. Li, and U. J. Krull, *Cationic polymer coatings for design of electroosmotic flow and control of DNA adsorption*, Anal. Chem. Acta **508** (2004), 55–62.

[76] Y. Liu, Fanguy J. C., J. M. Bledsoe, and C. S. Henry, *Dynamic coating using polelectrolyte multilayers for chemical control of electroosmotic flow in capillary electrophoresis microchips*, Anal. Chem. **72** (2000), 5939–5944.

[77] D. Long, J. L. Viovy, and A. Ajdari, *Simultaneous action of electric fields and nonelectric forces on a polyelectrolyte: motion and deformation*, Phys. Rev. Lett. **76** (1996), 3858–3861.

[78] D. Lumma, S. Keller, T. Vilgis, and J. O. Radler, *Dynamics of large semiflexible chains probed by fluorescence correlation spectroscopy*, Phys. Rev. Lett. **90** (2003), no. 21, 218301.

[79] B. Maier and J. O. Rädler, *Conformation and self-diffusion of single DNA molecules confined to two dimensions*, Phys. Rev. Lett. **82** (1999), 1911–1914.

[80] H. Makamba, J. H. Kim, K. Lim, N. Park, , and J. H. Hahn, *Surface modification of poly(dimethylsiloxane) microchannels*, Electrophoresis **24** (2003), 3607–3619.

[81] L. I. McCann, M. Dykman, and B. Golding, *Thermally activated transitions in a bistable three-dimensional optical trap*, Nature **402** (1999), 785–787.

[82] U. Meseth, T. Wohland, R. Rigler, and H. Vogel, *Resolution of fluorescence correlation measurements*, Biophys. J. **76** (1999), 1619–1631.

[83] R. Mills, *Self-diffusion in normal and heavy water in the range 1-45°*, J. Phys. Chem. **77** (1973), 685–688.

[84] M. Minor, A. J. van der Linde, H. P. van Leeuwen, and J. Lyklema, *Dynamic aspects of electrophoresis and electroosmosis: A new fast method ofr measuring particle mobilities*, J. Colloid Interface Sci. **189** (1997), 370–375.

[85] Orrit M. Moerner, W. E., *Illuminating single molecules in condensed matter*, Science **283** (1999), 1670–1676.

[86] W. E. Moerner, *A dozen years of single-molecule spectroscopy in physics, chemistry, and biophysics*, J. Phys. Chem. B **106** (2002), 910–927.

[87] W. E. Moerner and D. P. Fromm, *Methods of single-molecule fluorescence spectroscopy and microscopy*, Review of Scientific Instruments **74** (2003), 3597–3619.

[88] D. Montiel, H. Cang, and H. Yang, *Quantitative characterization of changes in dynamical behavior for single-particle tracking studies*, J. Phys. Chem. B (2006).

[89] K. C. Neuman, E. A. Abbondanzieri, R. Landick, J. Gelles, and S. M. Block, *Ubiquitous transcrptional pausing is independent of RNA polymerase backtracking*, Cell **115** (2003), no. 437-447, 437.

[90] K. C. Neuman and S. M. Block, *Optical trapping*, Rev. Sci. Instrum. **75** (2004), 2787–2809.

[91] R. W. O'Brien and L. R. White, *Electrophoretic mobility of a spherical colloidal particle*, J. Chem. Soc., Faraday Trans. 2 **74** (1978), 1607–1626.

[92] M. A. Osborne, S. Balasubramanian, W. S. Furey, and D. Klenerman, *Optically biased diffusion of single molecules studied by confocal fluorescence microscopy*, J. Phys. Chem. B **102** (1998), 3160–3167.

[93] R. Parthasarathy and J. T. Groves, *Protein patterns at lipid bilayer junctions*, Proc. Natl. Acad. Sci. USA **101** (2003), 12798–12803.

[94] W. Paul, *Electromagnetic traps for charged and neutral particles*, Rev. Mod. Phys. **62** (1990), 531–540.

[95] R. Pecora, *DNA: a model compound for solution studies of macromolecules*, Science **251** (1991), no. 4996, 893.

[96] G. Peleg, P. Ghanouni, B. K. Kobilka, and R. N. Zare, *Single-molecule spectroscopy of the β_2 adrenergic receptor: Observation of conformational substates in a membrane protein*, Proc. Natl. Acad. Sci. USA **98** (2001), 8469–8474.

[97] E. J. G. Peterman, S. Brasselet, and W. E. Moerner, *The fluorescence dynamics of single molecules of green fluorescent protein*, J. Phys. Chem. A **103** (1999), 10553–10560.

[98] M. L. Plenert and J. B. Shear, *Microsecond electrophoresis*, Proc. Natl. Acad. Sci. USA **100** (2003), 38533857.

[99] H. Qian, M. P. Sheetz, and E. L. Elson, *Single particle tracking. analysis of diffusion and flow in two- dimensional systems*, Biophys. J. **60** (1991), 910–921.

[100] S. R. Quake, H. P. Babcock, and S. Chu, *The dynamics of partially extended single molecules of DNA*, Nature **388** (1997), 151–154.

[101] Y. Rondelez, G. Tresset, K. V. Tabata, H. Arata, H. Fujita, S. Takeuchi, and H. Noji, *Highly coupled ATP synthesis by F_1-ATPase single molecules*, Nature Biotech. **23** (2005), 361–365.

[102] P. E. Rouse, *A theory of the linear viscoelastic properties of dilute solutions of coiling polymers*, J. Chem. Phys. **21** (1953), 1272–1280.

[103] J. Rudnick and G. Gaspari, *The shapes of random walks*, Science **237** (1987), 384–389.

[104] R. Salmon, *Hamiltonian fluid mechanics*, Ann. Rev. Fluid Mech. **20** (1988), 225–256.

[105] T. Savin and P. S. Doyle, *Static and dynamic errors in particle tracking microrheology*, Biophys. J. **88** (2005), 623–638.

[106] Th. Schmidt, G. J. Schütz, W. Baumgartner, H. J. Gruber, and H. Schindler, *Imaging of single molecule diffusion*, Proc. Natl. Acad. Sci. USA **93** (1996), 2926–2929.

[107] M. Schulz, *Control theory in physics and other fields of science: concepts, tools, and applications*, Springer, Berlin, 2006.

[108] C. Schwer and E. Kenndler, *Electrophoresis in fused-silica capillaries: The influence of organic solvents on the electroosmotic velocity and the ζ potential*, Anal. Chem. **63** (1991), 1801–1807.

[109] N. C. Shaner, P. A. Steinbach, and R. Y. Tsien, *A guide to choosing fluorescent proteins*, Nat. Methods **2** (2005), 905–909.

[110] E. S.G. Shaqfeh, *The dynamics of single-molecule DNA in flow*, Journal of Non-Newtonian Fluid Mechanics **130** (2005), 1–28.

[111] R. Shusterman, S. Alon, T. Gavrinyov, and O. Krichevsky, *Monomer dynamics in double- and single-stranded DNA polymers*, Phys. Rev. Lett. **92** (2004), 048303.

[112] D. E. Smith, T. T. Perkins, and S Chu, *Dynamical scaling of DNA diffusion coefficients*, Macromolecules **29** (1996), 1372.

[113] D. E. Smith, J. T. Sander, S. B. Smith, S. Grimes, D. L. Anderson, and C. Bustamante, *The bacteriophage phi29 portal motor can package DNA against a large internal force*, Nature **413** (2001), 748–752.

[114] S. S. Sommer and J. E. Cohen, *The size distributions of proteins, mRNA, and nuclear RNA*, J. Molec. Evol. **15** (1980), 37–57.

[115] T. R. Strick, M-N. Dessinges, G. Charvin, N. H. Dekker, J-F. Allemand, D. Bensimon, and V. Croquette, *Stretching of macromolecules and proteins*, Rep. Prog. Phys. **66** (2003), 1–45.

[116] A. Sze, D. Erickson, L. Ren, and D. Li, *Zeta-potential measurement using the smoluchowski equation and the slope of the current-time relationship in electroosmotic flow*, J. Colloid Interface Sci. **261** (2003), 402–410.

[117] D. S. Talaga, *Information theoretical approach to single-molecule experimental design and interpretation*, J. Phys. Chem. A **110** (2006), 9743–9757.

[118] Svetlana A. Tatarkova and David A. Berk, *Probing single DNA mobility with fluorescence correlation microscopy*, Phys. Rev. E **71** (2005), no. 4, 041913.

[119] R. E. Thompson, D. R. Larson, and W. W. Webb, *Precise nanometer localization analysis for individual fluorescent probes*, Biophys. J. **82** (2002), 2775–2783.

[120] T. Tsuda, *Modification of electroosmotic flow with cetyltrimethylammonium bromide in capillary zone electrophoresis*, J. High Res. Chromatography & Chromatography Communications **10** (1987), 622–624.

[121] M. T. Tyn and T. W. Gusek, *Prediction of diffusion coefficients of proteins*, Biotechnol. Bioeng. **35** (1990), 327–338.

[122] R. S. Van Dyck, P. B. Schwinberg, and H. G. Dehmelt, *New high-precision comparison of electron and positron g factors*, Phys. Rev. Lett. **59** (1987), 26–29.

[123] N. G. Van Kampen, *Stochastic processes in physics and chemistry*, North-Holland, 1992.

[124] J. Voldman, R. A. Braff, M. Toner, M. L. Gray, and M. A. Schmidt, *Holding forces of single-particle dielectrophoretic traps*, Biophys. J. **80** (2001), 531–541.

[125] M. Vrljic, S. Y. Nishimura, S. Brasselet, W. E. Moerner, and H. M. McConnell, *Translational diffusion of individual class II MHC membrane proteins in cells*, Biophys J **83** (2002), 2681–2692.

[126] K. Šolc and W. H. Stockmayer, *Shape of a random-flight chain*, J. Chem. Phys. **54** (1977), 2756–2757.

[127] M. D. Wang, H. Yin, R. Landick, J. Gelles, and S. M. Block, *Stretching DNA with optical tweezers*, Biophys. J. **72** (1997), no. 3, 1335–1346.

[128] S. Q. Wang and K. F. Freed, *Renormalization group study of rouse–zimm model of polymer dynamics through second order in epsilon*, J. Chem. Phys. **85** (1986), no. 10, 6210–6224.

[129] ———, *Renormalization group theory of the rouse–zimm model of polymer dynamics to second order in epsilon. ii. dynamic intrinsic viscosity of gaussian chains*, J. Chem. Phys. **86** (1987), no. 5, 3021–3031.

[130] L. P. Watkins and H. Yang, *Information bounds and optimal analysis of dynamic single molecule measurements*, Biophys. J. **86** (2004), 4015–4029.

[131] P. H. Wiersema, Loeb A. L., and J. Th. G. Overbeek, *Calculation of the electrophoretic mobility of a spherical colloid particle*, J. Colloid Interface Sci. **22** (1966), 78–99.

[132] J. Wilcoxon and J. M. Schurr, *Dynamic light scattering from thin rigid rods: Anisotropy of translational diffusion of tobacco mosaic virus*, Biopolymers **22** (1983), 849–867.

[133] H. Yang, G. Luo, P. Karnchanaphanurach, T. Louie, I. Rech, S. Cova, L. Xun, and X. S. Xie, *Protein conformational dynamics probed by single-molecule electron transfer*, Science **302** (2003), 262–266.

[134] H. Yang and X. S. Xie, *Probing single molecule dynamics photon by photon*, J. Chem. Phys. **117** (2002), 10965–10979.

[135] I. C. Yeh and G. Hummer, *Diffusion and electrophoretic mobility of single-stranded RNA from molecular dynamics simulations*, Biophys. J. **86** (2004), 681–689.

[136] C. Yoshina-Ishii, Y.-H. M. Chan, J. M. Johnson, L. A. Kung, P. Lenz, and S. G. Boxer.

[137] C. Yoshina-Ishii, G. P. Miller, M. L. Kraft, E. T. Kool, and S. G. Boxer, *General method for modification of liposomes for encoded assembly on supported bilayers*, J. Am. Chem. Soc. **127** (2005), 1356–1357.

[138] N. Zarrabi, B. Zimmermann, M. Diez, P. Graeber, J. Wrachtrup, and M. Boersch, *Asymmetry of rotational catalysis of single membrane-bound* F_0F_1*-ATP synthase*, Proc. SPIE **5699** (2005), 175–188.

[139] B. H. Zimm, *Dynamics of polymer molecules in dilute solution: viscoelasticity, flow birefringence and dielectric loss*, J. Chem. Phys. **24** (1956), 269–278.